

COMPARISON AND VALIDATION OF ARCTIC PRECIPITATION FIELDS FROM
THREE ATMOSPHERIC REANALYSES: CFSR, MERRA, ERA-INTERIM

by

ALLISON R. HURLEY

B.S., The Pennsylvania State University, 2009

A thesis submitted to the
Faculty of the Graduate School of the
University of Colorado in partial fulfillment
of the requirement for the degree of

Master of Arts

Department of Geography

2014

This thesis entitled:
Comparison and validation of Arctic precipitation fields from three atmospheric reanalyses:
CFSR, MERRA, ERA-Interim
written by Allison R. Hurley
has been approved for the Department of Geography

Mark C. Serreze

Peter D. Blanken

John J. Cassano

Date _____

The final copy of this thesis has been examined by the signatories, and we find that both the content and the form meet acceptable presentation standards of scholarly work in the above mentioned discipline.

Hurley, Allison R. (M.A., Geography)

Comparison and validation of Arctic precipitation fields from three atmospheric reanalyses: CFSR, MERRA, ERA-Interim

Thesis directed by Professor Mark C. Serreze

Abstract

The intent of this thesis project was to investigate Arctic precipitation from three atmospheric reanalyses: Modern Era Retrospective Analysis for Research and Applications (MERRA), Climate Forecast System Reanalysis (CFSR), European Centre for Medium-Range Weather Forecasts Reanalysis-Interim (ERA-Interim). The first objective of the study was to determine if the three atmospheric reanalyses provide an accurate depiction of seasonal precipitation patterns. Spatial variability, recent trends, and anomalies in Arctic precipitation were investigated. The second objective was to conduct a statistical validation of each of the reanalysis products through a comparison with monthly GHCN station observations. Monthly precipitation fields were investigated for the period spanning January 1979 – December 2010. Overall, MERRA, CFSR, and ERA-Interim captured the known average monthly precipitation patterns across the Arctic. One notable discrepancy with ERA-Interim’s precipitation field exists across the northern North Atlantic and is further investigated using nearby coastal station data. Station observations were then used to validate the reanalyses across the entire Arctic. Bias, correlations, root mean-squared error were calculated. The largest inconsistency between the reanalyses and the station observations exists in summer; smaller biases and errors exist in winter. However, associated model errors and biases are found to be related to the number of observations utilized. The ability to pinpoint the best reanalysis for use in Arctic hydrologic studies lies in further investigation of the precipitation assimilation process in each reanalysis as well as an improvement in the accuracy of gauge measurements.

ACKNOWLEDGEMENTS

This thesis was made possible by the personal and financial support of many people and organizations. First and foremost, I would like to extend immense gratitude to my graduate adviser and mentor, Mark Serreze. Mark was the director of this thesis project and also provided the means for me to attend graduate school via NSF grants. Thank you, Mark, for your unrelenting patience and support, helpful advice, and quirky jokes. I'd also like to extend thanks to my committee members, Peter Blanken and John Cassano, for their helpful critiques of this thesis. A special thank you also goes out to Andrew Barrett for the countless coding tips he imparted on me as I learned NCL.

I could not have survived my graduate school journey without the support of my family, friends, and fellow classmates. Mahsa Moussavi, I am forever grateful for your friendship and the fact that you share my affinity for corny radiative transfer jokes. Thank you, Leah Meromy, for your optimism. I am also thankful for my office mates, Glenn Grant, Alex Crawford, and Karen Alley, for their companionship and moral support. Thank you to my parents, Diane and John Hurley, for their continual love and support. And last, but not least, I would like to thank my husband-to-be, Sean Prendergast, for talking me off the ledge when I was overwhelmed by stress and for always reminding me to smile.

CONTENTS

CHAPTER 1	INTRODUCTION	1
	1.1 Background.....	1
	1.2 Objectives and Scope.....	9
	1.3 Thesis Organization.....	13
CHAPTER 2	ATMOSPHERIC REANALYSES	14
	2.1 Reanalysis Systems.....	14
	2.1.1 MERRA	21
	2.1.2 CFSR.....	23
	2.1.3 ERA-Interim.....	25
CHAPTER 3	ARCTIC PRECIPITATION	27
	3.1 Seasonality of Precipitation.....	27
	3.1.1 Winter.....	29
	3.1.2 Spring.....	31
	3.1.3 Summer.....	31
	3.1.4 Autumn.....	32
	3.2 Recent Precipitation Changes.....	33
	3.2.1 Methods.....	33
	3.2.2 Results.....	42

	3.3 The ERA-Interim Discrepancy	44
	3.3.1 <i>General Circulation Analysis</i>	44
	3.3.2 <i>Coastal Station Analysis</i>	49
CHAPTER 4	VALIDATION	58
	4.1 Comparison with Observations	58
	4.1.1 <i>Methods</i>	59
	4.1.2 <i>Results</i>	63
CHAPTER 5	SYNTHESIS	75
	5.1 Discussion	75
	5.1.1 <i>Addressing Objective I</i>	75
	5.1.2 <i>Addressing Objective II</i>	78
	5.1.3 <i>Study Limitations</i>	78
	5.2 Conclusions	81
	5.3 Future Work	82
	REFERENCES	84
APPENDIX A.	GHCN STATIONS AND THEIR LOCATIONS	92

LIST OF TABLES

Table

1	Information regarding the web sources and data for each reanalysis.....	19
2	Data used to inform the model within each reanalysis.....	20
3	Location and time span details for the North Atlantic coastal stations.....	50
4	Mann-Kendall trend test results for coastal stations.....	53
5	Number of stations with statistically significant correlations.....	62
6	Mean, median, maximum, and minimum correlation coefficients.....	67
7	Mean, median, maximum, and minimum RMSE values.....	68
8	Number of stations with positive and negative biases for each season.....	71

LIST OF FIGURES

Figure

1 a, b	Map and graph of linear trends in surface temperature.....	2
2	Schematic of the sea ice-albedo feedback mechanism.....	4
3	Map of the Arctic with major drainage basins labeled	7
4	Bar plot highlighting the large variability of snow gauges.....	11
5	Schematic of reanalysis assimilation processes.....	17
6	Schematic of one full analysis cycle in a reanalysis.....	17
7	Maps of monthly mean precipitation for the four mid-season months.....	28
8	Maps of sea-level pressure fields for January and July.....	30
9	Plots of long term monthly trends for MERRA.....	35
10	Plots of long term monthly trends for CFSR.....	36
11	Plots of long term monthly trends for ERA-Interim.....	37
12	Anomaly plots for winter (DJF).....	38
13	Anomaly plots for spring (MAM).....	39
14	Anomaly plots for summer (JJA).....	40
15	Anomaly plots for autumn (SON).....	41
16	Sea level pressure winter anomalies.....	46
17	500 mb geopotential height winter anomalies.....	47

18	Precipitable water winter anomalies.....	48
19	Location map of North Atlantic coastal stations.....	51
20	Map of GHCN station locations.....	59
21	Map of winter (DJF) correlations and RMSE.....	63
22	Map of spring (MAM) correlations and RMSE.....	64
23	Map of summer (JJA) correlations and RMSE.....	65
24	Map of autumn (SON) correlations and RMSE.....	66
25	Boxplots for precipitation RMSE and correlations.....	69
26	Bar plot of average RMSE for each season.....	70
27	Bar plot of average model biases for each season.....	71
28	RMSE vs. observations plots.....	73
29	RMSE vs. observations plots, with outliers removed.....	74

CHAPTER 1

INTRODUCTION

1.1 Background

Mean global air temperatures have increased $\sim 0.6^{\circ}\text{C}$ (1.1°F) since the mid-20th Century (Hansen, et al., 2006). However, this observed warming trend is not expressed equally across all regions of the globe. Data from the National Aeronautics and Space Administration Goddard Institute for Space Sciences (NASA GISS) was used to create **Figure 1a**, a map of annual global temperature trends. The reds/oranges indicate that a location experienced warming during this 32 year period; blues indicate cooling. Warming dominates most of the globe for the period 1979 onwards, but the strongest warming has occurred over the Arctic. This enhanced Arctic warming is even more evident from looking at **Figure 1b**, which is a graphical representation of the zonal mean temperature trends. Indeed, over the past three decades, the Arctic region has warmed nearly twice as fast as any other location on the planet. Both the map and graph highlight the 32-year period between 1979 and 2010, the time period of emphasis throughout this thesis.

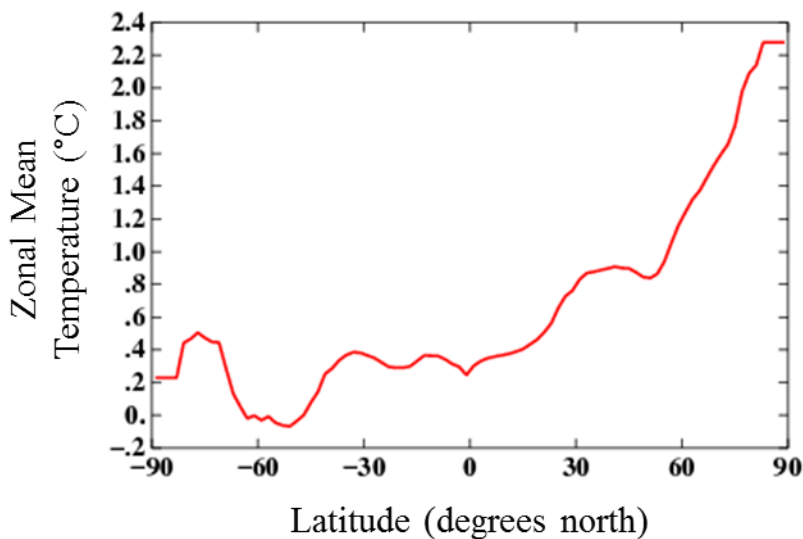
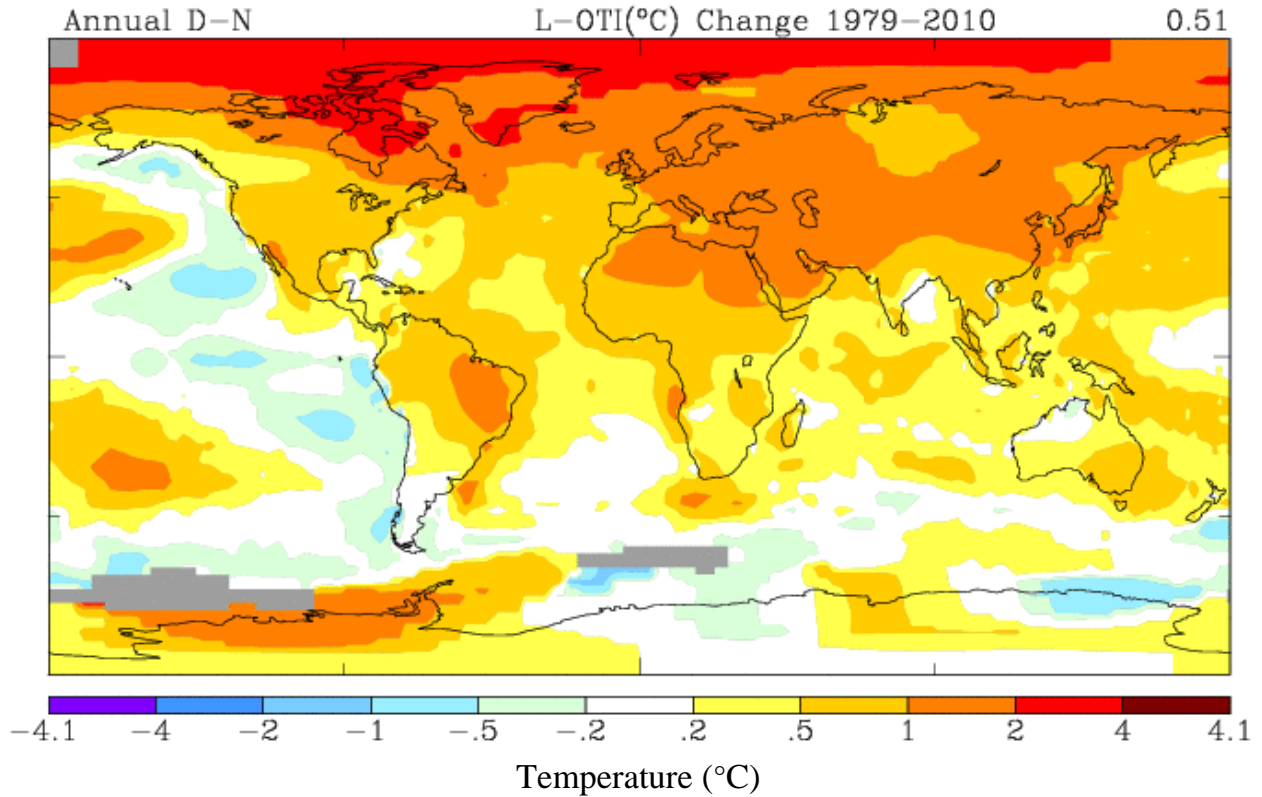


Figure 1a. Map of linear trends in annual average surface temperatures for the 32-year period from 1979 to 2010, based on data from the NASA GISS temperature analysis, found here: <http://data.giss.nasa.gov/gistemp/maps/>.

Figure 1b. Linear trends in surface temperature averaged by latitude (1979-2010) based on data from the NASA GISS temperature analysis, found here: <http://data.giss.nasa.gov/gistemp/maps/>. Note the pronounced increase in average temperatures across Arctic regions (north of 60°N) characteristic of Arctic amplification.

This observed trend of northern high latitudes warming faster than the mid-latitudes has been termed “Arctic amplification.” Arctic amplification has been at the forefront of literature in recent years and is largely thought to be linked to the observed decline in sea ice extent (Serreze et al., 2009; Screen and Simmonds, 2010; Serreze and Barry, 2011). With less sea ice, the upper layer of the Arctic Ocean absorbs more solar energy than it used to. Once the sun sets in autumn, the extra energy that the ocean absorbed is released upward, warming the atmosphere (Serreze and Barry, 2011). The ice loss rate linked to Arctic amplification has been impressive. Annual average Arctic sea ice extent has shrunk by 2.7 [2.1 to 3.3]% per decade since 1978, with larger decreases in summer of 7.4 [5.0 to 9.8]% per decade (IPCC, 2007). Winter Arctic sea ice extent historically covers about 14 to 16 million square kilometers (NSIDC, *Sea Ice*, Oct. 2013). More recently, September minimum sea ice extent reached a record low in 2012 of 3.41 million square kilometers, 44 percent below the 1981-2010 average¹, and 16 percent below the previous record in 2007, according to a National Snow and Ice Data Center report (NSIDC, *Sea Ice*, Oct. 2013). Sea ice loss and arctic amplification are intimately linked through the positive sea ice-albedo feedback mechanism (**Figure 2**). Albedo can be expressed mathematically as:

$$\alpha = \frac{S_{\text{ref}}}{S_{\text{tot}}} \quad (1)$$

where α is the albedo of a surface, often expressed as a ratio. S_{ref} represents the amount of solar energy that a surface reflects and S_{tot} represents the total solar energy incident upon that surface. A surface that is a perfect reflector has an albedo of 1; a perfect absorber (blackbody) would

¹ 1981 – 2010 is the new baseline for comparing Arctic sea ice changes as of September 2013. Previously the baseline was 1979 – 2000.

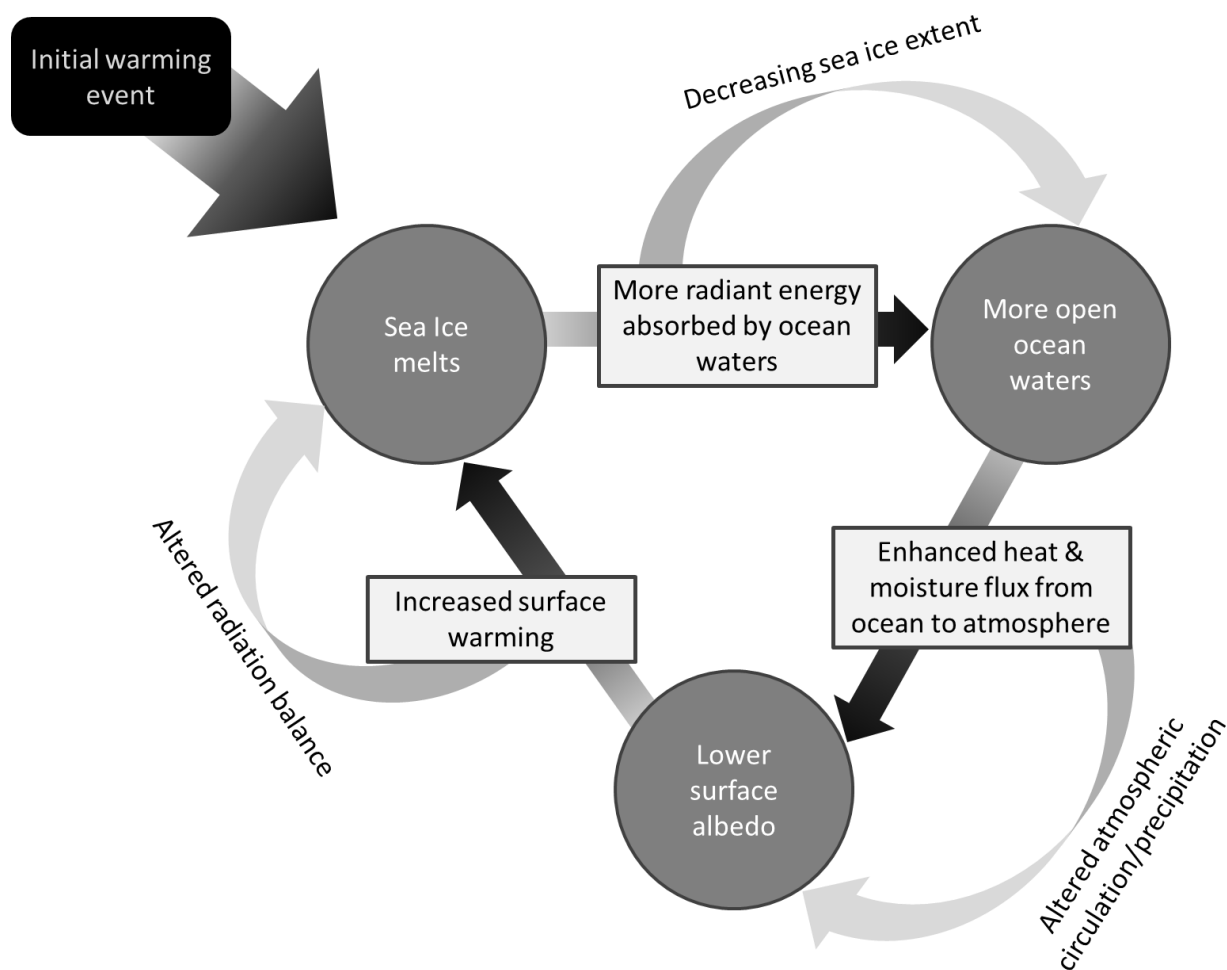


Figure 2. Schematic of the sea ice-albedo feedback mechanism with other influencing factors related to Arctic amplification process included to show how all factors are intertwined. A warming event (upper-left hand corner) initially perturbs the system. Sea ice-albedo components of the cycle are indicated by grey circles. Light grey rectangles represent surface heat/ moisture fluxes. These heat/moisture fluxes have their own impacts on related factors (curved arrows). Both the heat/moisture fluxes, as well as the additional factors they impact, have an influence on the sea ice-albedo components of the feedback cycle.

have an albedo of 0. The albedo of a surface depends upon the color, roughness, and angle of incidence of the solar radiation. Sea ice has a higher albedo ($\alpha = 0.5$ to 0.8) compared to open ocean water ($\alpha = 0.06$). As sea ice melts in summer, large areas of dark open water are exposed. These darker open waters absorb more solar energy, leading to more ice melt, and absorption of even more solar energy. With more heat in the upper ocean at summer's end, the stage is set for a large upward heat release in autumn and winter, seen as Arctic amplification.

However, the process of ice loss is quite complicated. Part of the sea ice loss can be attributed to changes in atmospheric circulation, both through thermodynamic effects (altered wind patterns affecting summer melt) and dynamic effects (altered wind patterns leading to changes in the circulation of the ice cover). Francis and Hunter (2006), in turn, find that sea ice loss can be linked to an increase in the downward longwave radiation flux to the surface, which, at least in part, can be associated with increased Arctic cloud cover, tropospheric vapor content, and more liquid-water-containing clouds (Zuidema et al., 2005) and an increase atmospheric water vapor content (Wang and Key, 2005).

It is increasingly recognized that through its impact on the Arctic energy budget, changing sea ice may itself drive changes in patterns of atmospheric circulation and precipitation across the Arctic (Simmonds and Keay, 2009; Serreze and Barry, 2011). Recently, Bintanja and Selten (2014) used statistical analysis of state of the art models from the Coupled Model Intercomparison Project Phase 5 (CMIP5) to demonstrate that increasing temperatures and declining sea ice are indeed contributing to changes in Arctic precipitation. Their analysis showed that an increase in evaporation from areas of retreating sea ice across the Arctic Ocean is the primary driver of the enhanced autumn and winter precipitation; more so than increased moisture transport from the mid-latitudes. There is also growing but controversial evidence that

some of these influences have already been observed beyond the Arctic. Francis and Vavrus (2012) used atmospheric reanalysis data to provide new evidence of the effect of Arctic amplification on large-scale atmospheric circulation. They found that that a warming Arctic may contribute to a slower progression of Rossby waves with larger amplitudes. The resultant slower circulation contributes to extremes across mid-latitudes, such as prolonged precipitation events and droughts. This thesis aims to contribute to the monitoring of Arctic precipitation and through the lens of atmospheric reanalyses.

Why study precipitation? First, precipitation is a central theme of Arctic climate change. The warming and subsequent loss of the sea ice cover is potentially important because open water provides a moisture source to the overlying atmosphere. The theory follows that increasing atmospheric greenhouse gas concentrations will lead to a warmer atmosphere, which can hold more water vapor. Global climate models (GCMs) are in general agreement that the Arctic will see increased precipitation in the future (Deser et al., 2012; Finnis et al., 2007; Kattsov et al., 2007; Stroeve, et al., 2011).

Secondly, precipitation plays a key role in the freshwater budget of the Arctic Ocean. One of the reasons why sea ice can form so readily atop the Arctic Ocean is the relatively fresh surface layer maintained by river runoff and net precipitation over the Arctic Ocean itself. Runoff ratios (runoff/precipitation) tend to be high for Arctic-draining rivers due to underlying impermeable permafrost. It is estimated that nearly 80% of the terrestrial Arctic is underlain by permafrost (Zhang, et al., 1999). Annual runoff tends to be highest in the mountains of central and eastern Siberia and the Canadian Rockies (Serreze and Barry, 2005, Chapter 6). Four major rivers – the Ob, Lena, Yenisey, and Mackenzie –contribute two-thirds of the total freshwater input into the Arctic Ocean with the latter three rivers alone contributing to approximately 57%

of the total discharge (Serreze and Barry, 2005, Chapter 6) (**Figure 3**, NOAA). Community Climate System Model, version 5 (CCSM5) simulations by Finnis et al. (2007) showed that net precipitation tended to be highest over Arctic land areas during the colder months (defined in the study as the period: September through May), which raised questions regarding the implications of changing cyclone activity on Arctic freshwater hydrology.



Figure 3. Map showing the four major Arctic drainage basins – Ob, Lena, Yenisey, and Mackenzie – with smaller basins included. Image courtesy of NOAA Arctic Change website: http://www.arctic.noaa.gov/detect/detection-images/land-arctic-rivers_gro-375.jpg.

A modeling study by Lawrence and Slater (2005) showed that freshwater discharge into the Arctic Ocean by the year 2100 could be 28% higher than today, primarily as a result of an increase in net precipitation that exceeds expected evaporation rates. In turn, 15% of the overall freshwater increase is attributed to meltwater from thawing subsurface ice (Lawrence and Slater, 2005).

Snow blankets Arctic lands for the majority of the year. In the high-Arctic, as defined by continuous permafrost, snow covers the ground surface for approximately 70% of the year (Woo and Winter, 1993). In the sub-Arctic, defined by the limit of discontinuous permafrost, snow is present between 50% and 70% of the year (Woo and Winter, 1993). Regional changes in snow cover across the Arctic are expected as precipitation patterns evolve in the future. Variations in snow cover account for the greatest changes in surface albedo, which is an important component of the Arctic heat budget and broader climate system. Snow cover acts to insulate the permafrost soils below. While above-ground air temperature changes will undoubtedly have an impact on the subsurface, a study by Stieglitz et al., (2003) highlighted the importance of snow cover on the subsurface temperature regime through catchment based land model simulations.

The Arctic contains a large store of soil carbon locked within near-surface permafrost. Concern is growing that warming and permafrost thaw will initiate a feedback whereby increased microbial activity leads to release of some of this carbon to the atmosphere, exacerbating global warming (Lawrence, et al., 2005; Zimov, et al., 2006). Station observations document increased soil warming in recent decades and later autumn freeze-up. However, it appears that soil warming is not simply a function of higher air temperatures, but is also linked to precipitation through changes in snow depth that limit winter heat loss from the soil column (Zhang, et al., 2005). Permafrost warming and deepening of the active layer – the supra-

permafrost layer which thaws seasonally (Hinzman, et al., 1991; Zhang, et al., 2005) also holds implications for changes in Arctic hydrology and ecology. Additionally, engineers must be attentive to changes resulting from thawing ground in order to assess the ability to build structurally-sound buildings as well as modify pre-existing structures in such regions.

1.2 Objectives and Scope

The central question to be addressed in this thesis is: *How has Arctic precipitation changed in recent decades?* It can be expected that changes in precipitation across the Arctic during winter months, will be primarily seen as changes in snowfall. While increase in precipitation across the Arctic might be due to the augmented moisture-holding capacity of a comparatively warmer atmosphere than in previous decades (Stroeve, et al., 2011), little is understood regarding spatial changes in precipitation, precipitation type, and the resulting impacts on the soil thermal regime (Ling and Zhang, 2004; Zhang et al., 2005).

The task of evaluating precipitation, particularly snow, across the Arctic is daunting. At special field sites, precipitation and snow cover may be recorded using meteorological stations and field measurements. Such gauge observations are incorporated into gridded datasets by blending them with satellite retrievals. Obtaining accurate measurements is extremely difficult as a result of the variability of snow depth due to topography and wind. Wind affects the efficiency of these gauges, typically resulting in an under-catch of solid precipitation (Rasmussen, et al., 2012), with errors easily ranging between 50-100% across the windswept Arctic. Along with the gauge undercatch problem, many locations are hard to access resulting in observing stations that are few and far between (Yang and Ohata, 2001; Liston and Sturm, 2002; Yang et al., 2005). Inaccessibility of many remote locations as well as the lack of a standardized observation network across political borders is another cited hindrance (Hinkel and Nelson, 2003).

Sugiura, Ohata and Yang (2006) performed an inter-comparison of solid precipitation measurement in Barrow, Alaska by examining catch characteristics for five types of precipitation gauges where they investigated the catch ratios as a function of daily mean wind speed. Sugiura, Ohata, and Yang (2006) provide a nice description regarding why windspeed is such an important factor in gauge undercatch, as follows:

Wind induced loss of precipitation is caused by the interaction between the precipitation gauge with the wind flow and snow particles falling through the air, depending on the falling particle speed, the wind speed, and the aerodynamic properties of gauge types. Since small particles are affected by viscosity more than by inertia, the wind induced loss for small snow particles may be larger than that for large snow particles. Therefore, it is reasonable for the daily catch ratio to have decreased remarkably due to wind [at our field site].

When wind speeds exceeded 6 m s^{-1} , a gentle breeze, zero catch was very frequent for unshielded gauges and overall daily catch ratios were scattered for all gauges. Data collected from March 2001 to March 2004 showed mean catch ratios of the Canadian Nipher gauge, the Russian Tretyakov gauge, and the Wyoming gauge, all of which are shielded, are 68.1%, 53.9%, and 67.6%, respectively. On the other hand, those of the unshielded Hellmann gauge and the U.S. 8-in. gauge are only 6.6% and 10.2%, respectively (Sugiura, Ohata, and Yang, 2006).

Models can incorporate such data; however, they are severely limited by sparse number of measurements and inherent errors. While models are only as good as the initial input of information, they are an important tool for assessing changes across the expansive Arctic. With a low density of measurement across the Arctic, it is crucial that the available measurements be accurate – or that we can at least quantify the undercatch and correct for it.

An attractive alternative to field or station measurements is the use of precipitation forecasts from atmospheric reanalyses (Serreze, et al., 2005). Reanalyses use both observations

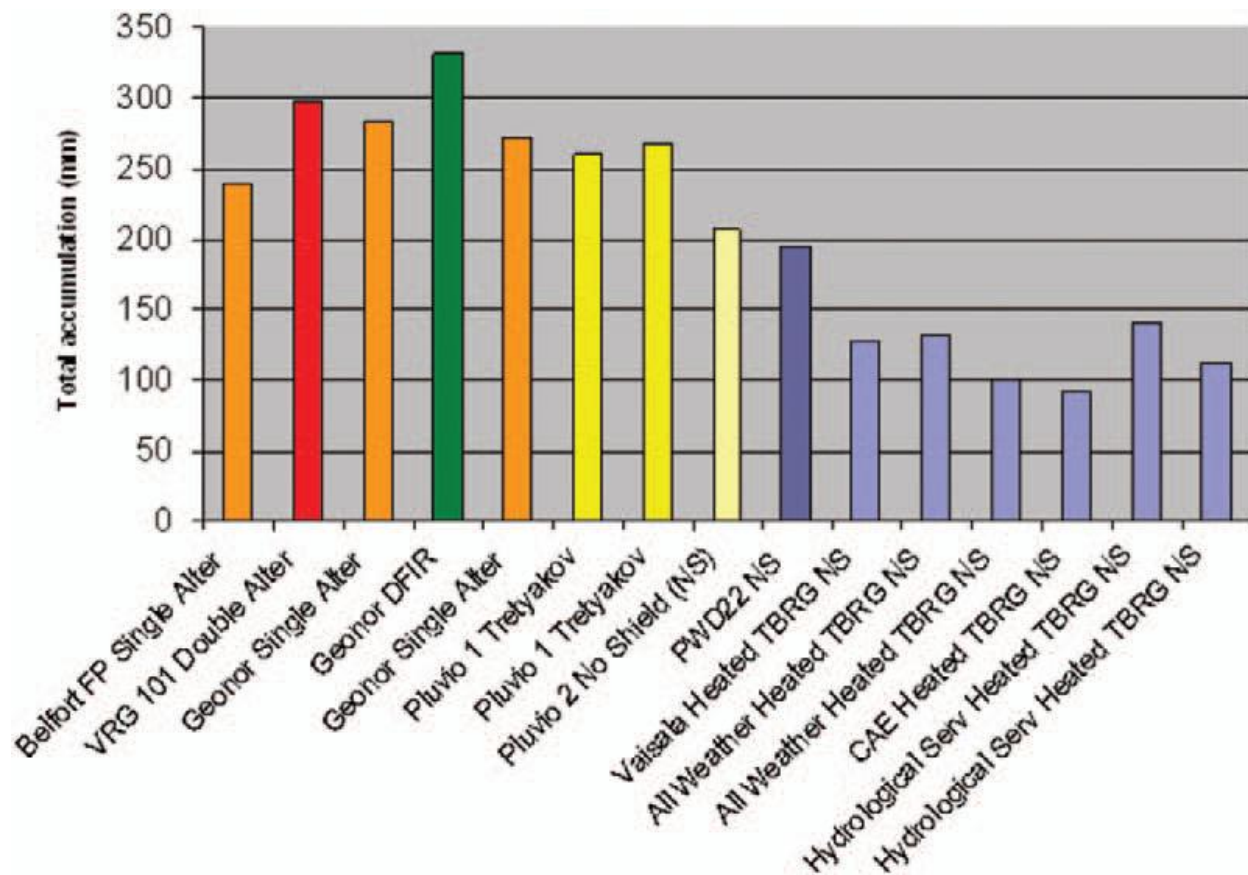


Figure 4. Bar plot highlighting the large variability of snow measurements across different gauge types for a field location in Environment Canada (EC) Centre for Atmospheric Research Experiments (CARE) near Egbert, Ontario, Canada. (Figure from Rasmussen, et al., 2012).

and equations that describe the laws of atmospheric physics to create precipitation forecasts using numerical models. Once an initial state of the atmosphere is determined for a specific point in time, the model is run producing a short-range forecast. The model forecast is submitted to checks, against new observational inputs, at designated time steps. Reanalyses are discussed in greater depth in Chapter 2.

The *first objective* of the present study is to examine spatial variability and recent trends in Arctic precipitation as represented by three modern reanalyses. The *second objective* is to validate precipitation fields from each reanalysis through comparison with station observations. Three third-generation atmospheric reanalyses are examined: (1) The National Aeronautics and Space Administration Modern Era Retrospective-Analysis for Research and Applications (MERRA; Rienecker, et al., 2011); (2) The National Centers for Environmental Prediction Climate Forecast System Reanalysis (CFSR; Saha, et al., 2010); and (3) The European Center for Medium-Range Weather Forecast ERA-Interim reanalysis (ERA-Interim; Dee, et al., 2011). Each provides a comprehensive record of climate variables spanning from 1979 until 2010. For each reanalysis, trends and recent anomalies (e.g., for the last decade) in monthly precipitation, temperature, and snowfall are examined across the entire Arctic, defined here as latitudes north of 60°N.

Biases in atmospheric reanalysis fields can be significant. Using three different reanalyses provides an estimate of uncertainty. For this study, monthly station observations from the most recent version of the Global Historical Climatology Network (GHCN; Lawrimore, et al., 2011) were used to validate the reanalysis output. The evaluation of the reanalysis outputs includes the computation of standard statistics including correlation, bias, and root-mean-square error.

1.3 Thesis Organization

Chapter 2 provides a detailed description of each of the three atmospheric reanalyses used. Chapter 3 discusses seasonality of Arctic precipitation, as well as trends and anomalies. This chapter also includes a time series analysis of coastal station data in an effort to address a major difference between ERA-interim and the other reanalyses. Chapter 4 focuses on evaluation of the reanalysis precipitation forecasts using the GHCN station data. Here the reader will find a description of the statistical methods used and mapped results. Finally, Chapter 5 provides a synthesis of the results, the author's conclusions, as well as a discussion of future research.

CHAPTER 2

ATMOSPHERIC REANALYSES

2.1 Reanalysis Systems

In climate science, a retrospective analysis – or reanalysis – is a synthesis of both observational and numerical model data, spanning an array of climate variables. This combination of data and modeled fields provides scientists with multi-decadal information on weather patterns, climate variability, and change. Variables include everything from modeled surface fields, such as precipitation, evaporation and radiation fluxes, to components of the stratosphere. The use of atmospheric reanalyses has been adopted amongst a variety of Earth system sciences. Helpful information regarding comparisons and improvements of individual reanalysis products can be found at: reanalysis.org, a regularly updated website and wiki that serves as a forum for researchers integrating reanalysis data into their studies.

Why use reanalyses to study precipitation? As briefly mentioned in Chapter 1, while station observations and remotely sensed data are important sources of information regarding precipitation in the Arctic, there are difficulties associated with their use. The gauge undercatch problem, coupled with a lack of standardization and a comparatively sparse network in relation to mid-latitude land areas, makes using station observations alone unrealistic. While satellite radiances (in the IR or microwave spectrum) are used to inform reanalyses regarding rain rates and total column water vapor, it has been demonstrated that reanalyses tend to outperform these

satellite measurements at latitudes north of 45°N (Serreze, Barrett, and Lo, 2005). Atmospheric reanalyses provide an attractive alternative.

Precipitation forecasts within atmospheric reanalysis products are produced using a Numerical Weather Prediction (NWP) model. The framework of these NWP models is a 3-dimensional grid of the atmosphere. Each grid node is assigned an initial “best estimate” of atmospheric conditions. Fundamental equations – equations describing the physics of the atmosphere – are then implemented in order to govern the evolution of the modeled atmosphere. However, due to the nonlinear nature of these equations, discrepancies between the modeled results and reality will present themselves as the forecasts extend further out into the future. Thus is the nature of in chaotic systems, which was explored in a hydrodynamical systems context by Edward Lorenz (1963). To counter this run-away tendency of the model, the observations are assimilated into the previous short-term forecast (typically a 6 hour forecast).

Parameters within reanalyses must be consistent with physical laws as well as observations, something that Dee et al. (2011) describe as physical coherence. This physical coherence is achieved through data assimilation – the process of combining observations with short-term forecasts resulting in an initial condition. In other words, the representation of precipitation by a reanalysis is related to the physics of the system itself as well as the assimilation of data. The assimilation process incorporates observational data from various sources: satellites, radiosondes, and aircraft and surface reports. The accuracy of the modeled state increases after the observations are subjected to raw data checks, quality control, and corrections. The resulting modeled state of the atmosphere is called an analysis. As the model is run forward in time, each analysis is used to inform the next consecutive forecast. Hence, by assimilating historical series of observations into a NWP model, reanalyses provide us with a

time series of these individual analyses. This assimilation process is illustrated in **Figure 5** and **Figure 6** on the following page.

The reanalyses discussed in this section utilize satellite radiance data are assimilated to create precipitation forecasts. Satellite radiance data are indirect observations of meteorological parameters. Satellites do not measure wind, or even temperature. Satellite instruments (active and passive) measure the amount of radiation (radiance) that reaches the top of the atmosphere (TOA) at a certain frequency. Radiances are often reported in terms of brightness temperature. Using satellite radiance data is particularly useful because it eliminates the introduction of errors linked to pre-processing of data – such as angle adjustments or surface corrections. Finally, it allows for consistent treatment across data used in reanalyses.

A number of atmospheric reanalyses exist. *So which reanalysis is best to use?* The answer is highly dependent upon which variables and latitudes are of interest to the user as each reanalysis differs in terms of assimilation methods, modeling algorithms, and the spatial grid used. Individual reanalyses have their own inherent biases, all of which may or may not be easily identifiable. While reanalyses are commonly used for investigations of the Earth's climate system, challenges remain in coupling each of the system's components (Bosilovich, et al., 2012). Observations are a key resource in producing reanalyses; however, regardless of improvements to observations, forward models, and analysis schemes, biases remain an issue (Treadon, et al., 2002).

Observations are irregular in both space and time and such irregularities and scarcities of observations are especially prominent in Arctic regions. As discussed above, the observations are synthesized within the model during the data assimilation step to create an analysis and a short term forecast. One of the key utilities in a reanalysis is that the output generated from the model

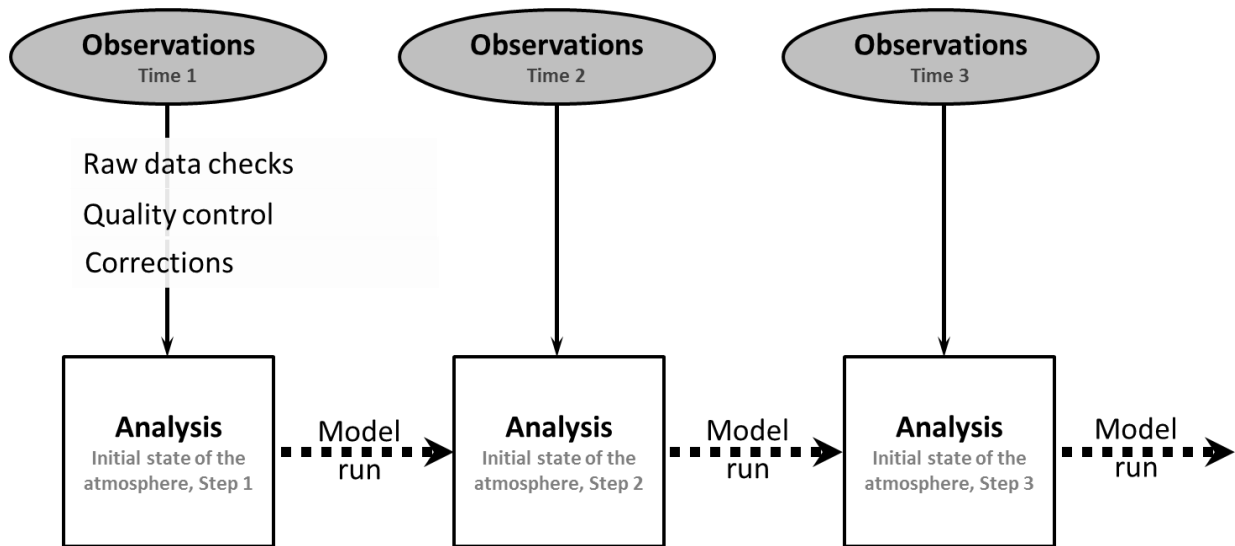


Figure 5. Schematic of the data assimilation process in a NWP model. Throughout the data assimilation process, observations are used to inform the model at each step. The caliber of the observational data used is very important.

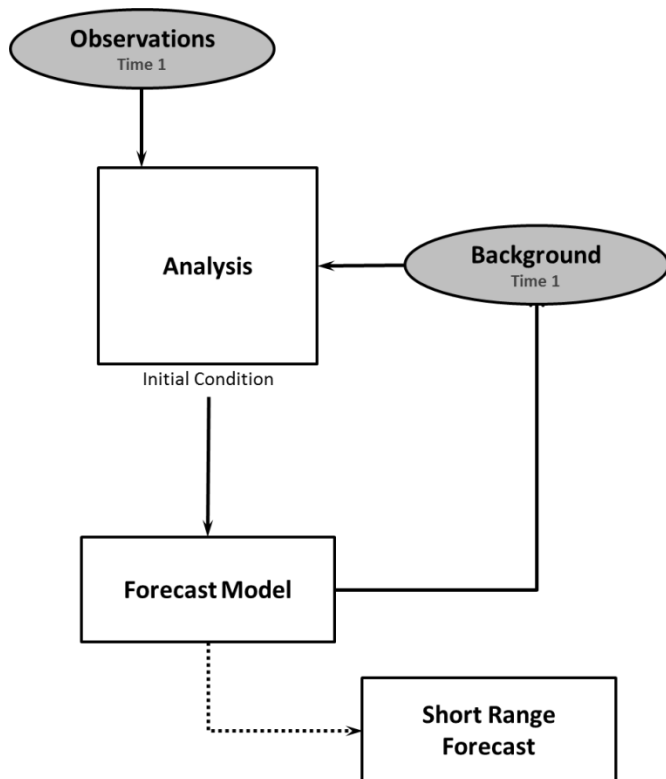


Figure 6 (left). The diagram shows of one full analysis cycle during the data simulation process within a NWP model. NWP models are constrained by the assimilation of observations.

physics (e.g., precipitation, evaporation) are variables that are not easily observed, but *are* consistent with the analyzed observed data (Bosilovich, et al., 2008). Therefore, while the real-world observations act as a guide, the model physics, uncertainties, and related errors will inevitably still lead to some degree of uncertainty in the resultant data products.

In this study, three third-generation atmospheric reanalyses are utilized to explore changes in Arctic precipitation for the 32 year (384 month) period between January 1, 1979 and December, 31 2010. Third-generation reanalyses use advanced data assimilation approaches and models compared to previous generations. Seen as improved versions of earlier reanalyses, these third-generation reanalysis products are typically used in place of earlier products and therefore make practical subjects for this validation study. The reanalyses of concern in this thesis have data available for the entire globe, but for the purposes of this project, only the area north of 60°N latitude is examined. The three atmospheric reanalyses are:

- 1.) Modern Era Retrospective Analysis for Research and Applications,
- 2.) Climate Forecast System Reanalysis,
- 3.) European Centre for Medium-Range Weather Forecasts Reanalysis-Interim.

Specifics regarding the precipitation data and sources for each reanalysis product used in this thesis are provided in **Table 1**. Conventional observations sources and suppliers for precipitation data used within all three of the reanalysis products are listed in **Table 2**.

Table 1. Information regarding the web sources and data from each reanalysis product used.

	MERRA	CFSR	ERA-Interim
Product Source	NASA/GMAO	NOAA/NCEP	ECMWF
Data Download	http://disc.sci.gsfc.nasa.gov/mdisc/	http://rda.ucar.edu/datasets/ds093.2/	http://data-portal.ecmwf.int/data/d/interim_full_mnth/
Spatial Resolution	0.5° N x 0.66° E	0.5° N x 0.5° E	0.75° N x 0.75° E
Temporal Range	Jan-01-1979 to Dec-31-2010	Jan-01-1979 to Dec-31-2009	Jan-01-1979 to Dec-31-2010
Variable Name	Total Precipitation (PRECTOT)	Precipitation Rate (PRATE)	Total Precipitation
Variable Units	kg m ⁻² s ⁻¹	kg m ⁻² s ⁻¹	m

Table 2. Conventional observations (excluding satellite radiance data), time range, and sources used to inform the model regarding precipitation for each reanalysis. Details regarding the GHCN dataset are included for comparison. Information used in this table was taken from: Lucchesi (2012), Saha, et al. (2010), and Tavolato and Isaksen (2010).²

	Data Source	Period	Data Supplier
GHCN	Meteorological stations	varies, 1930s - 2010	NOAA/NCDC
MERRA	Radiosondes	1970 - present	NOAA/NCEP
	Dropsondes	1970 - present	NOAA/NCEP
	Land surface observations	1970 - present	NOAA/NCEP
	Ship and buoy observations	1977 - present	NOAA/NCEP
CFSR	CAMS (pentad)	1979 - present	NOAA/CPC
	CPC unified global daily gauge analysis (retrospective)	1979-2005	NOAA/CPC
	CPC unified global daily gauge analysis (real time)	2006-present	NOAA/CPC
ERA-Interim	Radiosondes	?	NCAR/NCEP
	Land surface observations	?	?
	COADS (ship and buoy observations)	1979-1998	NCAR

² The author was not able to pinpoint every observational source for ERA-Interim. Appropriately, Dick Dee himself has even brought this problem up stating: “In particular, it should be made much easier for a user to get detailed information about the observations used in reanalysis, including the quality assessment and bias adjustments produced by the reanalysis process itself.” (UCAR reanalysis page, March 2012).

2.1.1 MERRA

The Modern Era Retrospective Analysis for Research and Applications (MERRA; Rienecker et al., 2008; Lucchesi, 2012) is a product of the Global Modeling and Assimilation Office (GMAO) within the National Aeronautics and Space Administration (NASA). The horizontal and vertical resolution of the MERRA output used in this project is 0.5° N x 0.66° E with 72 hybrid-sigma coordinate vertical levels. Monthly MERRA data (Total Precipitation, PRECTOT, $\text{kg m}^{-2} \text{ s}^{-1}$) are available through Goddard Earth Sciences (GES) and can be downloaded from the Modeling and Assimilation Data and Information Services Center (MDISC) website, at: <http://disc.sci.gsfc.nasa.gov/mdisc/>. Within MERRA precipitation, both rain and snow fall uniformly across all sub-grid surface types and are defined everywhere. This is of note, as other land budget variables are only defined over grid cells that have a non-zero land fraction (Lucchesi, 2012).

MERRA uses the Goddard Earth Observing System Model, Version 5 (GEOS-5) and data assimilation system (DAS) (Rienecker, et al. 2008). The GEOS-5 model is an atmospheric general circulation model (AGCM) with a finite-volume dynamical core. Its capabilities encompass both weather and climate modeling; it is currently used for numerical weather prediction and atmospheric analyses (Rienecker, et al. 2008). GEOS-5 includes changes that have been made to both the general atmospheric circulation model as well as the analysis system. Within MERRA, the model produces observational analyses at 6-hour intervals. GEOS-5 is coupled to a catchment-based hydrologic model (Koster, et al., 2000) and a multi-layer snow model (Stieglitz, et al., 2001).

The DAS integrates the GEOS-5 atmospheric model with Gridpoint Statistical Interpolation analysis (GSI; Hu, et al., 2009). GSI is a joint analysis system developed by the

NOAA/NCEP and the NASA/GMAO. GSI analysis is a three-dimensional, variational (3D-Var) data assimilation system which was developed to integrate atmospheric observations with background fields in order to produce an initial field for global or regional models (Hu, et al., 2009). Such three- or four-dimensional analyses can be thought of as “a generalization of physical retrieval to include all types of data and spatial and temporal variability” (Derber, et al., 2010). GEOS-5 DAS implements Incremental Analysis Updates (IAU; Bloom et al., 1996), which is a method used to slowly adjust the modeled states toward the observed states. The IAU procedure – in which dynamically consistent, one-hourly forecasts are corrected against observations at six-hour intervals – has improved precipitation spin-down during early stages of the forecast (Cullather and Bosilovich, 2011).

As a whole, precipitation within MERRA is model generated, but is still informed by the analysis. Satellite radiances from NOAA-NASA Geostationary Operational Environmental Satellite (GOES) and NOAA’s High Resolution Infrared Radiation Sounder (HIRS) and Advanced Microwave Sounding Unit (AMSU) radiometers aboard NASA’s Aqua satellite provide atmospheric moisture information (Treadon, et al., 2002; Lucchesi, 2012). Over the oceans, precipitation assimilation within GEOS-5 DAS utilizes radiance information to derive rain rates from the Special Sensor Microwave/ Imager (SSM/I) and the Tropical Rainfall Measuring Mission Microwave Imager (TMI), where it contributes to the water vapor analysis. (M.G. Bosilovich, personal communications). This however, is restricted to locations between 60° N and 60° S. This is the result of quality control checks. Treadon, et al. (2002) found that quality control bounds decrease to zero for observations poleward of 45° latitude; therefore, satellite observations are not used over snow or land ice, ice covered water, or locations poleward of 60° latitude (Rienecker, et al. 2008). Further details regarding quality control studies

related to precipitation assimilation can be found in Treadon, et al. (2002) and Okamoto and Derber (2006). Over land, conventional observations of precipitation include radiosondes, dropsondes, land surface observations, and ship/buoy observations (Lucchesi, 2012) which are not broadly restricted by latitude (Bosilovich, personal communications).

The three reanalysis products emphasized in this thesis do not assimilate gauge or surface observations for precipitation. However, MERRA-Land, an “off-line” extension of the MERRA project has been developed by NASA with the aim of assisting land surface hydrology studies, combines a gauge based precipitation product with MERRA precipitation. MERRA-Land data are available for year 1980 through present. More information and data access can be found here: <http://gmao.gsfc.nasa.gov/research/merra/merra-land.php>.

2.1.2 CFSR

The Climate Forecast System Reanalysis (CFSR; Saha, et al., 2010) is a product of the U.S. National Centers for Environmental Prediction (NCEP) and NOAA. The spatial resolution of the CFSR output used here is 0.5° N x 0.5° E. The spectral resolution is ~ 38 km (T382) with 64 levels extending from the surface to 0.26 hPa. The regular monthly CFSR data (Precipitation Rate, PRATE, $\text{kg m}^{-2} \text{ s}^{-1}$) was downloaded from the University Corporation for Atmospheric Research (UCAR) website, at: <http://rda.ucar.edu/datasets/ds093.2/>. Monthly precipitation rate is computed as an average of forecast averages with equal duration and six hour intervals between forecasts. Currently, the regular long-term mean data for CFSR are available through December 2009. There are efforts being undertaken by NCAR to extend these data through December 2010; however, currently CFSR monthly data only extends from 1979 through 2009. While this is not ideal, missing only one year out of the entire 32-year analysis period will not have drastic impacts on this study and so this 31-year period is used for CFSR data.

As discussed by Saha, et al. (2010), the two previous NCEP atmospheric reanalyses – NCEP/NCAR Reanalysis (R1) and its corrected version (R2) – differ from the newer CFSR in the following ways: “the sigma coordinate system (Phillips, 1957) of the global spectral model previously used was replaced with a hybrid sigma-pressure system (Juang, 2005). The Spectral Statistical Interpolation (SSI) analysis system was replaced by the GSI (Kleist, et. al, 2009a).” For atmospheric analysis, CFSR uses a GSI scheme very similar to that used by MERRA. Further details regarding the GSI configuration and testing after it was implemented into the NCEP Global Data Assimilation System is found in Kleist, et al., (2009b).

Within CFSR there is a land surface analysis. This is a notable contrast from MERRA which contains no land surface analysis. The land surface model (LSM) used in CFSR is the Noah LSM (Ek, et al., 2003). Noah is implemented in both a fully- and semi- coupled system: 1.) the fully coupled land-atmosphere-ocean model, which interacts with the reanalysis at each time step, makes the first guess land-atmosphere simulation, and 2.) the semi-coupled CFSR Global Land Data Assimilation System (GLDAS), which interacts with the reanalysis once daily, performs the land surface analysis. GLDAS is forced with CFSR atmospheric data assimilation output and observed precipitation analyses as direct forcing (Saha, et al., 2010). Previously, R1 and R2 used different approaches, as described by Saha, et al. (2010): “using precipitation from the assimilating background atmospheric model (R1), or using observed precipitation to ‘nudge’ soil moisture (R2)”. Another improvement of CFSR over R2 is the direct assimilation of satellite radiances (Saha, et al., 2010); note that GEOS-5, within MERRA, also assimilates satellite radiances rather than retrievals (Rienecker, et al. 2008).

Conventional and satellite observations are included in CFSR and two sets of global precipitation analyses are used in the CFSR land surface analysis (Saha, et al., 2010). First, is the

CPC Merged Analysis of Precipitation (CMAP; Xie and Arkin, 1997), which is a global, gridded product that defines 5-day averages of precipitation on a 2.5° latitude/longitude grid. CMAP utilizes both satellite and gauge observations. It is important to note that the input data sources to make these analyses are not constant throughout the period of record, 1979 to present. Second, is the CPC unified global daily gauge analysis, which is first interpolated on 0.125° latitude/longitude, then averaged on 0.5° latitude/longitude grid over global land (Xie, et al., 2007).

2.1.3 ERA-Interim

The European Centre for Medium-Range Weather Forecast's (ECMWF) interim reanalysis product (ERA-Interim; Dee, et al., 2011) was originally meant to serve as a temporary product while an updated version of the ERA-40 reanalysis was created. It is now continuing as an ECMWF climate data assimilation system (ECDAS) until it is superseded by a new extended reanalysis (Simmons, et al., 2007a,b; Tavolato and Isaksen, 2010). ERA-Interim spans from 1979 through present day and is updated monthly. The spatial resolution of the ERA-Interim output used here is 0.75° N x 0.75° E. The spectral resolution is ~80 km (T255); compared to ERA-40's spectral resolution of T159 (Dee, et al., 2011). There are 60 vertical levels and 37 pressure levels. Monthly ERA-Interim data (Total Precipitation, m) were downloaded from: http://data-portal.ecmwf.int/data/d/interim_full_mnth/. ECMWF provided instructions for calculating the monthly means from the available daily averaged fields; these instructions can be found on the data FAQ page. At the time of this analysis the monthly mean precipitation fields had not yet been made available on the ECMWF website. Thus, the recommended procedure was followed in order to calculate monthly precipitation for all 384 months in the study period.

ERA-Interim is produced using a forward-advancing data assimilation scheme consisting of 12-hourly analysis cycles. The ERA-Interim archive currently contains 6-hourly gridded estimates of three-dimensional meteorological variables, and 3-hourly estimates of surface parameters (Dee, et al., 2011). ERA-Interim benefits from an improved assimilation system compared to ERA-40 from 1989 onwards. The ECMWF's operational assimilation system has improved considerably since its inception in 1997 (Tavolato and Isaksen, 2010); such improvements have led to better forecast ability (Simmons and Hollingsworth, 2002).

One of the major differences that sets ERA-Interim apart from the ERA-40 reanalysis as well as MERRA and CFSR is ECMWF's operational four-dimensional variational (4D-Var) data assimilation system. Data from microwave imagers in cloudy and rain-affected areas are assimilated as total column water vapor estimates. The process follows 1D+4D-Var which is described further by Dee et al. (2010). Both CFSR and MERRA use 3D-Var assimilation methods – via GSI – with MERRA also employing incremental updates via IAU.

Like the two previous reanalyses discussed, ERA-Interim also utilizes SSM/I derived radiances, with the most noticeable impact of integrating such observations being over oceans. ERA-Interim does not use TMI radiance information. Temperature and humidity measurements from conventional radiosondes and land-based meteorological stations are used across land areas to inform the model about precipitation events (Dee, et al., 2011). Data from ships and buoys from the Comprehensive Ocean Atmosphere Data Set (COADS; Woodruff, et al., 1987) dataset are used between 1979 and 1998; post-1998 data usage drops due to changes in observation distribution and related biases (Tavolato and Isaksen, 2010). For more details regarding quality control and observations utilized by ERA-Interim, the reader is referred to the technical report by Tavolato and Isaksen (2010).

CHAPTER 3

ARCTIC PRECIPITATION

3.1 Seasonality of Precipitation

The Arctic is a place of stark seasonal contrasts, with long dark winters and nightless summers. Apart from the Atlantic sector of the Arctic that is influenced by frequent cyclone activity and open ocean waters, winter tends to be a cold and dry season. As the spring sun peeks over the horizon and climbs higher in the sky, the sea ice cover wanes in extent. Open ocean water provides an abundant moisture source for the atmosphere, and convective precipitation becomes common over land areas during summer. By autumn, lower temperatures return as the sun sinks below the horizon and the growing sea ice cover caps the warm ocean surface, causing a sharp decline in water vapor flux to the atmosphere as the long winter begins.

Maps of long-term mean precipitation totals over the Arctic for each month are displayed in **Figure 7**. The maps were created using MERRA reanalysis output. Serreze and Barry (2005, Chapter 6, Figure 6.3) showed mean seasonal precipitation using a NCEP/NCAR reanalysis forecasts blended with various station datasets for the four mid-season months; overall MERRA (**Figure 7**), CFSR, and ERA-Interim output for the past 32 years reproduces these seasonal patterns. Intercomparison of the average fields showed that all three reanalyses capture the major known features of Arctic precipitation, including:

- 1) Peak annual totals over the Atlantic side of the Arctic linked to the Icelandic Low, the North Atlantic storm track and a consistent moisture source;

- 2) Low annual totals over the Canadian Arctic Archipelago, eastern Siberia and the central Arctic Ocean, reflecting continentality;
- 3) Contrasting seasonal cycles over land are (summer maximum, winter minimum) and the Atlantic sector (winter maximum, summer minimum).

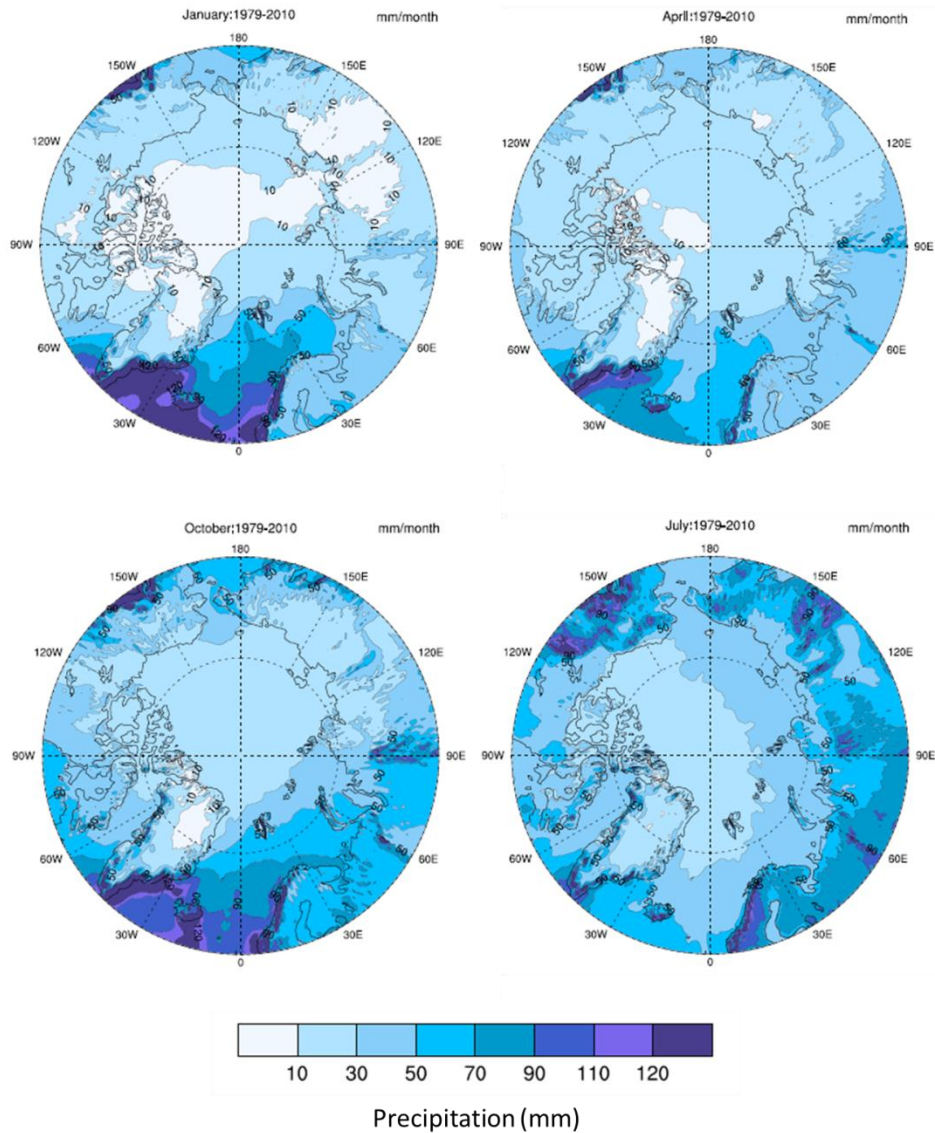


Figure 7. Average precipitation for the mid-season months: January, April, July and, October (starting at the upper left-hand corner moving clockwise) using MERRA data. Darker shades represent greater precipitation amounts.

Overall, MERRA precipitation averages do tend to agree (within +/-10 mm for January and +/- 40 mm for July) with the average precipitation values in the blended outputs published in Serreze and Barry (2005, Chapter 6, Figure 6.3).

3.1.1 Winter

Winter corresponds with the time when the tropospheric pressure and north-south temperature gradient between the equator and poles, and hence the poleward transport of atmospheric energy, is strongest. Much of this energy transport is accomplished by synoptic scale cyclones.

In general, the Atlantic sector (Fram Strait, Norwegian Sea, Barents Sea) has the highest precipitation totals due to the presence of the North Atlantic cyclone track and a consistent moisture source. Activity is strongest in the vicinity of the wintertime Icelandic Low, the semi-permanent center of low pressure that, on average, lies between the southern tip of Greenland and Iceland (~61 to 67°N) (**Figure 8a**). This region is particularly favorable to cyclogenesis and cyclone deepening due to its position downstream of the eastern North American longwave trough, the presence of warm open waters, vorticity generation in the lee of the Greenland ice sheet, and sharp horizontal temperature gradients along the sea ice margin. January precipitation totals in the North Atlantic range between 70 to 120+ mm, but locally, such as along the southeastern coast of Greenland, averages may reach 150 mm for the month (**Figure 7, January**). These high totals, as well as those along the Scandinavian coast, reflect orographic effects as moist air masses are lifted abruptly from sea-level.

Winter is a relatively dry season for most other Arctic locations. Across north-central Eurasia, the strong Siberian High maintains dry conditions and frigid temperatures. Another

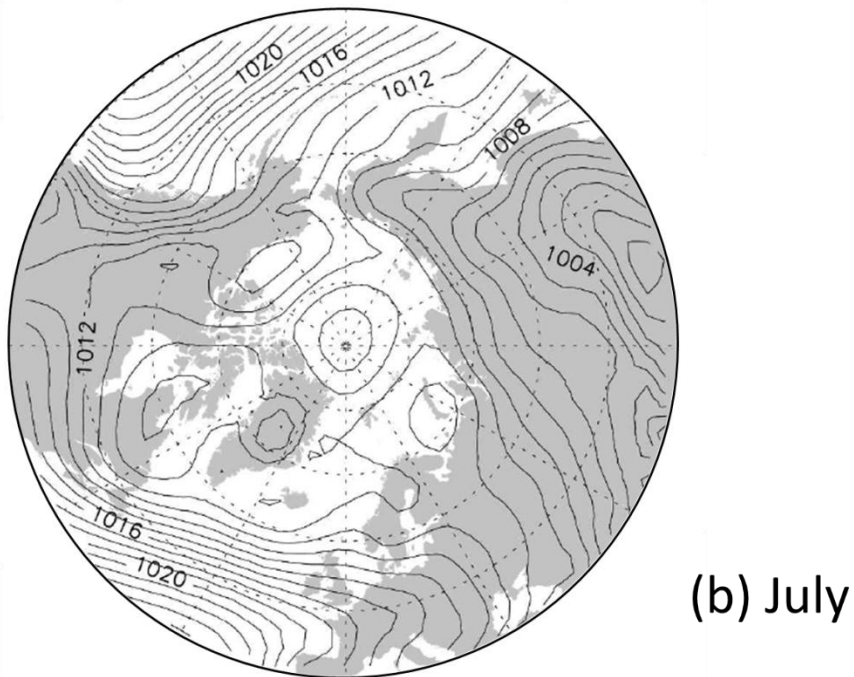
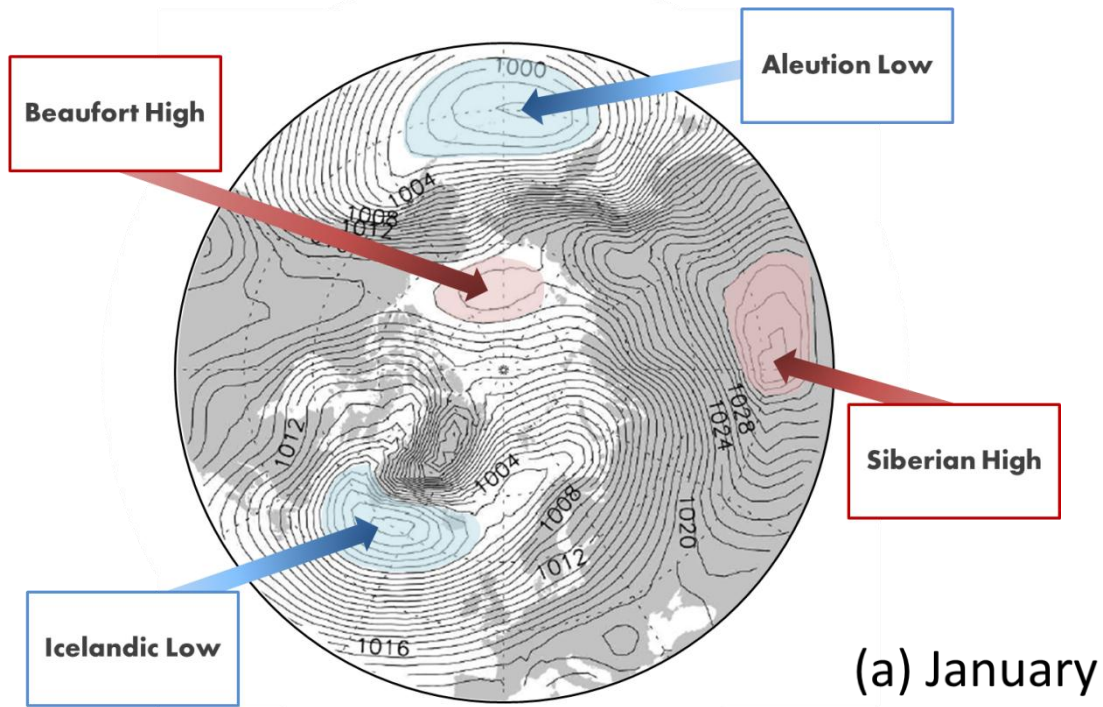


Figure 8. Fields of sea level pressure (hPa) for January (top) and July (bottom). The shifts in the positions of major high and low pressure centers are linked to seasonal changes in precipitation across the Arctic. This figure is adapted from Serreze and Barrett (2008).

center of high pressure – the Beaufort High – sets up north of Alaska. The Beaufort and Siberian Highs are separated by a ridge of high pressure extending from 250° E (over Canada), arching across the Arctic Ocean, and along 140°E (over Russia) (**Figure 8a**). It is this surface pressure set up, along with distance from moisture sources (continentality) that helps explain why central Eurasia, northern Canada and Alaska, as well as the central Arctic Ocean, tend to see minimal precipitation during winter. Wintertime precipitation averages across the Canadian Arctic Archipelago, the central Arctic Ocean, and north-central Eurasia average 10 mm or less (**Figure 7, January**). Particularly low precipitation values over north and central Greenland, compared to its south-eastern coastline, are due to continentality.

3.1.2 Spring

Spring in the Arctic brings increasing solar radiation as the sun rises higher and higher above the horizon. By spring, the Atlantic sector sees a noticeable decrease in precipitation compared to winter. This is due to the weakening of the Icelandic low and North Atlantic storm track. Precipitation over such terrestrial locations as Alaska, northern Canada, and Siberia remains low, with averages ranging between 10 and 30 mm (**Figure 7, April**). Central Arctic Ocean precipitation totals remain low, with averages of 10 to 30 mm for the month. Western Europe and Scandinavia see an increase in precipitation compared to winter, with totals ranging from approximately 30 to 50 mm.

3.1.3 Summer

In response to the more even latitudinal distribution to solar heating during summer, the atmospheric temperature gradient between the middle and high latitudes is at its seasonal minimum. The North Atlantic cyclone track is consequently much weaker compared to winter.

There are two separate low pressure centers over Baffin Island and another west of Iceland (**Figure 8b**). The long duration of sunlight contributes to increased evaporation rates and consequently greater atmospheric moisture. While solid precipitation is less frequent in mid-summer, is it not unusual for locations in the Central Arctic Ocean nearest the pole to see snow in July or August. Precipitation at lower latitudes falls almost entirely as rain during the summer.

July precipitation averages (**Figure 7, July**) for the North Atlantic sector average 50 to 70 mm. The central Arctic Ocean sees less precipitation than the continents, with averages ranging between 10 mm and 30 mm. Precipitation totals over continental regions are at their seasonal maximum during summer; a stark contrast to winter. These changes are a reflection of changes in synoptic activity as well as convection (Serreze, et al., 1993; Serreze, 1995). July precipitation averages across east-central Eurasia, north-central Canada, and the North Slope of Alaska range from 50-90 mm. Higher totals are seen across southern and central Alaska (>90 mm); lower totals are the norm across the Canadian Arctic Archipelago (~30 to 20 mm). This can be partially attributed to the summer Arctic frontal zone (extending 65° to 170°E) which is especially prominent over northeastern Eurasia (roughly the 65°–70°N, 140°–170°E region) (Serreze and Barrett, 2008). The Arctic frontal zone is a seasonal feature that is the result of the atmospheric heating differences over the Arctic Ocean and snow-free land that promotes cyclogenesis.

3.1.4 Autumn

Precipitation over the Central Arctic Ocean tends to peak in mid-September; around the time of annual the sea ice minimum. This coincides with a maximum of ice-free ocean waters, which serve as a moisture source to the atmosphere. Cyclone activity begins to increase across the Arctic Ocean thanks to storms tracking across Eurasia and the North Atlantic. During this

time, the central Arctic Ocean sees precipitation totals of 30 mm or less (**Figure 7, October**). The North Atlantic sector sees an increase in precipitation compared to summer, with averages ranging from 50 to 90 mm, with locally higher amounts (120 mm) along the south-eastern Greenland coast and the waters south of Iceland (**Figure 7, October**). This pattern manifests the seasonal transition back to the wintertime pattern the high pressure centers over land areas and strengthening of the North Atlantic cyclone track and Icelandic Low.

3.2 Recent Precipitation Changes

While the observed sharp decline in end-of-summer sea ice extent is in part a response to Arctic warming, it also contributes to the warming in autumn and winter, and may consequently influence the seasonal and spatial distribution of precipitation. Heat gained by the open ocean waters in summer is released back to the atmosphere in autumn and winter. This expanse of open water also represents a moisture source. It is in this way that changing sea ice distribution, affected by the positive feedback of warming, can affect horizontal temperature gradients, and hence storm formation and tracks.

3.2.1 Methods

Long-term monthly precipitation trends were plotted using least-squares regression. Determining the statistical significance to the trends was accomplished using the incomplete beta function. The function ratio is the probability that a random variable from a beta distribution, with parameters a and b will be less than or equal to c ; where c equals:

$$c = \frac{df}{df + (tval)^2} \quad (2)$$

In Equation 2, df is the degrees of freedom ($df = n - 2$) and $tval$ are the t -values for each grid node calculated from the student's t -distribution. In this case, $a = df/2$ and $b = 0.5$. This function can be used to calculate the p -values for a student t -test. This also comes as a prewritten function in NCL (betainc); the function code used is from SLATEC (<http://www.netlib.org/slatec/fnlib/>).

Figures 9, 10, and 11 show the trends for each month for MERRA, CFSR, and ERA-Interim output, respectively. When referring to specific seasons, three-month seasons are assumed and are abbreviated as follows: winter (DJF), spring (MAM), summer (JJA), autumn (SON). Significant trends at the 95% level ($p < 0.05$) are designated by crosshatching.

To highlight recent precipitation changes compared to the long-term averages, decadal anomalies (2001-2010) for were also calculated for each season. Anomalies were calculated by first computing the seasonal averages for the entire 32-year time period (1979-2010) and calculated the departures for the 10 year seasonal averages from the long-term seasonal averages. **Figure 12** shows decadal anomalies the three month winter season (DJF), **Figure 13** shows decadal anomalies the three month spring season (MAM), **Figure 14** shows decadal anomalies the three month summer season (JJA), **Figure 15** shows decadal anomalies the three month autumn season (SON). These figures can be found at the end of the results section of this chapter.

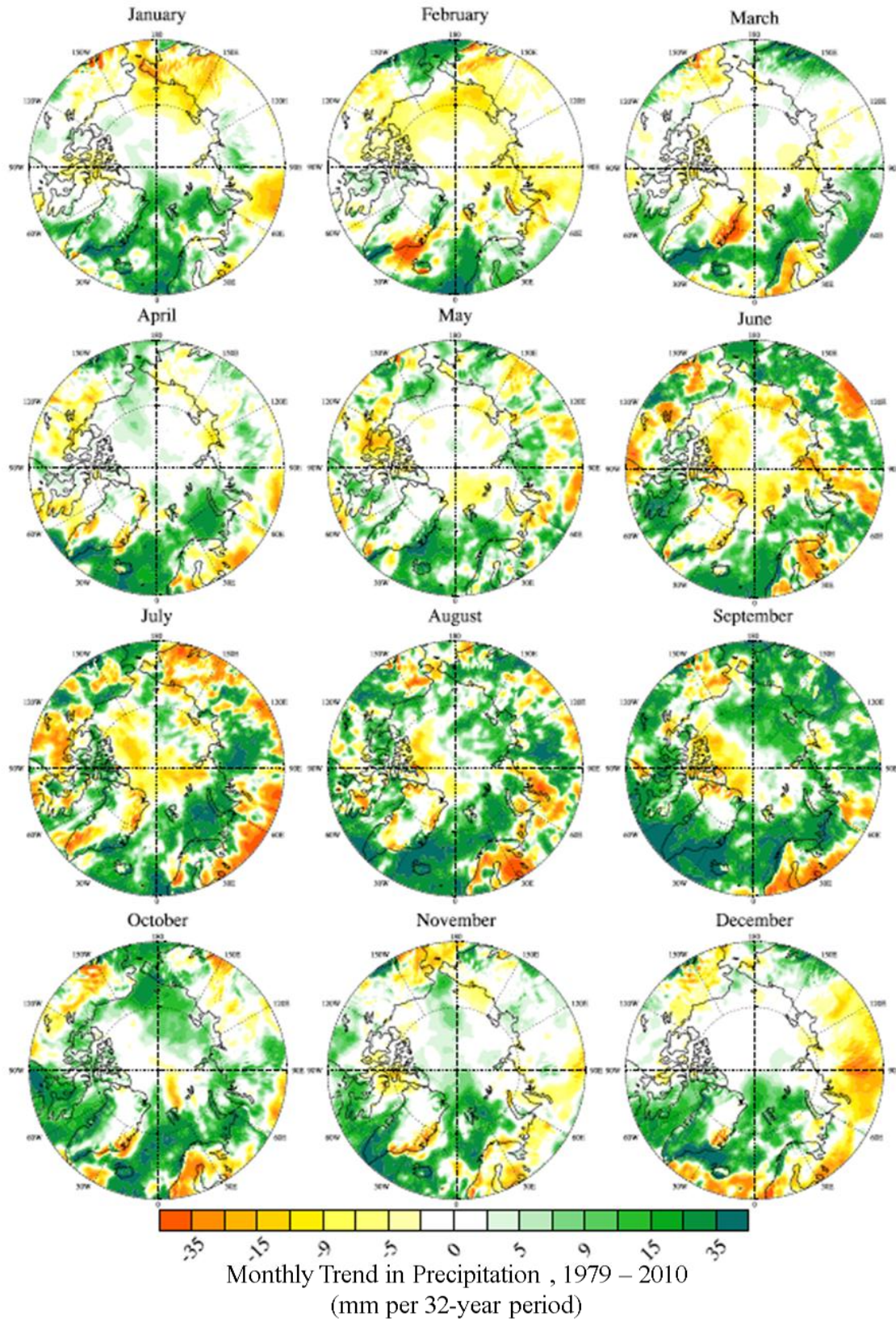


Figure 9. Plots of monthly precipitation trends, for 1979 – 2010, as represented by MERRA.

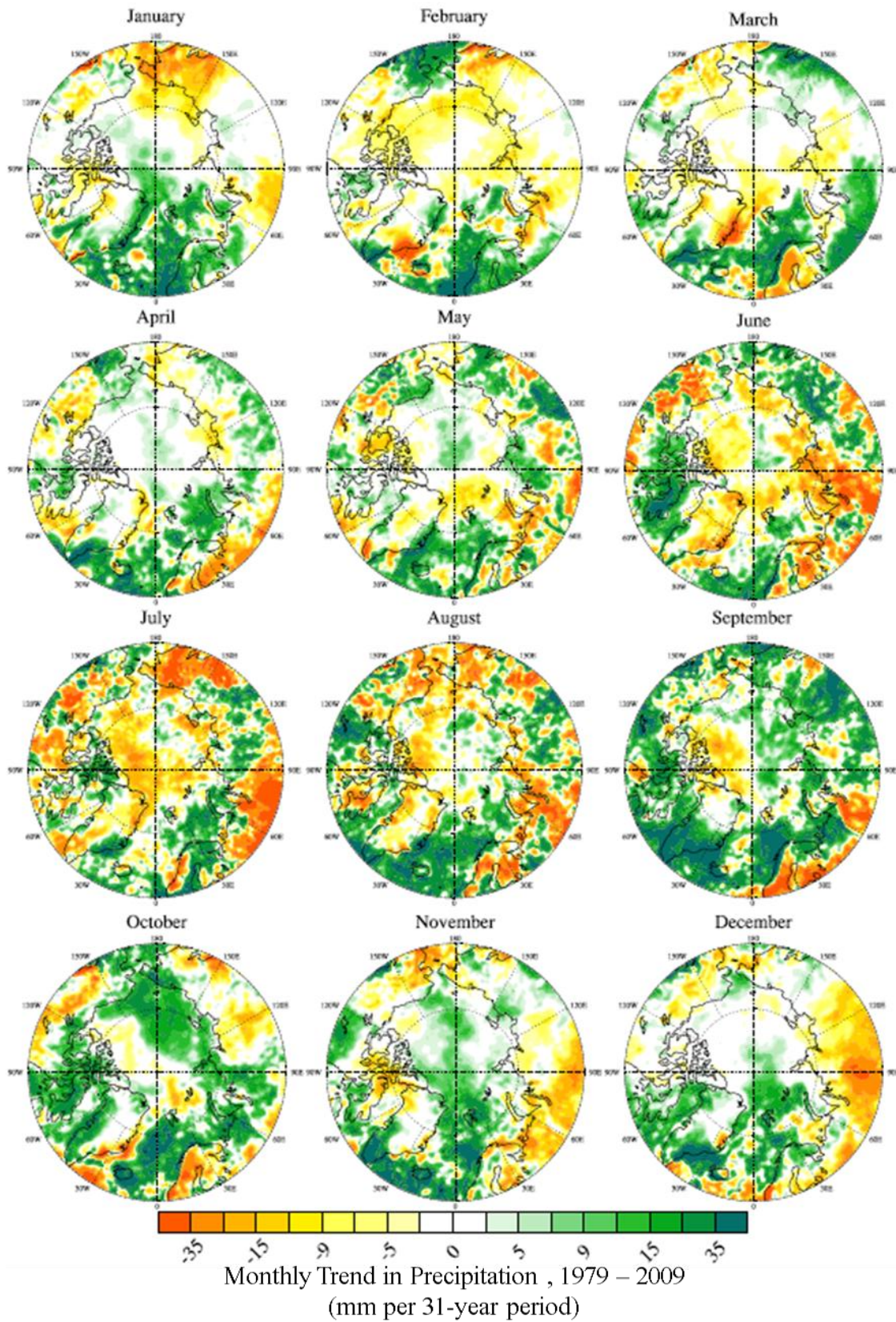


Figure 10. Plots of monthly precipitation trends for 1979 – 2009, as represented by CFSR.

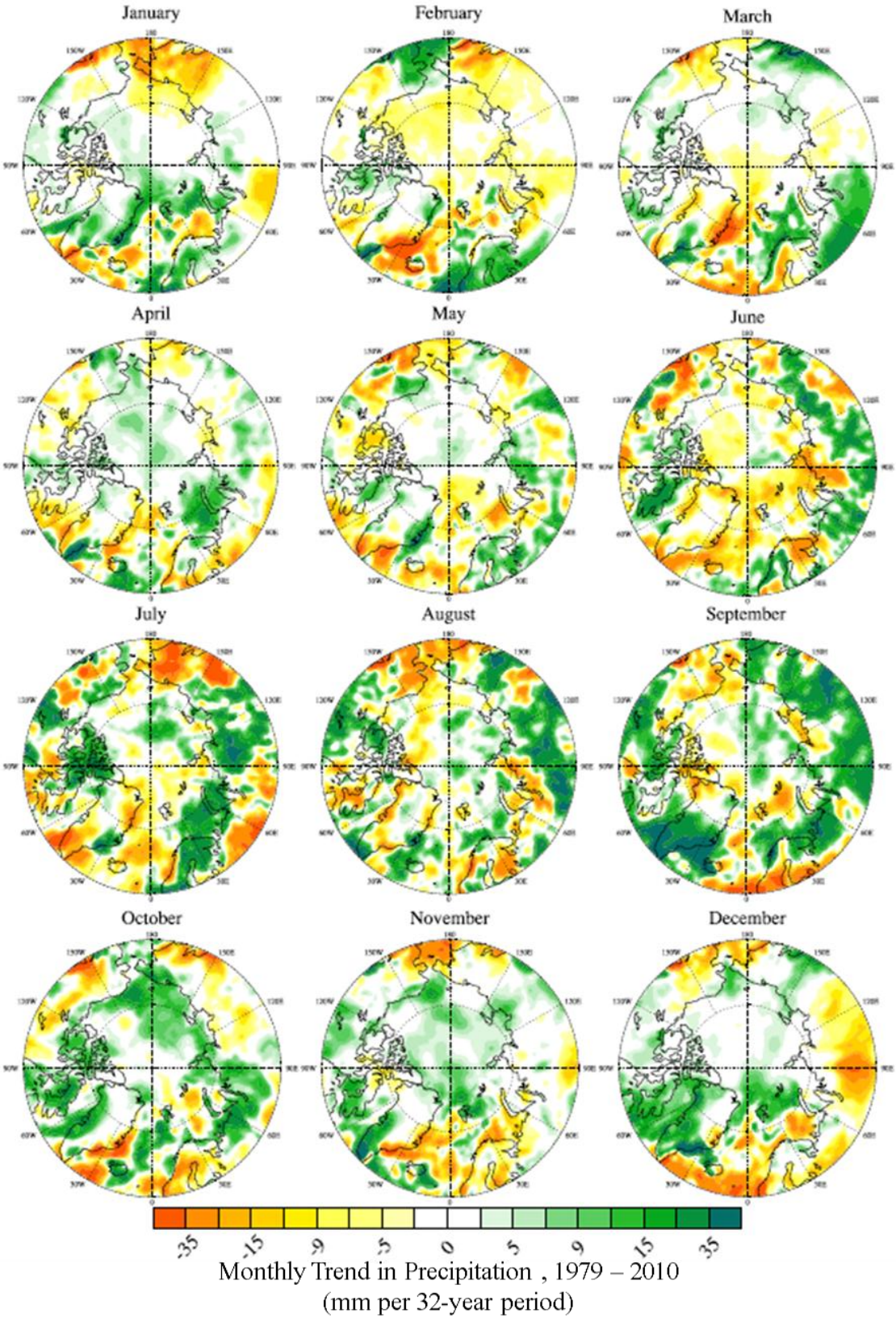


Figure 11. Plots of monthly precipitation trends for 1979 – 2010, as represented by ERA-Interim.

Winter (DJF)

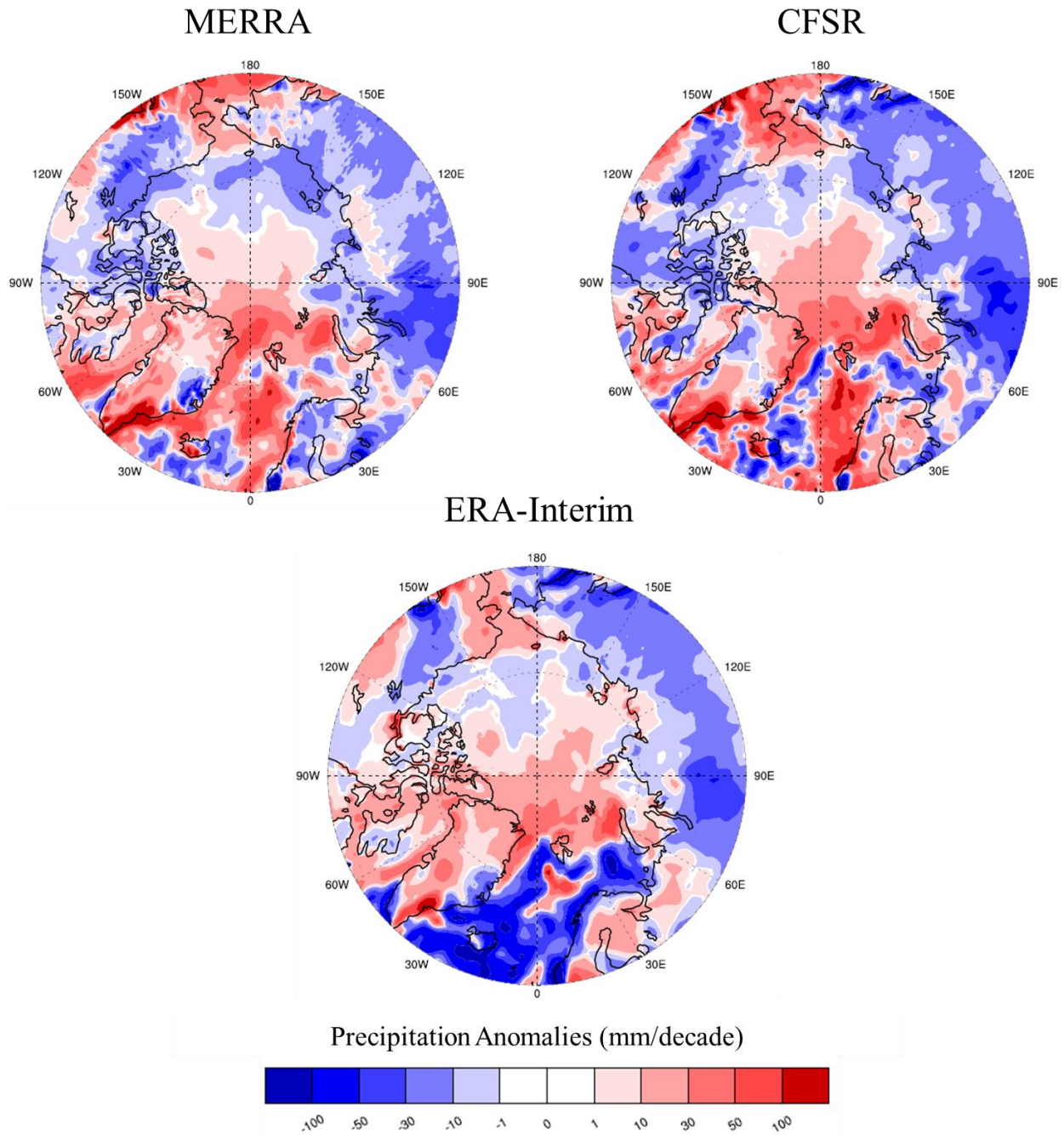


Figure 12. Plots of 10-year winter (DJF) precipitation anomalies, calculated as: (DJF 2001–2010) minus (1979–2010), as represented by MERRA, CFSR, and ERA-Interim. Blue colors represent negative anomalies; reds represent positive anomalies.

Spring (MAM)

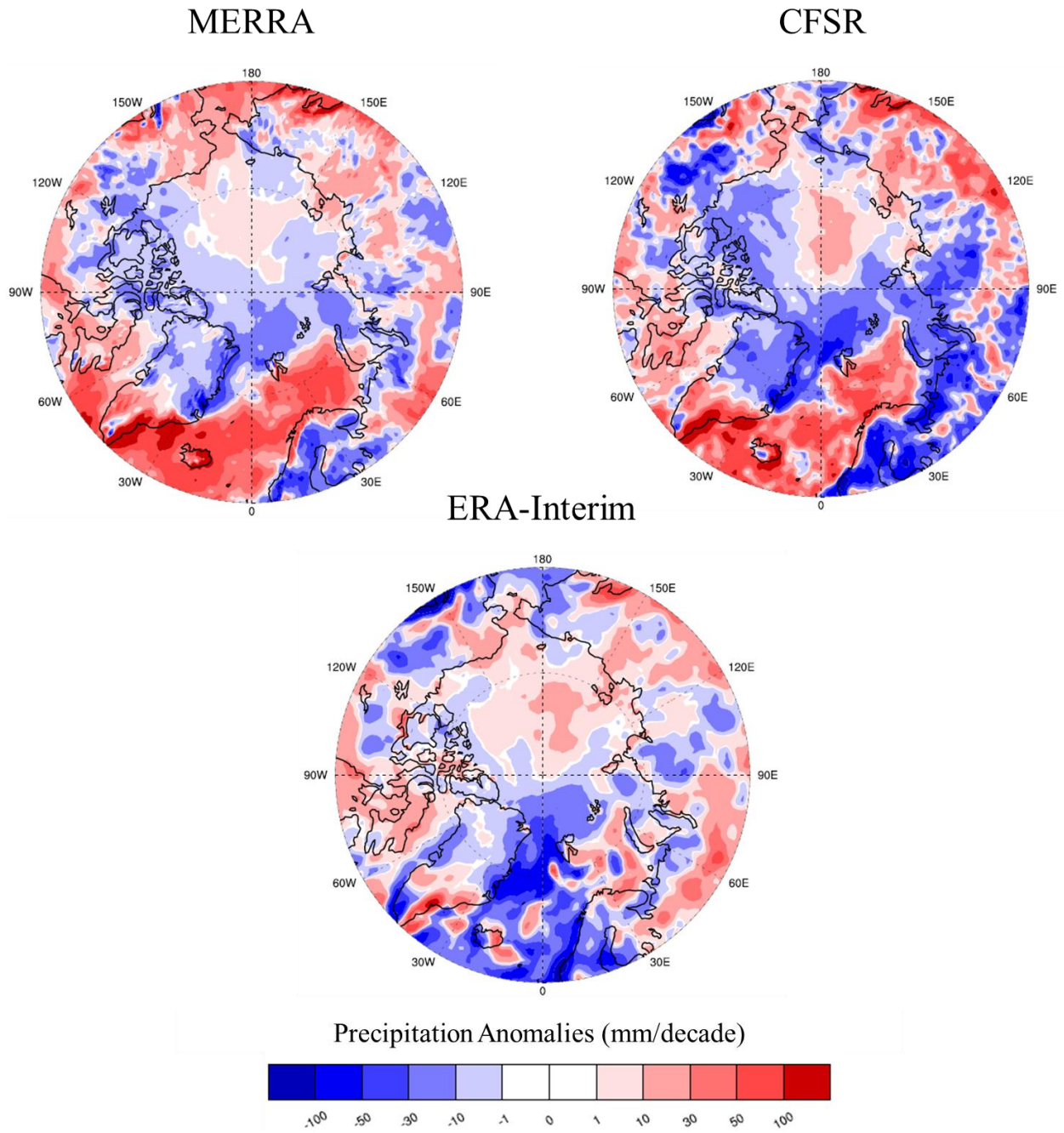


Figure 13. Plots of 10-year spring (MAM) precipitation anomalies; calculated as: (MAM 2001–2010) minus (1979–2010), as represented by MERRA, CFSR, and ERA-Interim. Blue colors represent negative anomalies; reds represent positive anomalies.

Summer (JJA)

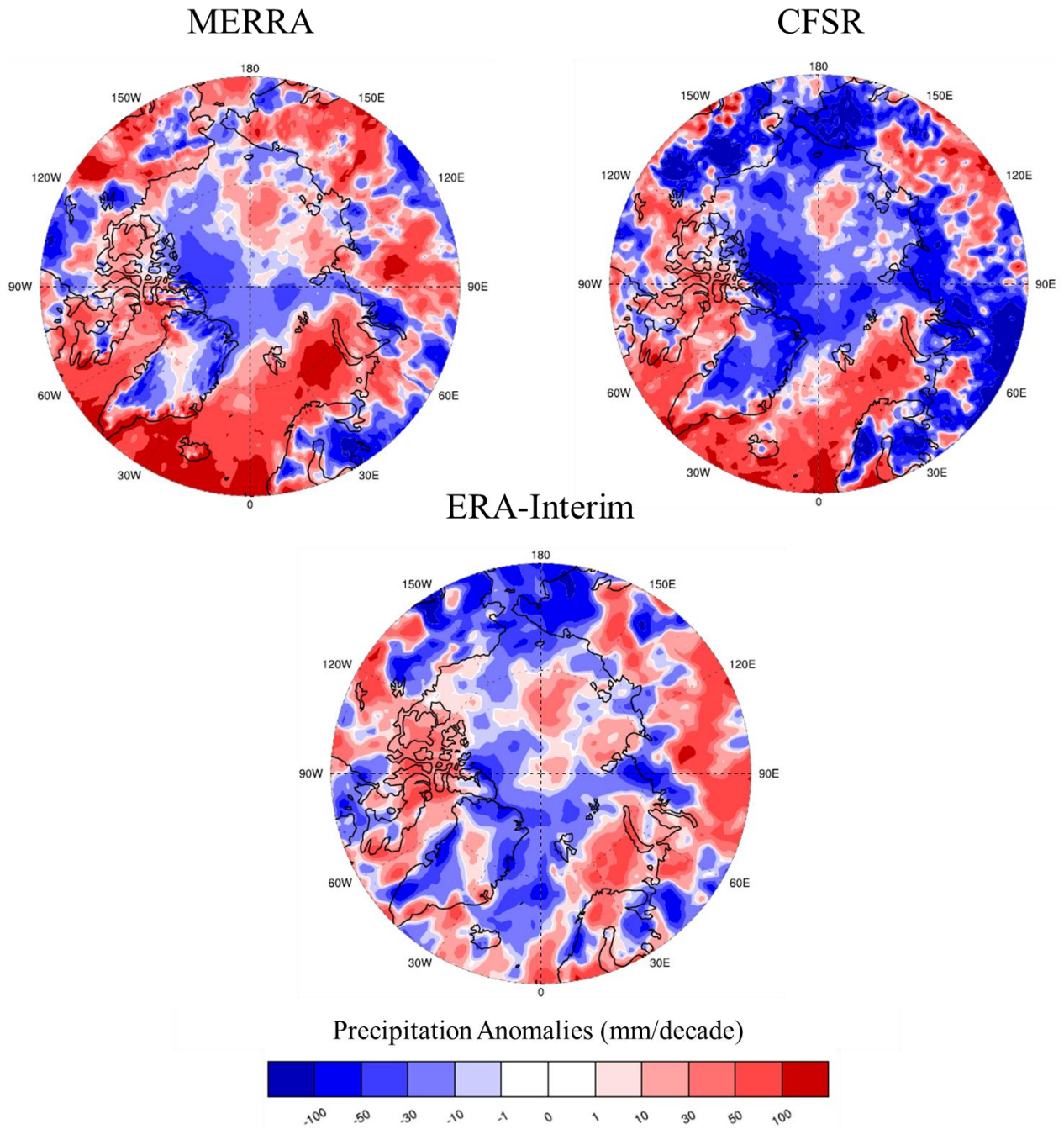
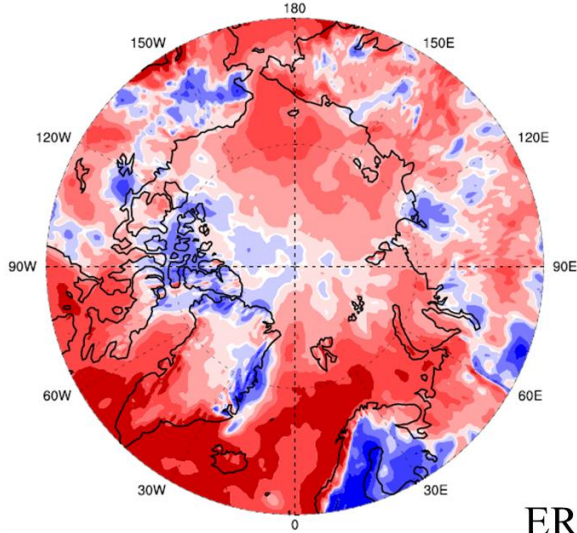


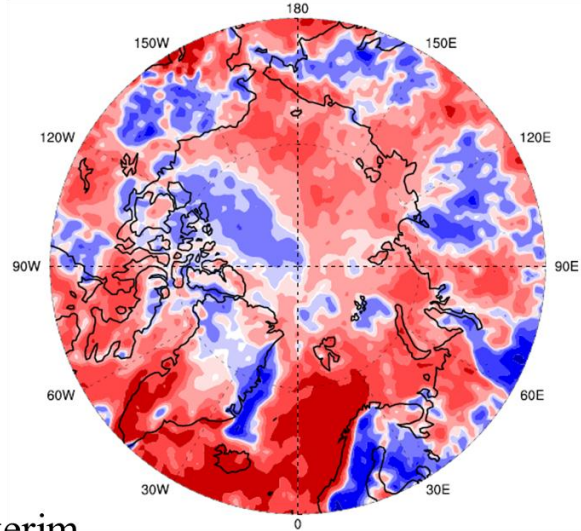
Figure 14. Plots of 10-year summer (JJA) precipitation anomalies, calculated as: (JJA 2001–2010) minus (1979–2010), as represented by MERRA, CFSR, and ERA-Interim. Blue colors represent negative anomalies; reds represent positive anomalies.

Autumn (SON)

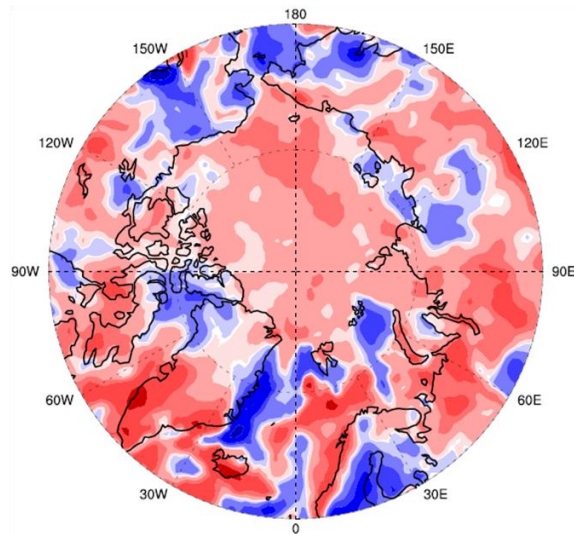
MERRA



CFSR



ERA-Interim



Precipitation Anomalies (mm/decade)



Figure 15. Plots of 10-year autumn (SON) precipitation anomalies, calculated as: (SON 2001–2010) minus (1979–2010), as represented by MERRA, CFSR, and ERA-Interim. Blue colors represent negative anomalies; reds represent positive anomalies.

3.2.2 Results

Strong positive trends are found across the Scandinavian countries during winter (+12 to +35 mm). Strong positive trends also characterize the Bering Sea and western Alaska (+12 to more than +35 mm), primarily due to increases at the end of the winter season with stronger trends located at lower latitudes nearest 60°N. Negative trends in precipitation are more of the rule over central Eurasia during the winter season. Moderate to large decreases in December and January precipitation are centered over western Russia (near 70°N, 90°E) as well as the region spanning far eastern Russia (from 150°E to the Chukchi Sea). Latitudes south of 70°N have experienced moderate to strong negative trends (-15 to < -35 mm) during the winter season.

The progression from spring to summer yields a mix of positive and negative trends across the entire Arctic, most noticeable over the continental regions. While “patchy,” the signs of the trends tend to be in agreement across all three of the reanalyses. Spring precipitation from all three reanalyses has positive trends (+5 to +12 mm) across the North Slope of Alaska and an area crossing the Canadian-Alaska border, spanning from about 150°W to 120°W and along ~64°N. Strong positive trends (approximately +15 mm, with locally greater increases in excess of +35 mm) exist across the windward side of the Ural Mountains, particularly in early spring (March). Other areas with positive trends include the northeastern Canadian Arctic, particularly in late spring (May) as well as the region spanning 30°E to 60°E.

During the summer season, trends point to drying in most continental locations but an increase in precipitation over Fram Strait into the Norwegian Sea. Other areas of notable negative summer trends include extreme eastern Russia and across the southern portions of the Bering Sea (along 60°N).

One point of interest is high variability in precipitation with respect to trends along the Greenland coastline during spring. This high variability is rather consistent across the three reanalyses, with the best agreement being between CFSR and ERA-Interim along the east-central coast of Greenland. In summer and there is good agreement across MERRA, CFSR, and ERA-interim. For instance, during the month of July, southern and northeastern Greenland sees a drying pattern, while an increase in precipitation is seen along the northwest and east-central coastal areas. In August these patterns appear to shift counter-clockwise around the Greenland ice sheet with positive trends in precipitation across the southern tip,

For autumn, results show strong positive trends (upwards of +15 mm) in precipitation over continental areas. Other locations with positive precipitation trends include southern and western Greenland (generally along the 50°W meridian). The area stretching eastward across the Beaufort Sea, off the coast of Alaska to Eurasia, also shows positive trends (+7 to +15 mm) in precipitation during this season. Moderate negative trends (-7 to -15 mm) are most prominent over the Canadian Arctic Archipelago into the western Arctic Ocean during early autumn (September).

Anomaly plots of the spring, summer, and autumn seasons show mostly positive anomalies over land areas, Southern Greenland, and the North Atlantic sector (**Figures 12 – 15**). Anomalies were calculated as: (Season 2001–2010) minus (1979–2010). Large positive anomalies across nearly all areas mark the autumn season as experiencing the greatest increase in precipitation of any season (**Figure 15**). However, show negative anomalies dominate during winter over much of Eurasia. Similar to the previously discussed trend plots, there is agreement across the reanalyses in the anomaly plots – with the exception of the North Atlantic sector.

Overall, patterns of long-term monthly trends are in agreement across the three reanalyses. The pattern of anomalies for the most recent decade supports these findings. However, there is one major discrepancy between models. The inconsistency lies with ERA-Interim across the North Atlantic, including Fram Strait and the Norwegian Sea. This difference becomes strikingly apparent when looking at winter precipitation anomaly plots (**Figures 12**).

3.3 The ERA-Interim Discrepancy

For all seasons, ERA-Interim outputs yield strong to moderate negative anomalies over the northern North Atlantic region, including the Greenland Sea, north into Fram Strait as well as the western Norway coastline extending into the Barents Sea; whereas both MERRA and CFSR show positive anomalies for this region (**Figures 12 – 15**). The positive anomalies in MERRA and CFSR over the North Atlantic are most pronounced in the autumn. The negative anomalies seen over the North Atlantic in ERA-Interim are most pronounced in winter, and then shift northward and weaken in spring and summer. The discrepancies are nearly non-existent in autumn; although, ERA-Interim does not show the same magnitude of positive anomalies seen across southern Greenland and Fram Strait in MERRA and ERA-Interim.

3.3.1 General Circulation Analysis

The first step in addressing the underlying cause of the discrepancy seen in ERA-Interim's total precipitation field (most noticeable in the anomaly plots in **Figures 12 – 15**) was to investigate related fields within the reanalyses in an effort to find evidence that the discrepancy may be related to differences between the atmospheric circulation models. The NOAA Earth System Research Lab's "Web-based Reanalysis Intercomparison Tool" was used to make comparison plots for various variables; the webpage can be accessed here: <http://www.esrl.noaa.gov/psd/cgi-bin/data/testdap/plot.comp.pl>. Since the discrepancy in

anomalous precipitation is most prevalent in the winter (DJF), wintertime plots are shown. Winter sea level pressure (SLP) (**Figure 16**) and 500 mb geopotential height anomalies (**Figure 17**) were plotted. The anomalies were calculated as: (December to February 2001–2010) minus (1979–2010).

It seemed possible that anomalously high atmospheric pressure was resulting in the strong negative precipitation anomalies seen in ERA-Interim that were not corroborated by MERRA nor CFSR. However, the wintertime SLP and 500mb geopotential height fields did not indicate any cross-reanalysis differences that would explain the disparity between the reanalysis precipitation fields.

Plots of precipitable water anomaly fields for the past decade were also plotted (**Figure 18**). MERRA data was unavailable so only CFSR and ERA-Interim were compared. While there are notable differences across lower latitudes (below 60°N), the region north of 60°N as including the North Atlantic region of interest are in agreement. It appears unlikely that ERA-Interim's total precipitation fields stem from an issue with available precipitable water.

Winter (DJF)

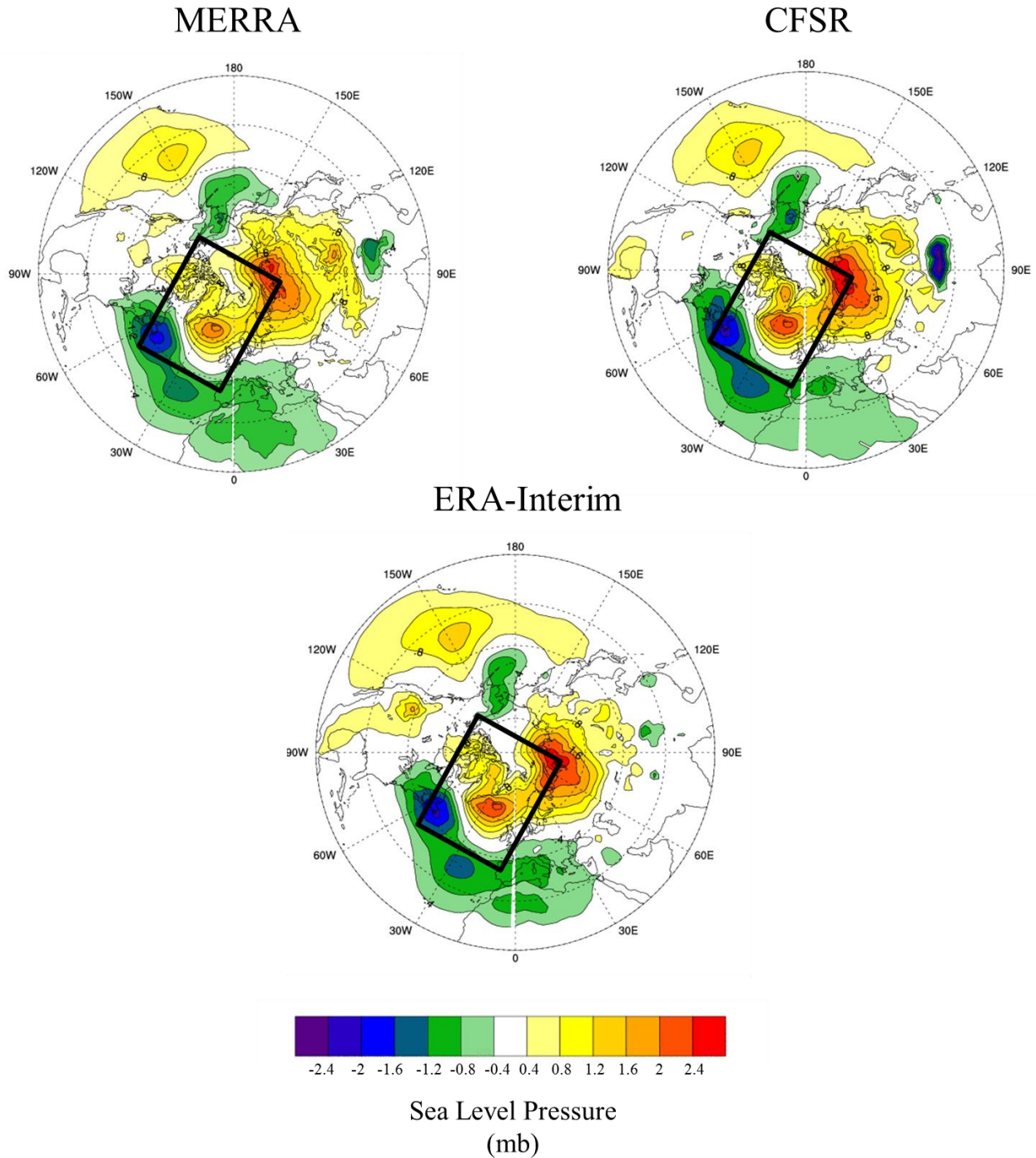
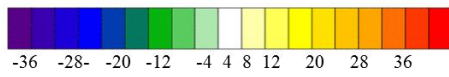
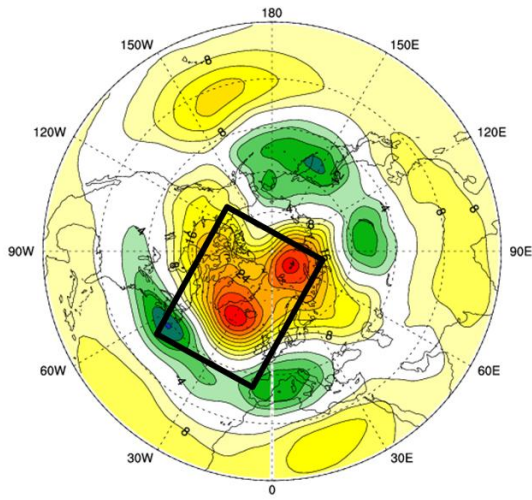


Figure 16. Wintertime sea level pressure (SLP) anomaly fields for the last decade. Anomalies were calculated as: (DJF 2001–2010) minus (1979–2010). Black boxes highlight the North Atlantic region of interest.

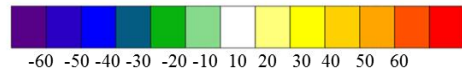
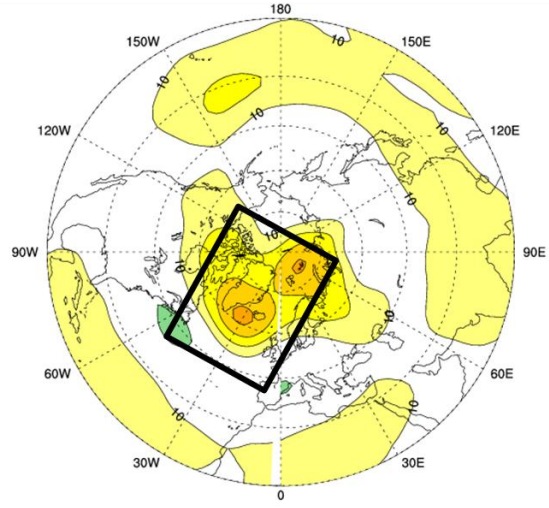
Winter (DJF)

MERRA



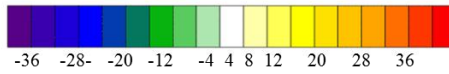
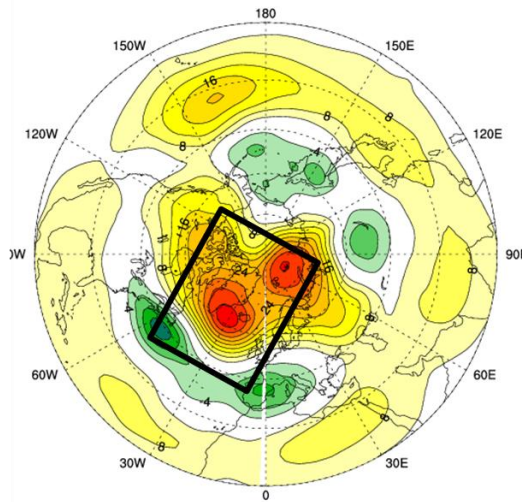
500 mb Geopotential Height
(gpm)

CFSR



500 mb Geopotential Height
(gpm)

ERA-Interim



500 mb Geopotential Height
(gpm)

Figure 17. Wintertime 500 mb geopotential height anomaly fields for the last decade. Anomalies were calculated as: (DJF 2001–2010) minus (1979–2010). Black boxes highlight the North Atlantic region of interest.

Winter (DJF)

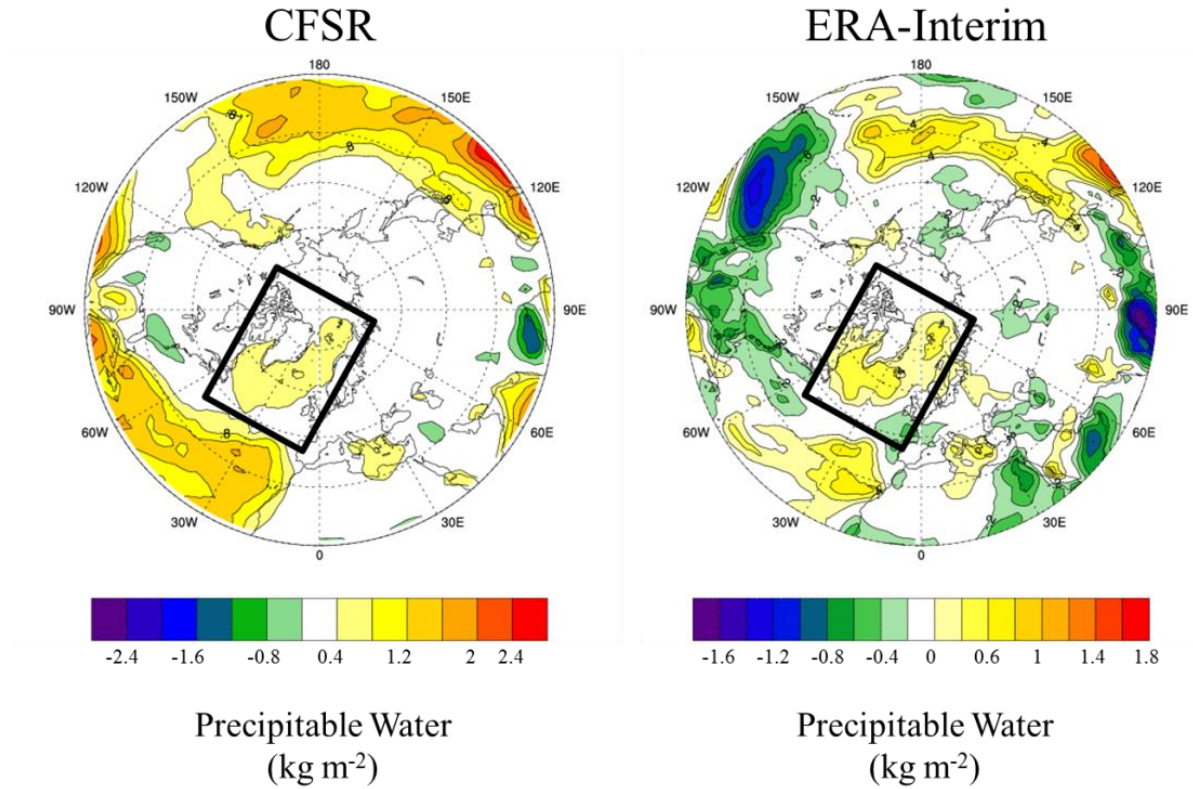


Figure 18. Wintertime precipitable water (kg m^{-2}) anomaly fields. Anomalies were calculated as: (DJF 2001–2010) minus (1981–2010). Blues and purples indicate negative anomalies; oranges and reds indicate positive anomalies. Black box highlights the North Atlantic region of interest.

Given these findings, it appears that the difference is not a result of some difference within the atmospheric circulation model. Rather, the discrepancy within the precipitation field likely stems from the way in which ERA-Interim is generating precipitation. Precipitation and convective processes are notoriously difficult to accurately simulate. The work needed to address exactly *why* or *how* the models are different is outside the scope of this thesis; in fact, improving the modeling of cloud phases, cloud water content, and precipitation has always been – and will continue to be – an ongoing process for the atmospheric modeling community.

3.3.2 Coastal Station Analysis

Unable to pinpoint why ERA-Interim’s precipitation field is vastly different across the North Atlantic sector compared to CFSR and MERRA’s; the focus was next placed upon determining which reanalysis shows the strongest agreement with nearby stations. The GHCN dataset used in this study lacks buoy data; therefore, coastal station data nearest the northern North Atlantic waters were investigated. Attention was placed on 41 North Atlantic coastal stations (**Table 3**).

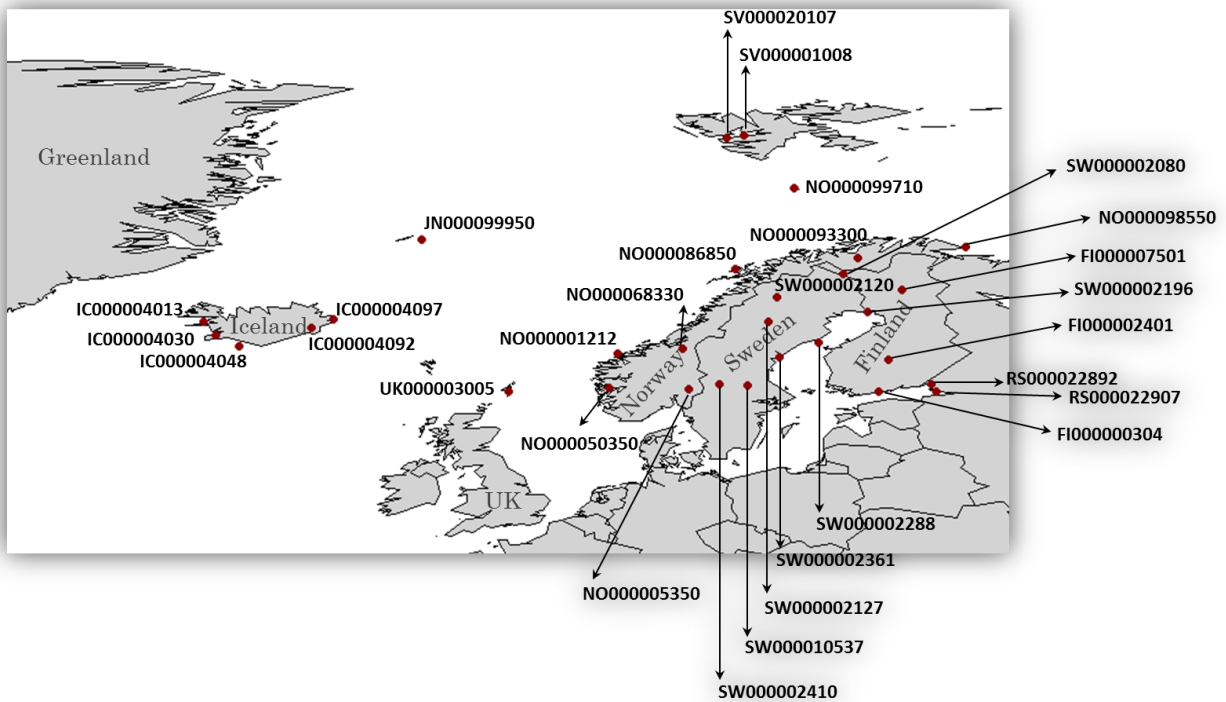
The stations needed to have at least 4-years of consecutive monthly data to be retained for the time series analysis; the ‘Kendall’ package in R has a documented bug with datasets with $n < 4$. For those stations that do have missing data, the missing months within these timespans are sporadic and the longest consecutive period of missing data is only four months total. Of the 31 stations retained for analysis, the majority had complete or nearly-complete monthly data for the 21 year time period, spanning January 1979 through December 1999; only one station (SV000020107) had less data, with a dataset spanning 6 years (January 1979 to December 1984) (**Table 3**).

Table 3. Location and time span details for the 41 North Atlantic coastal GHCN stations.

Station ID	Location (City)	Latitude (°N)	Longitude (°E)	Timespan of Consecutive Data (≥ 4-year period of consecutive monthly data)				
				Start Date (Mon-YY)	End Date (Mon-YY)	Total # of Months	Missing Months	Missing Months
FI00000304	HELSINKI	60.17	24.95	Jan-79	Dec-01	276	0	0
FI000002401	JYVASKYLA	62.4	25.683	Jan-79	Dec-01	276	0	0
FI000002963	JOKIOINEN	60.817	23.5	< 4 years				
FI000007501	SODANKYLA	67.367	26.65	Jan-79	Dec-01	276	0	0
GL000004250	NUUK	64.167	308.25	< 4 years				
GL000004320	DANMARKSHAVN	76.767	341.333	< 4 years				
GL000004360	TASILAQ	65.6	322.367	< 4 years				
IC000004013	STYKKISHOLMUR	65.083	337.267	Jan-79	Jul-99	247	0	0
IC000004030	REYKJAVIK	64.132	338.1	Jan-79	Aug-99	248	0	0
IC000004048	VESTMANNAEYJAR	63.4	339.717	Jan-79	Jun-99	246	0	0
IC000004063	AKUREYRI	65.683	341.917	< 4 years				
IC000004092	TEIGARHORN	64.68	344.86	Jan-79	Jun-99	247	3	3
IC000004097	DALATANGI	65.266	346.417	Jan-79	May-99	245	0	0
ICW00016201	KEFLAVIK	63.9667	337.4	< 4 years				
JN000099950	JAN-MAYEN	70.93	352.67	Jan-79	Dec-03	300	3	3
NO000001026	TROMSO	69.65	18.933	< 4 years				
NO000001212	ONA	62.867	6.533	Jan-79	Sep-01	273	4	4
NO000001238	FOKSTUA	62.117	9.283	< 4 years				
NO000005350	NORD-ODAL	60.38	11.55	Jan-79	Dec-99	252	0	0
NO000050350	SAMNANGER	60.46	5.9	Jan-79	Dec-99	252	0	0
NO000050540	BERGEN/FLORIDA	60.383	5.333	< 4 years				
NO000050550	BERGEN-FREDRIKSBERG	60.4	5.317	< 4 years				
NO000068330	SELBU-STUBBE	63.2	11.117	Jan-79	Dec-99	252	0	0
NO000086850	BARKESTAD	68.82	14.8	Jan-79	Dec-99	252	0	0
NO000093300	SUOLOVUOPMI	69.583	23.533	Jan-79	Dec-99	252	5	5
NO000097250	KARASJOK	69.467	25.517	< 4 years				
NO000098550	VARDO	70.367	31.1	Jan-79	Nov-03	299	0	0
NO000099710	BJORNOYA	74.517	19.017	Jan-79	Dec-99	252	0	0
RS000022892	VYBORG	60.717	28.733	Jan-79	Jun-96	210	0	0
RS000022907	OZERKI	60.2	29	Jan-79	Oct-94	190	0	0
SV000001008	SVALBARD	78.25	15.467	Jan-79	Feb-04	302	2	2
SV000020107	BARENCEBURG	78.067	14.25	Jan-79	Dec-84	72	0	0
SW000002080	KARESUANDO	68.45	22.45	Jan-79	Dec-99	252	0	0
SW000002120	KVIKKJOKK-ARRENJARK	66.883	17.75	Jan-79	Dec-03	300	4	4
SW000002127	STENSELE	65.067	17.167	Jan-79	Dec-99	252	0	0
SW000002196	HAPARANDA	65.833	24.15	Jan-79	Dec-03	300	0	0
SW000002288	HOLMOGADD	63.6	20.75	Jan-79	Feb-03	290	0	0
SW000002361	HARNOSAND	62.633	17.95	Jan-79	Dec-99	252	0	0
SW000002410	MALUNG	60.683	13.717	Jan-79	Dec-03	300	0	0
SW000010537	FALUN	60.617	15.667	Jan-79	Dec-01	276	0	0
UK000003005	LERWICK	60.133	358.817	Jan-79	Dec-01	276	1	1

A location map of the thirty stations that were retained for analysis is found in **Figure 19**. For ease of reference, the two letter prefix of the station IDs indicate the country or island (i.e. FI, Finland; IC, Iceland; JN, Jan-Mayan Island; NO, Norway; RS, Russia, SV, Svalbard, SW, Sweden; UK, United Kingdom). All stations are located north of 60°N and bounded by 51.7°W and 31.1°E longitude.

Figure 19. Location map of the 30 northern north Atlantic stations retained for comparison with the reanalysis fields in an attempt to address the ERA-Interim discrepancy.



The Seasonal Mann-Kendall trend test (Hirsch, et al., 1982) was chosen because it compensates for the presence of a seasonal cycle. This seasonal Mann-Kendall trend test is a variant of the Mann-Kendall trend test, which is a special case of the Kendall rank correlation test (Kendall, 1975). The Mann-Kendall trend test is used to determine whether a variable (precipitation measurements) tends to increase or decrease with a monotonic change in time. Other benefits of using this Seasonal Mann-Kendall trend test include that it is a nonparametric test – useful here since we cannot assume normality in the precipitation datasets – and uses rank-correlation coefficients to calculate a trend test statistic (τ), allowing it to handle datasets with missing values.

In using the Seasonal Mann-Kendall trend method, the data series is first divided into subsets, with each subset representing the measurements collected during a common sampling event; in this study, sampling frequency was monthly and therefore 12 subsets (i.e. one subset for each month of the year) were used. Next, the standard Mann-Kendall test is then performed separately on each month subset; a test statistic (monthly τ) is calculated for each month-subset. Finally, the overall test statistic (overall τ) is calculated from a standard Mann Kendall test for the entire period of available monthly data.

The Mann-Kendall tests were performed on the thirty North Atlantic stations retained for analysis. The functions, `MannKendall(x)` and `SeasonalMannKendall(x)`, are found within the ‘Kendall’ package in R. Details regarding this package and function can be found here: <http://cran.r-project.org/web/packages/Kendall/Kendall.pdf>. The results, including the monthly and overall τ values and the associated p -values for the seasonal (monthly) and standard Mann-Kendall tests appear in **Table 4**.

Table 4. Mann-Kendall trend test results for 30 coastal GHCN stations. Monthly and overall tau values and associated *p*-values are listed; statistically significant values (*p*-value < 0.05) are indicated by shaded cells with bold text. Red text indicates negative tau values.

Station ID		Winter			Spring			Summer			Autumn			Overall tau
		Dec	Jan	Feb	Mar	Apr	May	Jun	Jul	Aug	Sep	Oct	Nov	
FI00000304	tau	-0.202	0.004	0.344	-0.130	0.209	-0.099	0.012	-0.051	-0.032	-0.265	0.083	-0.170	-0.015
	p-value	0.178	0.979	0.022	0.383	0.162	0.509	0.937	0.731	0.833	0.077	0.579	0.256	0.713
FI000002401	tau	-0.174	0.012	0.289	0.162	0.115	-0.063	-0.051	-0.166	-0.273	-0.099	0.091	-0.225	-0.010
	p-value	0.245	0.937	0.054	0.279	0.444	0.673	0.731	0.267	0.068	0.509	0.544	0.132	0.800
FI000007501	tau	-0.190	-0.004	0.202	-0.020	0.146	-0.198	-0.083	0.087	-0.233	-0.246	-0.067	-0.091	-0.038
	p-value	0.205	0.979	0.178	0.895	0.328	0.187	0.579	0.561	0.004	0.101	0.653	0.544	0.350
IC000004013	tau	0.032	0.086	-0.095	0.024	-0.314	0.224	-0.200	-0.124	0.221	-0.069	-0.032	0.048	-0.013
	p-value	0.846	0.587	0.546	0.880	0.046	0.156	0.205	0.432	0.173	0.673	0.846	0.770	0.769
IC000004030	tau	0.232	0.000	0.024	0.019	-0.305	0.267	-0.190	0.067	0.086	0.042	-0.185	0.137	0.080
	p-value	0.153	1.000	0.880	0.904	0.053	0.091	0.227	0.672	0.587	0.795	0.256	0.399	0.851
IC000004048	tau	0.105	-0.171	-0.143	-0.095	-0.448	0.038	0.010	-0.053	0.063	0.021	-0.200	-0.032	-0.070
	p-value	0.516	0.277	0.365	0.546	0.005	0.809	0.952	0.746	0.697	0.897	0.218	0.846	0.104
IC000004092	tau	0.216	0.211	-0.105	-0.067	0.057	0.029	0.291	0.143	0.253	-0.137	-0.084	0.316	0.068
	p-value	0.196	0.194	0.516	0.672	0.717	0.856	0.065	0.365	0.119	0.399	0.604	0.052	0.113
IC000004097	tau	0.189	0.248	-0.086	0.010	0.324	-0.171	0.179	0.253	0.000	-0.179	0.000	0.195	0.059
	p-value	0.243	0.116	0.587	0.952	0.040	0.277	0.270	0.119	1.000	0.270	1.000	0.230	0.167
JN000099950	tau	0.012	-0.167	-0.003	-0.057	-0.175	0.024	-0.030	-0.390	0.204	0.011	-0.058	-0.143	-0.051
	p-value	0.937	0.243	0.981	0.691	0.224	0.870	0.833	0.008	0.165	0.941	0.691	0.342	0.195
NO000001212	tau	-0.074	0.169	0.333	0.238	0.020	0.055	0.273	0.158	-0.099	-0.388	0.017	-0.281	0.025
	p-value	0.631	0.271	0.030	0.121	0.895	0.711	0.076	0.291	0.509	0.010	0.910	0.067	0.549
NO000005350	tau	0.114	0.220	0.124	-0.190	0.086	-0.114	0.086	-0.086	0.029	0.086	-0.152	-0.171	0.009
	p-value	0.469	0.164	0.432	0.227	0.587	0.469	0.587	0.587	0.856	0.587	0.334	0.277	0.835
NO000050350	tau	0.000	0.133	0.352	0.143	0.190	-0.024	0.095	0.305	-0.295	-0.371	-0.038	-0.295	0.025
	p-value	1.000	0.398	0.025	0.365	0.227	0.880	0.546	0.053	0.061	0.019	0.809	0.061	0.557
NO000068330	tau	0.086	0.038	0.257	0.152	-0.010	0.086	0.305	0.119	-0.038	-0.200	0.200	-0.162	0.059
	p-value	0.587	0.809	0.103	0.334	0.952	0.587	0.053	0.450	0.809	0.205	0.205	0.305	0.161
NO000086850	tau	-0.048	0.067	0.024	0.314	-0.029	0.143	-0.010	-0.048	0.219	0.105	0.219	0.124	0.072
	p-value	0.763	0.672	0.880	0.046	0.856	0.365	0.952	0.763	0.165	0.506	0.165	0.432	0.090
NO000093300	tau	0.267	0.116	0.253	0.362	0.210	-0.143	-0.038	-0.053	0.124	-0.076	0.181	0.124	0.094
	p-value	0.091	0.475	0.119	0.022	0.184	0.365	0.809	0.746	0.432	0.629	0.278	0.432	0.028
NO000098550	tau	-0.011	-0.147	0.127	0.154	0.024	-0.027	-0.070	0.007	0.087	-0.221	-0.040	-0.087	-0.020
	p-value	0.941	0.304	0.375	0.282	0.870	0.852	0.624	0.963	0.544	0.123	0.779	0.543	0.603
NO000099710	tau	0.355	0.491	0.281	0.411	0.073	0.213	0.153	0.033	0.300	0.244	0.280	0.347	0.228
	p-value	0.015	0.001	0.050	0.004	0.607	0.135	0.283	0.815	0.036	0.088	0.050	0.015	3.9 E09
RS000022892	tau	-0.412	-0.059	0.255	0.281	0.085	-0.020	-0.281	-0.309	-0.088	-0.074	0.000	-0.294	-0.056
	p-value	0.021	0.733	0.140	0.103	0.622	0.910	0.103	0.084	0.621	0.680	1.000	0.099	0.231
RS000022907	tau	-0.314	0.133	0.150	0.000	0.150	-0.343	-0.300	-0.267	-0.067	-0.167	-0.033	-0.429	-0.063
	p-value	0.102	0.471	0.418	1.000	0.418	0.065	0.105	0.150	0.719	0.368	0.857	0.026	0.197
SV000001008	tau	0.249	-0.103	-0.329	-0.168	-0.207	-0.175	-0.244	0.175	-0.037	0.144	-0.102	0.183	-0.047
	p-value	0.091	0.466	0.022	0.242	0.153	0.237	0.095	0.224	0.797	0.315	0.482	0.206	0.232
SV000020107	tau	0.600	0.200	0.600	0.467	0.200	0.067	-0.200	-0.333	0.467	-0.067	-0.200	0.200	0.061
	p-value	0.091	0.573	0.091	0.188	0.573	0.851	0.573	0.348	0.188	0.851	0.573	0.573	0.454

Table 4. Continued.

Station ID		Winter			Spring			Summer			Autumn			Overall tau
		Dec	Jan	Feb	Mar	Apr	May	Jun	Jul	Aug	Sep	Oct	Nov	
SW000002080	tau	0.039	0.165	0.398	0.086	0.206	-0.197	0.133	-0.129	0.158	-0.196	-0.058	0.015	0.058
	p-value	0.809	0.302	0.013	0.586	0.194	0.215	0.398	0.415	0.319	0.215	0.717	0.928	0.172
SW000002120	tau	-0.034	0.114	0.234	-0.244	0.302	-0.051	0.120	0.013	-0.113	-0.268	-0.235	-0.184	-0.021
	p-value	0.815	0.426	0.112	0.096	0.039	0.728	0.400	0.926	0.427	0.062	0.102	0.199	0.591
SW000002127	tau	-0.208	0.091	0.192	-0.227	0.247	-0.220	0.172	0.138	-0.014	-0.203	-0.155	-0.258	-0.021
	p-value	0.193	0.565	0.226	0.155	0.122	0.164	0.277	0.381	0.928	0.203	0.333	0.103	0.618
SW000002196	tau	-0.094	0.181	0.194	-0.074	0.149	0.064	0.084	0.154	-0.201	-0.115	-0.147	-0.027	0.020
	p-value	0.513	0.207	0.175	0.606	0.303	0.657	0.559	0.282	0.161	0.426	0.304	0.852	0.601
SW000002288	tau	-0.138	0.090	0.181	0.077	0.135	0.069	0.113	0.185	-0.207	-0.189	-0.098	0.040	0.023
	p-value	0.346	0.528	0.207	0.602	0.358	0.637	0.442	0.206	0.157	0.197	0.503	0.785	0.555
SW000002361	tau	-0.039	0.114	0.158	-0.172	0.167	-0.077	0.100	0.115	-0.221	-0.243	-0.067	-0.105	-0.008
	p-value	0.808	0.469	0.318	0.277	0.290	0.629	0.526	0.468	0.164	0.123	0.672	0.506	0.848
SW000002410	tau	-0.013	0.164	0.141	-0.218	0.138	-0.024	0.064	0.190	-0.080	-0.131	-0.013	-0.084	0.023
	p-value	0.925	0.252	0.326	0.129	0.338	0.870	0.657	0.183	0.575	0.362	0.926	0.559	0.557
SW000010537	tau	-0.004	-0.091	0.150	-0.209	0.004	-0.036	-0.059	0.130	-0.277	-0.265	0.170	-0.170	-0.030
	p-value	0.979	0.544	0.315	0.162	0.979	0.812	0.692	0.383	0.064	0.077	0.256	0.256	0.459
UK000003005	tau	0.087	-0.016	0.403	-0.020	0.119	-0.163	0.092	-0.004	-0.088	-0.246	-0.044	-0.087	0.010
	p-value	0.561	0.916	0.009	0.895	0.428	0.278	0.543	0.979	0.561	0.101	0.771	0.561	0.810

The results of the trend test showed a near-equal mix of positive and negative monthly trends, with the positive to negative tally coming to 187 and 173, respectively (**Table 4**). Of the 360 monthly tau values calculated, only 24 were statistically significant at the 95% level (p -value < 0.05). The majority of stations have data spanning 21 years (January 1979 to December 1999); only one station (SV000020107) had less data, with a dataset spanning 6 years (January 1979 to December 1984) (**Table 3**).

Interestingly, seven stations had statistically significant trends for the month of February across all years in the datasets; with six Scandinavian stations (FI000000304, NO000001212, NO000050350, NO000099710, SW000002080, UK000003005) showing significant positive trends and one Svalbard station (SV000001008) showing a significant negative trend (**Table 4**).

Each of these stations had data for the month of February for at least 20 years. MERRA, CFSR, and ERA-Interim appear to show a similar pattern. In all three reanalyses, positive trends are seen across the Norwegian coastal areas for the month of February over the 32-year analysis period extending from January 1979 to December 2010 (**February, Figures 9–11**). Negative trends are also seen over Svalbard in the reanalysis output; though these negative trends are most prevalent in MERRA and ERA-Interim (**February, Figures 9–11**).

Three stations along the Norwegian coast (NO000086850, NO000093300, NO000099710) had statistically significant positive trends for the month of March. All three reanalyses show agreement with this pattern of positive trends (**March, Figures 9–11**). Three Icelandic stations had statistically significant positive (IC000004097) and negative trends (IC000004013, IC000004048) for April. Again, these findings are also in agreement with the reanalysis output, with all three reanalyses showing negative trends across western Iceland and positive trends dominating the eastern half of the country (**April, Figures 9–11**).

Only two stations had statistically significant trends for the overall time series (**Table 4**). The Bjørnøya, Norway Station (NO000099710) had seven months with statistically significant positive trends, as well as a statistically significant overall trend for the station's 21 year analysis period (overall tau = 0.228, p -value < 0.05). The only other station with a significant overall trend was Suolovuopmi, Norway (NO000093300) (overall tau = 0.094, p -value < 0.05).

While the majority of monthly trends were not statistically significant, the distribution of positive and negative monthly trends is worth comparing with the reanalysis output. An examination of **Table 4** reveals that many Swedish stations (SW000002120, SW000002127, SW000002196, SW000002288, SW000002361, SW000002410, SW000010537) and the single station located on the Shetland Islands (Lerwick; UK000003005) show negative precipitation

trends persisting from August through December. This pattern is generally supported by all three reanalyses (**Figures 9–11**). The pattern is more ambiguous when it comes to the Norwegian coastal stations; which exhibit a more mixed pattern, with the northern coast of Norway seeing primarily positive precipitation trends for August, September and October; and many of the stations along the western coast of Norway seeing negative precipitation trends for August and September. Both the station data and the reanalysis data show a mix of trends for the Norway coastline from October through December; with the majority of stations showing a positive trend dominating in the later half of the winter season (January and February). All three reanalyses generally show this positive precipitation trend dominating across Norway, and Scandinavia as a whole, through the months of January and February (**Figures 9–11**). Ultimately, the trend analysis using the North Atlantic coastal stations show patterns that align well with the reanalysis output.

With general agreement between the North Atlantic stations and the reanalysis fields for the autumn and winter months it appears that wintertime ERA-Interim's discrepancy might be due to a difference in its data interpolation scheme. After this comparison with station data it appears that the trends across the Scandinavian Peninsula are exaggerated and extended farther out over the ocean compared to MERRA and CFSR. This is a reasonable possibility as MERRA and CFSR both use similar 3D-Var assimilation system (as discussed in Chapter 2). ERA-Interim uses a 1D+4D-Var rain assimilation system. This could partially be the result of a lack of buoy information available across this stretch of ocean with which to correct the model.

Dee et al. (2011) addressed the fact that in the early version of ERA-Interim the operator associated with the moist physics systematically overestimated rainfall by a factor of approximately two (Dee, et al., 2011). In the current version of ERA-Interim, this overestimation

of rainfall has been addressed through observational corrections. This has resulted in a drying-out of the model, which was subsequently addressed in bias corrections (Geer, et al., 2008). Even with bias corrections, the tendency for ERA-Interim to show drier conditions persists. Dee et al. (2011) admits that: “the fundamental limitation on our ability to describe the evolution of the atmosphere with increasing accuracy lies in the quality and availability of observations.” This could not be truer for the Arctic. This analysis is a great illustration of the need for increased observations across the Arctic. Perhaps this drying-out is the reason ERA-Interim shows strong negative anomalies across the northern North Atlantic, whereas MERRA and CFSR show strong positive anomalies.

CHAPTER 4

VALIDATION

4.1 Comparison with Observations

Monthly station observations from the most recent version of the GHCN (Lawrimore, et al., 2011) were used to validate the reanalysis output north of 60°N. The GHCN datasets were collectively created by the National Climatic Data Center (NCDC), the National Environmental Satellite, Data, and Information Service, the National Oceanic and Atmospheric Administration (NOAA), and the U.S. Department of Commerce. The GHCN monthly data can be accessed via the NOAA/NCDC website. Of the original 1023 individual stations north of 60°N, only 775 stations had data post-1979. **Figure 20** is a map showing the 775 stations retained for analysis. For a listing of the station IDs and their locations please refer to the table in **Appendix A**.

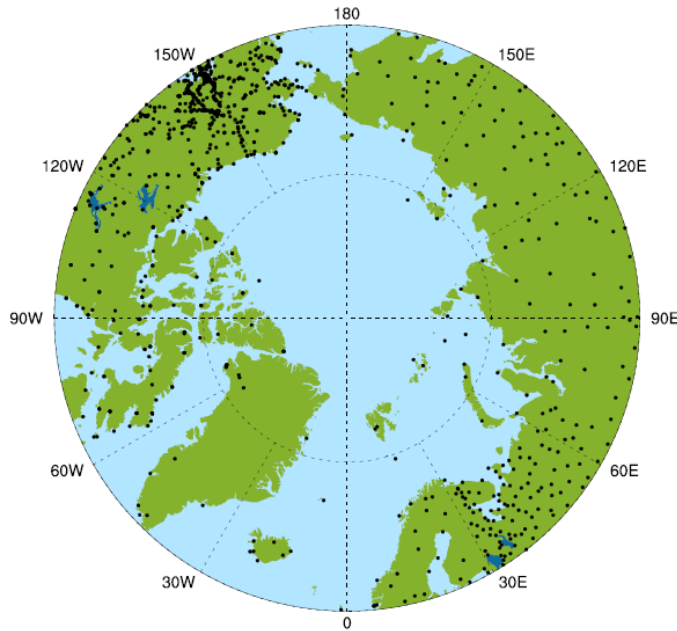


Figure 20. Map showing locations for 775 stations initially retained for analysis. Monthly station observations from the Global Historical Climatology Network (GHCN) were used for comparison with the reanalysis data.

4.1.1 Methods

Reanalysis data from the nearest grid node to each station were stored in three separate files, one for MERRA, CFSR, and ERA-Interim. Monthly GHCN observations from 1023 stations were acquired and after the initial round of quality control, stations that did not have data for 1979-onward were eliminated, 775 stations remained. A distance search was used to find the nearest reanalysis grid node to each station location. This was implemented using a pre-written function (`ind_nearest_coord`) in NCAR Command Language (NCL), which determines the indices of locations closest to a coordinate array. In this case, the function accepts GHCN point

location values and reanalysis coordinates, both of which must be 1D monotonic array (ie. latitudes or longitudes). The indices for the closest grid node to any particular GHCN station are then returned. The function is located in the contributed.ncl library. Data from these 775 stations were then allocated to individual station files. These files were then processed in batches, running statistical analysis for three-month seasons. The three month seasons were defined as follows: Dec-Jan-Feb (DJF), Mar-Apr-May (MAM), Jun-Jul-Aug (JJA), Sep-Oct-Nov (SON).

After the data at the corresponding grid nodes had been extracted, the reanalysis data at each location were then compared with the station observations, using methods similar to those from relevant studies (Yu, et al., 2010; Serreze, et al., 1998). Correlation, bias, and root-mean-square error (RMSE) were calculated using R statistical software. It is common to use such statistical measures for evaluating model accuracy; these methods, as well as support for their use, are discussed in the paragraphs below.

To determine the correlation between the reanalysis and station data sets, Spearman's rank order correlation coefficients were calculated. Spearman's rank order correlation, designated by ρ , is the nonparametric variation of the Pearson's r correlation. Equation 3 shows that this Spearman's rank can be written mathematically as:

$$\rho = 1 - \frac{6 \sum d^2}{n(n^2 - 1)} \quad (3)$$

where d is the difference between ranks for two points within a pair (ie. difference in rank between paired reanalysis and observational data), n is the sample size (ie. count of usable GHCN observations for each 3-month season). The numerator value of 6 is always the multiplier. In using the Spearman's rank correlation, the observations are replaced with their

ranks and the correlation coefficients are then computed. It is used to identify and test the strength of the relationship between two sets of data – in this case, a reanalysis and station observations. Spearman’s rank was an optimal choice as it does not assume a normal distribution. While it was valid to assume a variety of precipitation distributions across the Arctic, histograms of precipitation at random locations were also plotted to verify this fact.

Bias was calculated by subtracting the mean seasonal observed (station) value from the mean seasonal modeled (reanalysis) value. RMSE was then calculated as the square root of the mean squared difference between the observed and reanalysis values (bias). RMSE is frequently used to measure differences between predicted model values and observations. Mathematically, RMSE can be written as:

$$\text{RMSE} = \sqrt{\frac{\sum_{i=1}^n (x_i - y_i)^2}{n}} \quad (4)$$

where $x_i - y_i$ (representing: Reanalysis data – GHCN observations) is the difference between data at a reanalysis grid node and a GHCN station. This difference is squared and divided by the count (n), or the number of monthly data values used for both reanalysis and GHCN datasets across the 32 year study period. The square root of this quantity is then calculated. In other words, the RMSE is the same as the square root of the variance, or standard error.

Further quality control included removing stations containing ≤ 20 months of usable data over each 96-month season (i.e. four 3-month seasons for the period January 1979 through December 2010). Only stations with at least 20 months of usable data ($n > 20$; $df > 18$) were kept for significance testing. To determine which correlations were significant at the 95% level ($p = 0.05$), the degrees of freedom (df) for ρ were calculated as: $df = n - 2$. Typically df are used

along with significance tables to determine this, however, with many large n values, the following formula was used to compute the critical value, c , to assess the statistical significance of the correlation coefficient:

$$c = \frac{\pm z}{\sqrt{n - 1}} \quad (5)$$

where the value of z corresponds to the significance level. For example, if the significance level is 0.05, z will equal 1.96. If c exceeds the computed critical value, it is statistically significant. Only locations with significant correlations at the 95% level were plotted. The total number of stations that fit this criterion for each three-month season is provided in **Table 5**.

Table 5. Number of stations from each reanalysis for each three-month season for which there were > 20 stations ($n > 20$) with data that had correlations statistically significant at the 95% level ($z = 1.96$; $p = 0.05$).

		Reanalysis		
		MERRA	CFSR	ERA-Interim
Number of stations retained for analysis by season:	DJF	499	497	497
	MAM	503	485	497
	JJA	504	493	502
	SON	507	508	512

4.1.2 Results

Maps showing statistically significant correlations between each reanalysis and the GHCN observations for each of the four 3-month seasons are presented in **Figures 21 – 24**; DJF, MAM, JJA, SON, respectively. Circles represent station locations. Darker shaded circles represent a stronger correlation between the two datasets; lighter shaded circles represent weaker correlations. RMSE values are expressed through the circle size; the larger the circle, the greater the RMSE value.

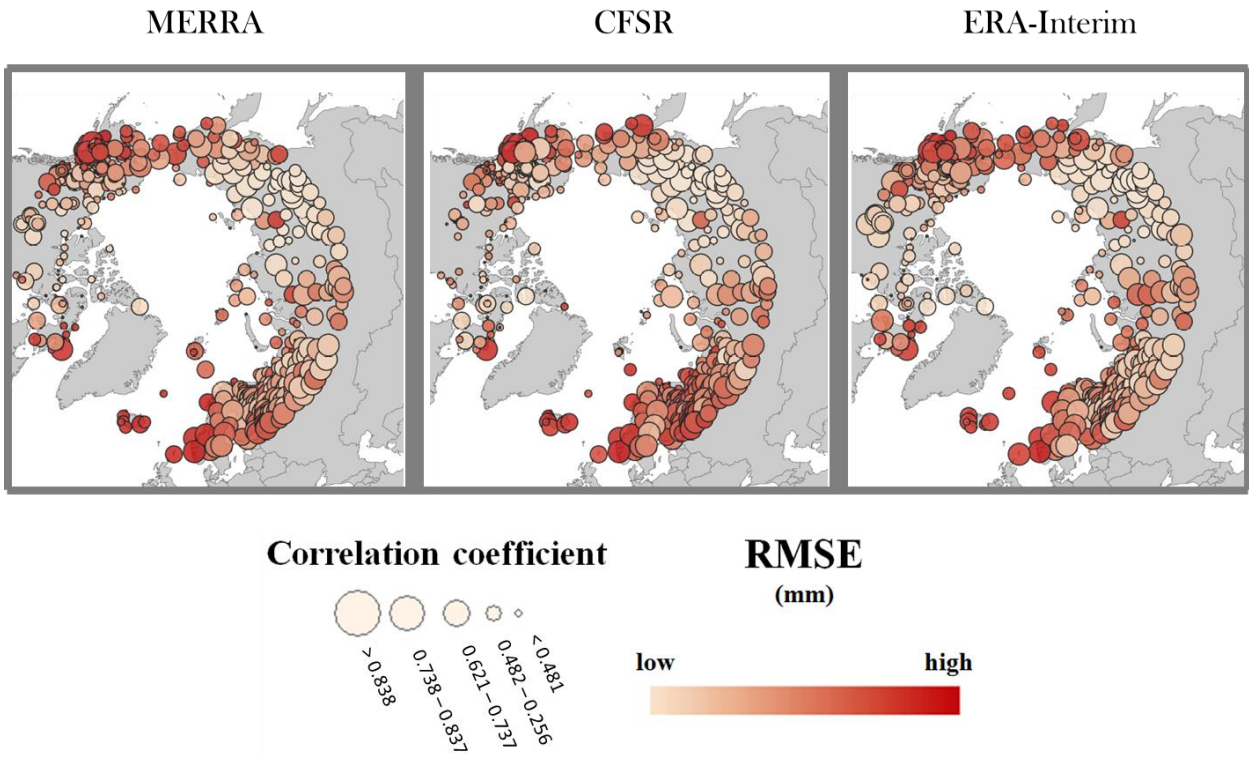


Figure 21. Correlation with GHCN observations (circle size) and RMSE (circle shading) for the winter season (DJF).

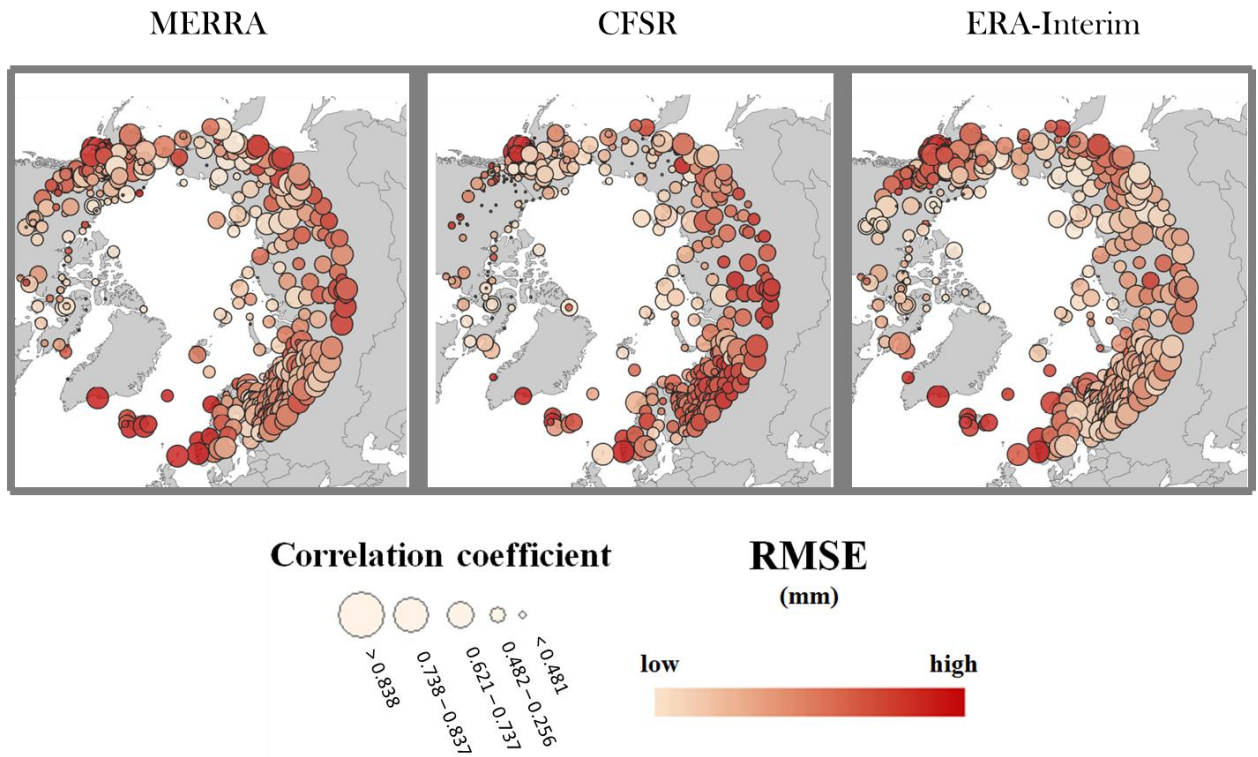


Figure 22. Correlation with GHCN observations (circle size) and RMSE (circle shading) for the spring season (MAM).

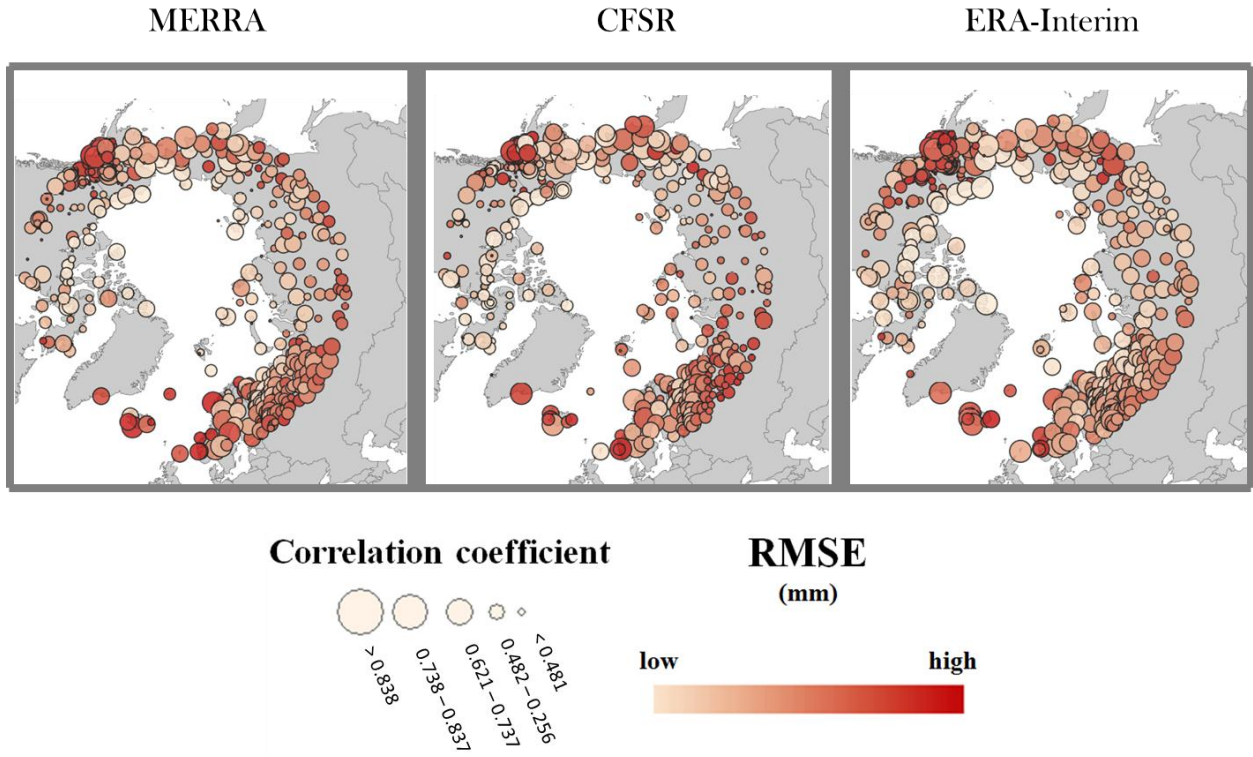


Figure 23. Correlation with GHCN observations (circle size) and RMSE (circle shading) for the summer season (JJA).

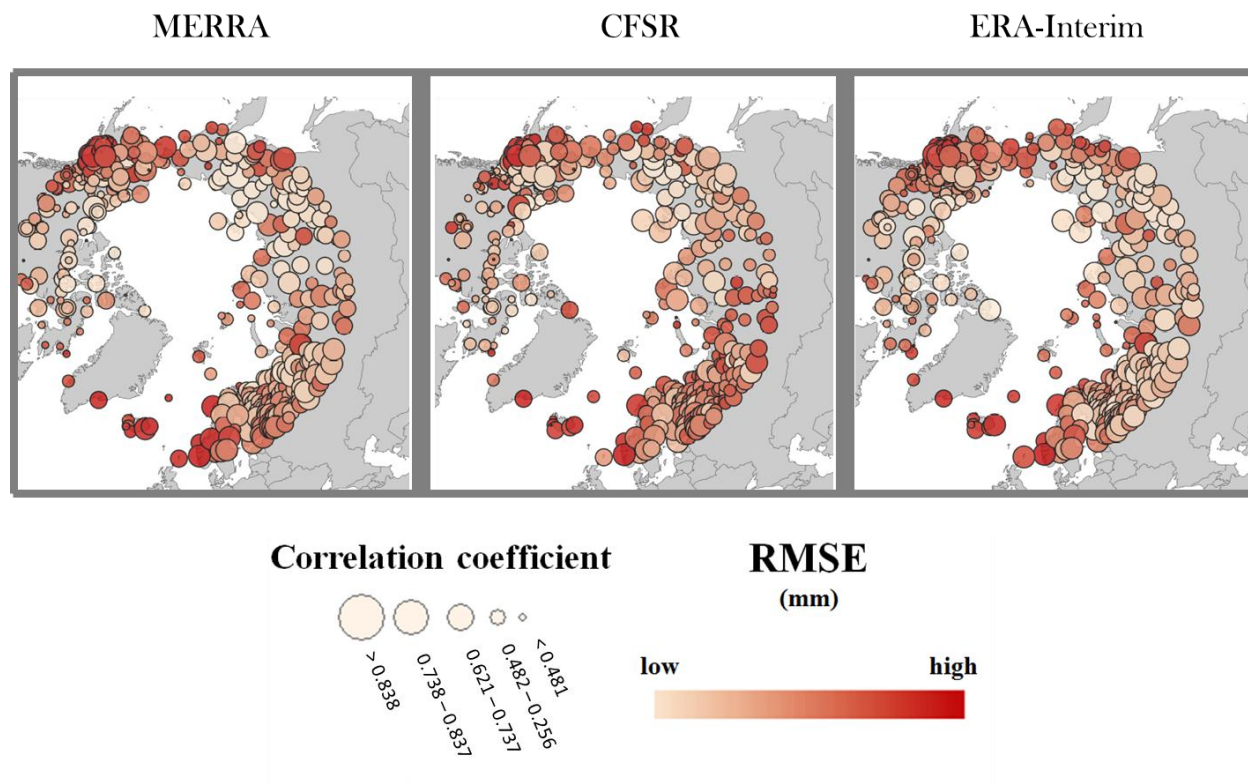


Figure 24. Correlation with GHCN observations (circle size) and RMSE (circle shading) for the autumn season (SON).

A summary table of the correlation coefficient values for the reanalyses by season is found in **Table 6**. Average, median, maximum, and minimum coefficient values are displayed. For all seasons, ERA-Interim has the highest average correlation with station data across all four seasons. **Table 7** provides a summary of the Average, median, maximum, and minimum RMSE values. CFSR has the largest error values when compared with the station observations for each of the seasons.

Table 6. Summary table of the average, median, maximum, and minimum correlation coefficient values for each season. All correlations are statistically significant at 95% ($z = 1.96$; $p < 0.05$).

		MERRA	CFSR	ERA-Interim
DJF	Average	0.697	0.696	0.726
	Median	0.717	0.714	0.741
	Max	0.957	0.974	0.966
	Min	0.239	0.255	0.257
MAM	Average	0.693	0.626	0.709
	Median	0.729	0.642	0.756
	Max	0.953	0.938	0.952
	Min	0.240	0.258	0.243
JJA	Average	0.674	0.652	0.710
	Median	0.691	0.660	0.730
	Max	0.944	0.929	0.934
	Min	0.294	0.243	0.270
SON	Average	0.714	0.712	0.737
	Median	0.742	0.729	0.761
	Max	0.953	0.962	0.955
	Min	0.299	0.309	0.355

Table 7. Summary table of the average, median, maximum, and minimum RMSE (mm) values for each season. All locations had statistically significant correlations at 95% ($z = 1.96$; $p < 0.05$).

		MERRA	CFSR	ERA-Interim
DJF	Average	21.0	29.2	22.6
	Median	11.6	23.3	11.5
	Max	402.1	432.0	405.3
	Min	1.8	1.8	2.3
MAM	Average	20.6	37.0	22.3
	Median	14.6	34.7	15.6
	Max	294.3	321.9	290.8
	Min	4.3	4.4	4.4
JJA	Average	29.9	38.1	32.3
	Median	25.1	33.1	25.4
	Max	234.6	237.6	202.2
	Min	9.0	11.8	7.3
SON	Average	28.1	38.4	30.1
	Median	17.4	30.8	17.6
	Max	457.9	382.5	354.3
	Min	5.2	6.2	5.9

A graphical representation of these same statistics (RMSE values and Spearman’s rank correlation coefficients and) as a series of boxplots is shown in **Figure 25** on the following page. It becomes apparent that the mean RMSE values for CFSR are consistently greater than for the other reanalyses. There are also many outliers among the errors; this will be important in the final analysis discussed in this chapter.

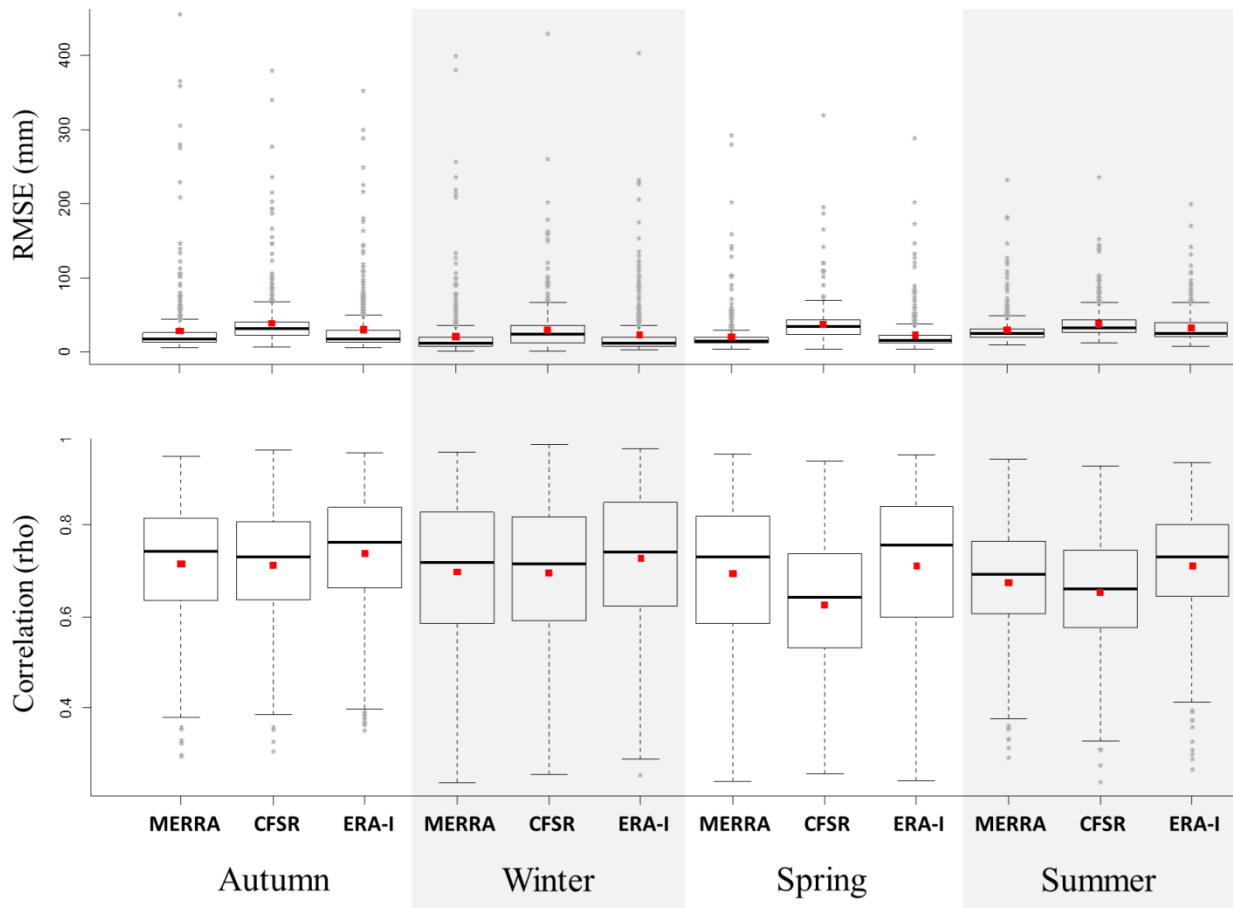


Figure 25. Boxplots of RMSE (mm) (top), and correlation coefficients (bottom) organized by season. The bold black line inside the boxes indicate the median; red squares indicates the mean. Dotted tails extending from either side of the boxes end at the maximum and minimum values, excluding outliers. Outliers are represented as grey asterisks.

Bar plots allow for easier comparison of the mean RMSE values as well as for mean biases (Figures 26 and 27). Again we notice that not only does CFSR consistently appear to be the reanalysis with the greatest error (Figure 26) but also greater model bias (Figure 27); and MERRA consistently showing the smallest mean error and bias compared to observations. Generally, model biases tended to be largest during the summer season; and lowest during the winter season. The seasonal breakdown of the number of stations, with either positive or negative biases, is found in Figure 27 in Table 8. The split between positive and negative precipitation biases appears to be less dramatic for MERRA during the DJF, JJA, and SON seasons.

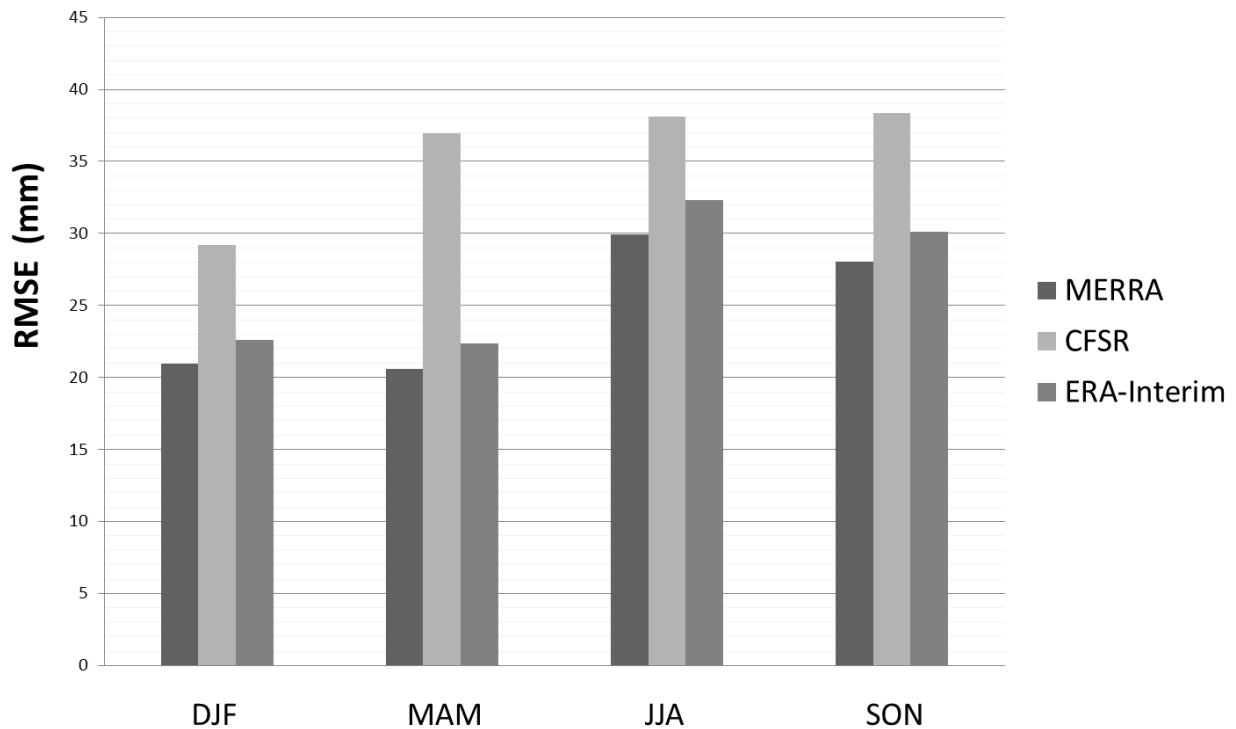


Figure 26. Average RMSE (mm) for each reanalyses across all four seasons. For each individual season, all bars are ordered, left to right: MERRA, CFSR, ERA-Interim.

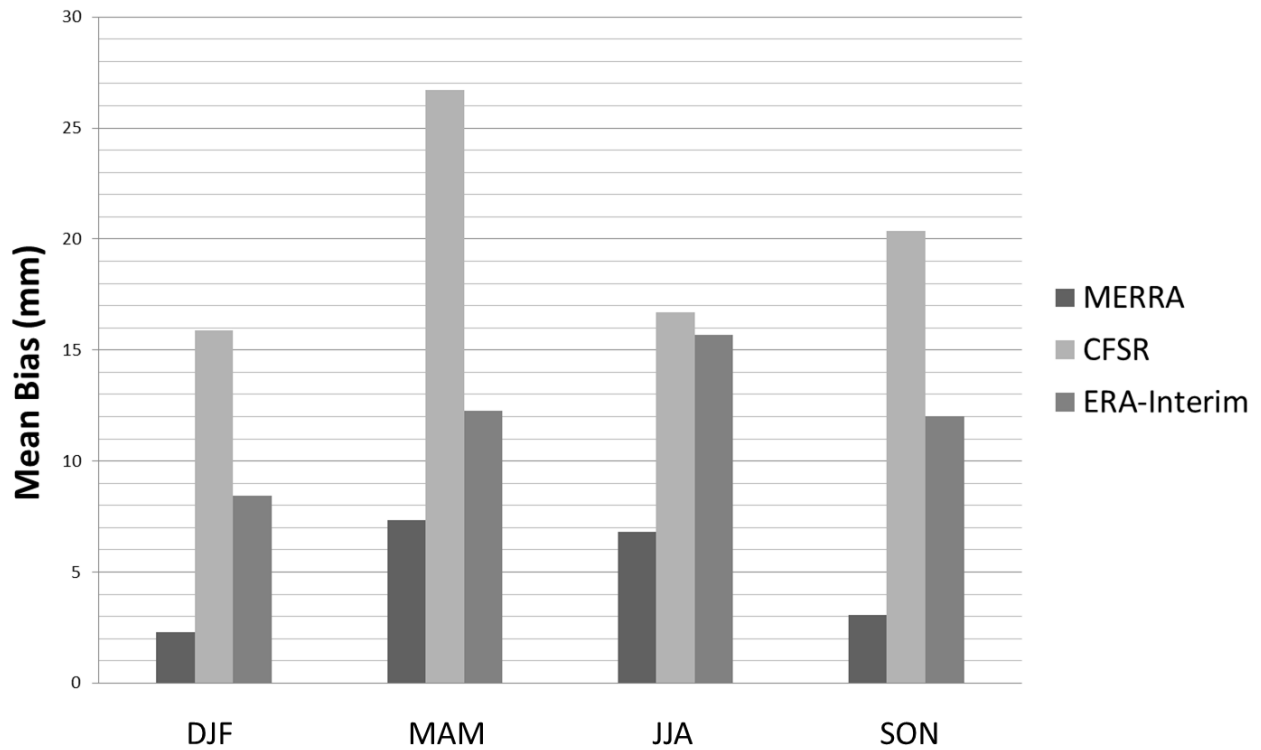


Figure 27. Average bias (mm) for each reanalyses across all four seasons. For each individual season, all bars are ordered, left to right: MERRA, CFSR, ERA-Interim. Bias was calculated as: Reanalysis data – GHCN observations.

Table 8. The number of stations with positive or negative biases for each season.

	MERRA	CFSR	ERA-Interim									
Positive	367	453	406	456	464	473	384	414	455	386	467	459
Negative	132	44	91	47	21	24	122	79	47	121	41	53
	DJF			MAM			JJA			SON		

All three of the reanalyses show positive biases across all seasons; indicating that the reanalysis are showing greater precipitation values than the observations. We might conclude from this information that the reanalyses are overestimating precipitation. However such a definitive conclusion regarding what this truly indicates, in terms of model accuracy, is difficult to make.

To elucidate if the error is being affected by the observations, plots of the RMSE values were plotted against average GHCN precipitation observations. An example of these plots is found in **Figure 28**. It becomes apparent that as observations increase, so does the amount of error. Lines of best-fit are given for each plot along with the R^2 values indicating the goodness of regression model fit. The regression models account for 81.4%, 59.95%, and 53.9% of the variance for MERRA (**a**), CFSR (**b**), and ERA-Interim (**c**), respectively. These findings suggest that RMSE values are indeed being influenced by the observations themselves. As observation values increase so does the model error.

Next, the outliers are removed and the remaining RMSE data are plotted against the mean GHCN observations again (**Figure 29**). This time the R^2 show there is less of the variance is captured by the regression models. Here we see the regression models account for 21.85%, 28.2%, and 12.29% of the variance for MERRA (**a**), CFSR (**b**), and ERA-Interim (**c**), respectively. In both cases (**Figures 28, 29**) it appears that the error associated with ERA-Interim is least influenced by the observed precipitation.

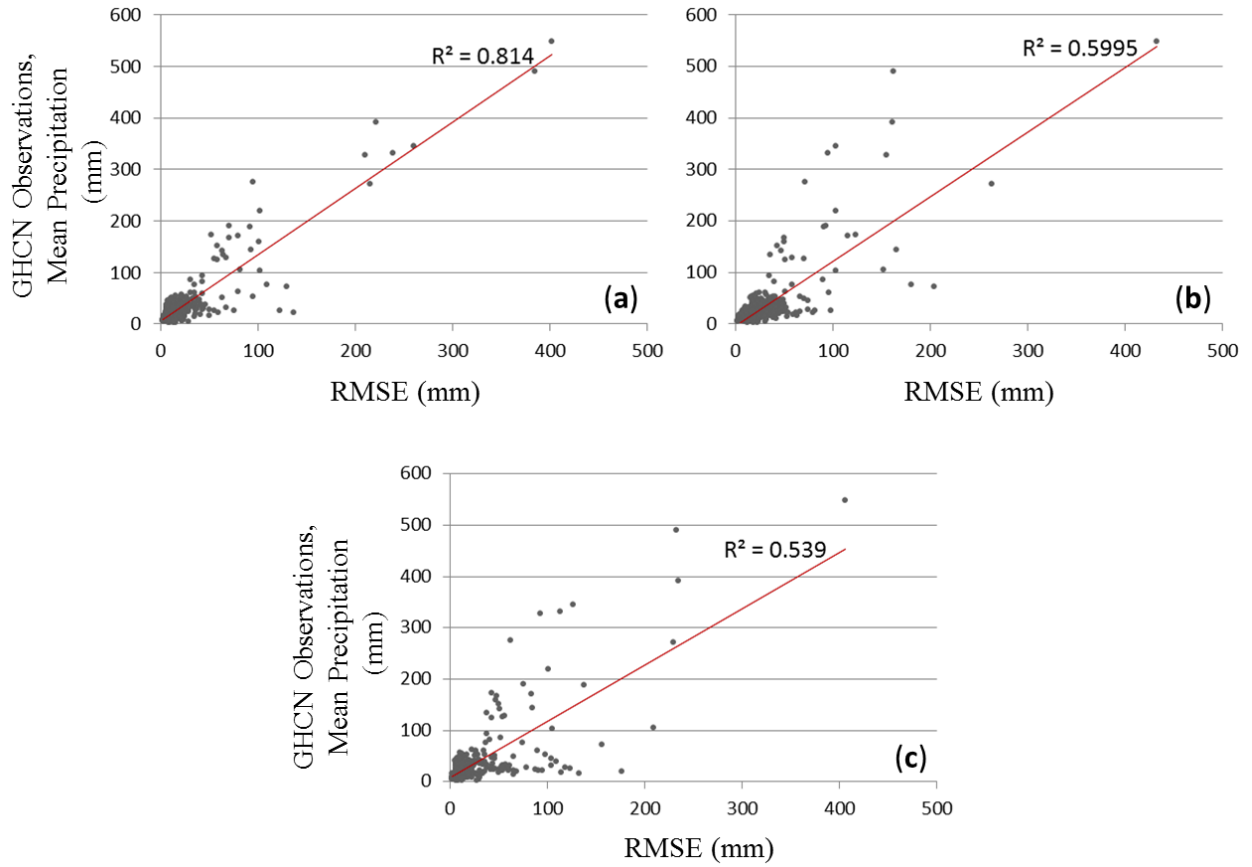


Figure 28. MERRA (a), CFSR (b), and ERA-Interim (c) RMSE values (mm) plotted against average GHCN precipitation observations (mm) for the winter (DJF) season. Regression lines (lines of best-fit) and R^2 values are included.

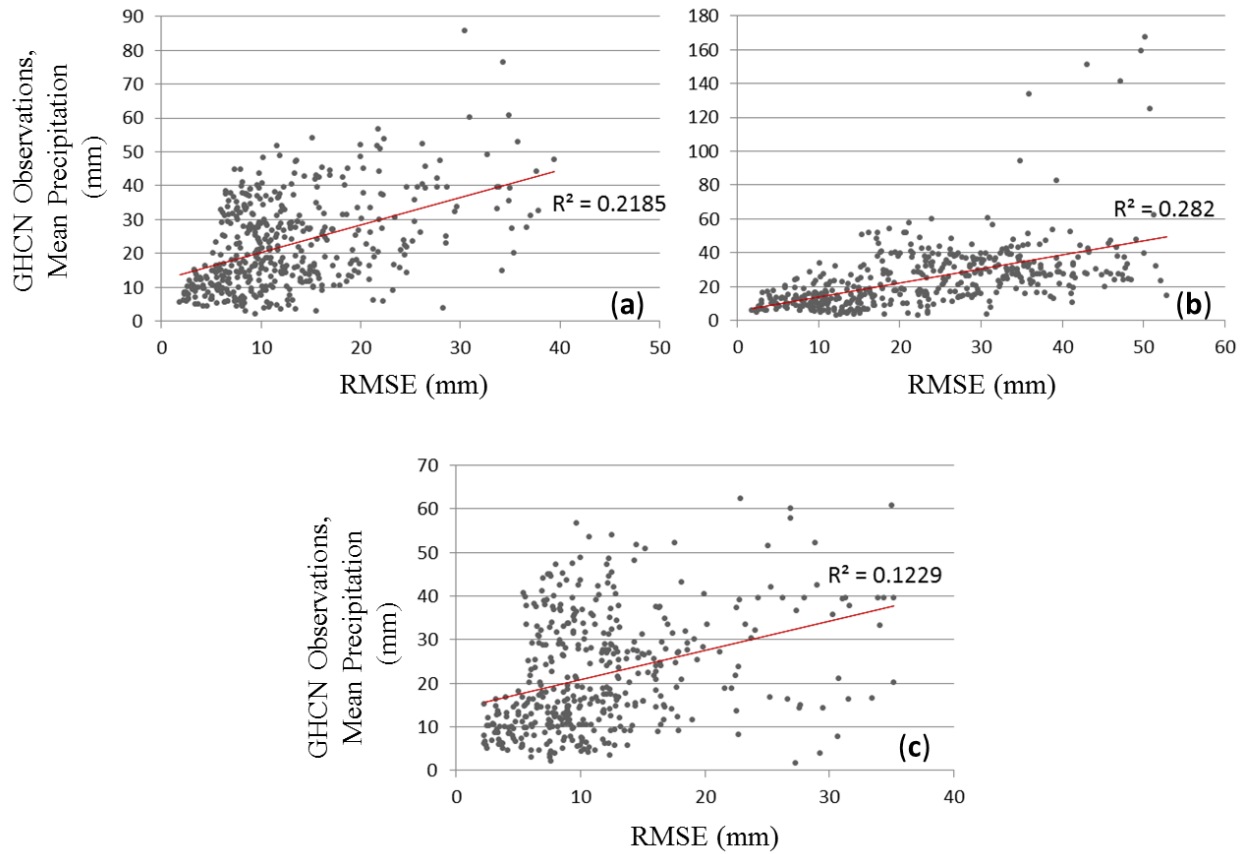


Figure 29. MERRA (a), CFSR (b), and ERA-Interim (c) RMSE values (mm) plotted against average GHCN precipitation observations (mm) for the winter (DJF) season where the outliers were removed. Regression lines (lines of best-fit) and R^2 values are included.

Knowing that station observations are subject to large undercatch biases, it is possible that the reanalyses would have the tendency to overestimate precipitation, but only because the observations are inherently biased to begin with. And so the dilemma of working with such data, which was discussed in Chapter 1, has been illustrated above. When calculating model RMSE and bias it is important to attempt to account for this inherent undercatch related bias. In an extended project the author would choose to conduct normalized error calculations in an effort to account for this dependency between the model error and the observations.

CHAPTER 5

SYNTHESIS

5.1 Discussion

This thesis examined the representation of Arctic precipitation in three atmospheric reanalysis products – MERRA, CFSR, and ERA-Interim. There were two primary objectives. The *first objective* of the study was to determine if the three atmospheric reanalyses provided an accurate depiction of the seasonal precipitation patterns. Spatial variability, recent trends, and anomalies in Arctic precipitation were investigated. Monthly precipitation averages and trends, as well as 10-year anomalies for each season were plotted. The *second objective* was to conduct a statistical validation of each of the reanalysis products through a comparison with monthly GHCN station observations. This was accomplished through statistical analysis of the reanalysis output fields and the station observations.

5.1.1 Addressing Objective I

Results from the assessment of precipitation averages, trends, and anomalies are detailed in Chapter 3. To summarize, MERRA, CFSR, and ERA-Interim all capture the known average monthly precipitation patterns across the Arctic (**Figure 7**). An investigation of trends for the past three decades reveals considerable spatial structure that is generally consistent across each reanalysis (**Figures 9 – 11**); though most long-term trends were not statistically significant. Anomaly plots for the most recent decade also show agreement across all three products

(**Figures 12 – 15**). The primary exception to this is the major discrepancy seen in ERA-Interim's output over the northern North Atlantic (Refer to Chapter 3, section 3.3).

Positive trends in precipitation are depicted over continental areas, southern Greenland, and much of the central/east Arctic Ocean during the autumn (SON) months. Negative trends in precipitation are the rule over the majority of central Eurasia, far eastern Russia. The Chukchi Sea coastal areas and southwestern Russia show negative trends during winter (DJF). Exceptions include the Scandinavian countries where strong positive trends are shown during winter, as well as the Bering Sea and western Alaska where there are strong positive trends, primarily at the end of the winter season. Spring (MAM) trends have patchier spatial patterns that continue into the summer (JJA) months, with increases of precipitation over areas of orographic lifting such as along the eastern side of the Ural Mountains in northeastern Russia and along the North Slope of Alaska. This patchy pattern is likely the result of the changes in synoptic climatology during the warmer months, when convective precipitation is more prominent over inland regions and activity along the North Atlantic storm track quiets. Instead, the storms develop over land areas creating a more variable or patchy pattern. Summer season trends point to a drying out of the southern continental regions, most noticeable during the mid-season month of July.

Regarding trends along coastal Greenland, there is high variability during spring, and the best agreement is between CFSR and ERA-Interim. The trend patterns across the Greenland ice sheet become more consistent across the reanalyses in summer. The only major discrepancy across the three reanalyses is in the trend and anomaly fields in the region encompassing the North Atlantic, including Fram Strait and the Norwegian Sea. Recall that ERA-Interim depicts negative anomalies over this region for three of the four seasons; while those trends and anomalies based on MERRA and CFSR are positive.

The trends calculated over the 32-year study period are broadly consistent with results from previous studies. Spatial variations in precipitation changes are influenced by changes in the synoptic circulation patterns, which may be linked in part to decreasing sea ice extent, as discussed previously in Chapter 1. Climate simulations from the multi-model dataset project that changes in winter precipitation, resulting from these changing atmospheric pressure patterns, project precipitation increases along the western Canadian coastal areas, southeast Alaska, and the North Atlantic (Cassano, et al., 2006). Regional climate modeling studies support this and suggest that “it is probable that there has been an increase in total precipitation over the past century at the rate of about 1% per decade” (Arctic Climate Impact Assessment, Chapter 2, 2005). The IPCC fourth assessment asserts that the projected change in the annual mean arctic precipitation varies from 10 to 28%, with an MMD-A1B ensemble median of 18% (IPCC, 2007). They show that strong correlations exist between temperature and precipitation in the model projections; and that both the sign and the magnitude (per degree warming) of the percentage precipitation change are robust among the models (IPCC, 2007).

Other studies also suggest that annual precipitation has increased across the Arctic over the past century. Findings from a now dated study across the Canadian Arctic show that over the 1950–1990 period, both annual snowfall and total precipitation increased by ~20% across northern Canada (Groisman and Easterling, 1994). In a later paper, Zhang et al., (2001) found similar positive precipitation trends when exploring 20th century changes based on data from 489 stations. Rather than focusing on annual precipitation changes, this thesis explored long-term changes for individual months, with the mindset that precipitation changes will vary spatially and by season. To this respect, the findings presented in this thesis are in agreement with the literature.

5.1.2 Addressing Objective II

The second objective of this thesis was accomplished through a statistical comparison of monthly Arctic precipitation observations with each reanalysis in an effort to provide information regarding the comparative performance for each. These results were provided in Chapter 4. Correlations between station data and the reanalyses are highest during the autumn and winter seasons and lowest during the summer; particularly over central Eurasia (**Table 6**). This is likely due to issues related to the inability of the models to accurately handle localized convective processes – a well-recognized problem. MERRA and ERA-Interim correlated best with the station data. MERRA was consistently less biased than ERA-Interim and CFSR for all seasons; with CFSR having the largest biases and errors (**Figures 26 and 27**).

Lindsay, et al. (2014) compared output from seven reanalysis products, including the three detailed in this study. The other four were: the National Centers for Environmental Prediction (NCEP) effort, the National Center for Atmospheric Research Reanalysis 1 (NCEP-R1), National Center for Atmospheric Research Reanalysis 2 (NCEP-R2), and the Japanese 25-year Reanalysis Project (JRA25). When comparing annual precipitation fields, the three top-performing reanalyses were: MERRA, ERA-Interim, and JRA-25; however they each had differing trends (Lindsay, et al., 2014). Based on comparisons with precipitation for land stations (CPC data), biases were smallest for MERRA, ERA-Interim, and JRA-25. Large biases were found for CFSR (Lindsay, et al., 2014). It is encouraging that this thesis research supports the findings of the Lindsay, et al., (2014) study.

5.1.3 Study Limitations

Despite the overall agreement, there are still considerable differences between the reanalyses. Differences between reanalyses are “an important measure of the uncertainty in any

reanalysis product, due to deficiencies and differences in the assimilating models and how the models interact with the assimilated data” (Rienecker, et al. 2011). The use of three different reanalysis products to explore precipitation points towards the author’s awareness of the existence of such uncertainties. Another considerable limitation is that improvements of precipitation assimilation methods employed in each reanalysis is extremely challenging and will likely take years of further development (Derber, 2010). Most reanalyses, including the three discussed in this study, do not assimilate precipitation directly – it is purely a forecast variable. All of the reanalyses examined here make use of satellite radiance data from hyper-spectral instruments. The seemingly better performance of MERRA compared to ERA-Interim and CFSR may be the result of improvements made within MERRA regarding assimilating satellite radiances.

While atmospheric reanalyses have in many ways revolutionized Arctic research, users should be particularly wary of forecasted precipitation due to both model biases as well as inherent challenges associated with validating such fields. This is especially important for Arctic studies and other areas where surface observations are scanty. Validating reanalysis precipitation fields in the Arctic is a somewhat circular problem. Validating Arctic precipitation fields obviously requires the use of “external” observations for comparison. However, as discussed previously, the GHCN station observations have a number of shortcomings. Namely, the low density of stations with which to compare with the models means that vast areas are unresolved. This is especially true across complex terrain. One cannot expect to get a good correlation between the precipitation measured at a station and precipitation at the closest grid node in the reanalysis. This is resultant from the likelihood of single station to give a poor representation of the regional precipitation. The problem of low station density will be especially pronounced in

summer, when more of the precipitation is from local convection. Findings detailed in Chapter 4 suggest that RMSE values are being influenced by the number of observations themselves. It appears that as observation values increase so does the model error.

Keeping with the theme of surface observations, it is also important that the time-period of emphasis in studies relating to Arctic precipitation is highly dependent on data availability, often coinciding with the establishment of station networks in a particular region. For example, many observing stations were not operational in Canadian Arctic locations until the 1940s (Groisman and Easterling, 1994). The former Soviet Union once had an extensive network, with some station records dating back to the ~1910s. Unfortunately, there has been an overall decline in both reporting frequency and number of operational stations since 1990 following the breakup of the Soviet Union. The author encountered this problem in assessing the GHCN data used for this study, with many stations across Russia having a wealth of data extending back to the 1910s but limited data for the post-1989 study period. The continued lack of gauge standardization, changes in the number of observations per day, and inconsistent corrections to precipitation observations have added further to difficulties in assessing Arctic precipitation (Groisman and Rankova, 2001).

Pinpointing the exact cause resulting in the differences between products would be a painstaking, near-impossible task thanks to the immense complexity of these reanalysis systems. It can be particularly difficult to assess exactly what data were used and the complexity of the assimilation system. The author believes that the further investigation of the differences in the precipitation assimilation processes could shed light on the large discrepancy found in wintertime precipitation across the North Atlantic sector.

Regardless, reanalyses remain useful tools to add to the Arctic science toolbox. Serreze et al. (2005) evaluated monthly precipitation from three earlier generation reanalyses (ECMWF ERA-40, NCEP-R1 and ERA (ERA-15), as well as satellite-derived estimates over latitudes north of 45°N. Findings showed that reanalyses provided better estimates of precipitation across the Arctic than did the satellite data. The use of reanalysis output to study Arctic precipitation is a win-win as it is yet another tool at scientists' disposal; and reanalyses also currently outperform satellite retrievals.

5.2 Conclusions

Results indicate that, from the viewpoint of the reanalyses, precipitation changes over the past three decades are variable and dependent upon season. MERRA, CFSR, and ERA-Interim give similar mean precipitation patterns across the Arctic for all seasons. Each captures the contrasting seasonal cycles over land (summer maximum, winter minimum) and the Atlantic sector (winter maximum, summer minimum).

This research also addressed uncertainties within reanalyses by demonstrating cross-model differences in relation to station observations. Such uncertainties continue to be a heavily discussed topic within the reanalysis community. Of the three reanalyses, MERRA was found to have smallest biases and errors (using both RMSE and MAE methods) compared to its counterparts. ERA-Interim is a close second; with CFSR have peculiarly large biases and errors. While these results are contingent upon the inherent limitations of the GHCN station data, these findings are in agreement with the recent study by Lindsay, et al. (2014). Results from this thesis serve as a resource regarding the performance of these three reanalyses across northern high latitudes for precipitation studies. This is extremely pertinent considering that many of the initial validations discussed in the original technical documentation, as well as later peer-

reviewed studies, tend to address precipitation on a global scale, but only ranging across the mid-latitudes (typically from 60°N to 60°S). However, good performance at mid-latitude does not always transfer to good performance at higher latitudes; similarly reanalysis performance can vary greatly depending on variable fields, especially difficult-to-model fields, such as precipitation.

5.3 Future Work

This research sets the foundation for exploring regional changes in precipitation, particularly in the form of snow³. For example, the precipitation from MERRA, the best-performing product could be used to drive a land surface model in an effort to investigate how snow cover changes affect the ground thermal regime. Snow cover changes are of particular importance because the soil column thaws from the surface downward through spring and summer; the maximum depth of seasonal thaw is termed the active layer. Seasonal freeze-up of the soil column also occurs from the top down through conduction and subsequent heat loss to the atmosphere. A deeper winter snowpack will reduce the rate of heat loss from the soil column. However, a warmer climate with an earlier spring snow melt will lead to a stronger seasonal heat gain in the soil column. Persistence of this pattern of seasonal anomalies can lead to a situation where the soil column does not completely freeze in winter, leaving an unfrozen layer at depth called thermokarst which marks the onset on rapid permafrost decay (Zhang, et al., 2005).

Another application of the findings gleaned from this research is to monitor precipitation over the Arctic Ocean – and area where it is notoriously difficult to obtain accurate measurements. Atmospheric reanalyses could be used to represent snow cover over sea ice,

³ Snow and rain are separate precipitation fields within the reanalyses.

which could be used to improve retrievals of sea ice thickness from the upcoming NASA's IceSat-2 (Ice Cloud and land Elevation Satellite) mission; the second generation of the laser altimeter IceSat mission that ended abruptly in 2010 (Abdalati, et al., 2010). IceSat-2 is projected to launch in 2017. In order to determine sea ice thickness there is the dilemma of snow on ice, to calculate ice thicknesses, the depth of the snow cover atop the ice must be known. It has been demonstrated that precipitation fields in atmospheric reanalyses tend to correspond better than satellite data (Serreze, Barrett, and Lo, 2005). Perhaps reanalyses could be utilized to provide the needed snow depth estimates.

With regards to further reanalysis validation studies, it will be useful to conduct a study comparing MERRA with the new MERRA-Land product, which incorporates surface observations to inform the model. In particular, it would be valuable to examine how the direct assimilation of surface observations changes the precipitation fields. Broadly, this thesis provides useful information regarding the performances of the current generation of atmospheric reanalyses. This, along with similar studies, will allow users to make informed decisions on which reanalyses to use for high-latitude hydrologic monitoring applications.

REFERENCES

- Abdalati, W., H.J. Zwally, R. Bindenschadler, B. Csatho, S. L. Farrell, H.A. Fricker, D. Harding, R. Kwok, M. Lefsky, T. Markus, A. Marshak, T. Neumann, S. Palm, B. Schutz, B. Smith, J. Spinhirne, and C. Webb. (2010), The ICESat-2 Laser Altimetry Mission, *Proceedings of the IEEE*, 98(5), 735–751.
- Arctic Climate Impact Assessment, Scientific Report (2005), Chapter 2: Arctic Climate –Past and Present, 21–60. [Available at: http://www.acia.uaf.edu/PDFs/ACIA_Science_Chapters_Final/ACIA_Ch02_Final.pdf].
- Bintanja, R., and F.M. Selten (2014), Future increases in Arctic precipitation linked to local evaporation and sea-ice retreat, *Nature*, 509(7501), 479-482, doi: 10.1038/nature13259.
- Bloom, S.C., L.L.Takacs, A.M. Da da Silva, and D. Ledvina (1996) Data assimilation using incremental analysis updates, *Monthly Weather Review*, 124, 1256–1271.
- Bosilovich, M.G., M. Rixen, P. van Oevelen, G. Asrar, G. Compo, K. Onogi, A. Simmons, K. Trenberth, and others (2012), Report of the 4th World Climate Research Programme International Conference on Reanalyses, *Conference Report*, 41 pp., 7-11 May 2012, Silver Spring, Maryland, USA. [Available at: http://www.wcrpclimate.org/documents/ICR4_Report.pdf].
- Bosilovich, M.G., J. Chen, F.R. Robertson, and R.F. Adler (2008), Evaluation of Global Precipitation in Reanalyses, *Journal of Applied Meteorology Climatology*, 47, 2279–2299, doi: <http://dx.doi.org/10.1175/2008JAMC1921.1>.
- Cassano, J.J., P. Uotila, and A. Lynch (2006), Changes in synoptic weather patterns in the polar regions in the twentieth and twenty-first centuries, part 1: Arctic, *International Journal of Climatology*, 26(8), 1027–1049, doi: 10.1002/joc.1306.
- Cullather, R.I., and M.G. Bosilovich (2011), The moisture budget of the polar atmosphere in MERRA, *Journal of Climate*, 24, 2861–2879, doi: <http://dx.doi.org/10.1175/2010JCLI4090.1>.
- Dee, D.P., S. Uppala, A.J. Simmons, P. Berrisford, P. Poli, S. Kobayashi, et al. (2011), The ERA-Interim reanalysis: Configuration and performance of the data assimilation system, *Quarterly Journal of the Royal Meteorological Society*, 137(656), 553–597, doi: 10.1002/qj.828.
- Dee, D.P., and S. Uppala (2009), Variational bias correction of satellite radiance data in the ERA-Interim reanalysis, *Quarterly Journal of the Royal Meteorological Society*, 135(644), 1830–1841, doi: 10.1002/qj.493.
- Derber, J.C. (2010), Presentation: Satellite Radiance Assimilation. Environmental Modeling Center, NCEP/NWS/NOAA. [Available at: http://www.dtcenter.org/com/GSI/users/docs/presentations/2010_tutorial/L9-0629/Satellite_Radiance_Assimilation_JohnDerber.ppt.pdf].

- Deser, C., A. Phillips, V. Bourdette, and H. Teng (2012), Uncertainty in climate change projections: the role of internal variability, *Climate Dynamics*, 38(3-4), 527–546, doi: 10.1007/s00382-010-0977-x.
- Ek M.B., K.E. Mitchell, Y. Lin, E. Rogers, P. Grunmann, V. Koren, G. Gayno, and J.D. Tarplay, (2003), Implementation of the Noah land-use model advances in the NCEP operational mesoscale Eta model. *Journal of Geophysical Research*, 108(D22), 8851, 16 pp., doi: 10.1029/2002JD003296.
- Francis, J.A. and S.J. Vavrus (2012), Evidence linking Arctic amplification to extreme weather in mid-latitudes, *Geophysical Research Letters*, 39, L06801, doi: 10.1029/2012GL051000.
- Francis, J.A., W. Chan, D.J. Leathers, J.R. Miller, and D.E. Veron (2009), Winter Northern Hemisphere weather patterns remember summer Arctic sea-ice extent. *Geophysical Research Letters*, 36, L07503, doi: 10.1029/2009GL037274.
- Francis, J.A., and E. Hunter (2006), New insight into the disappearing Arctic sea ice, *Eos, Transactions American Geophysical Union*, 87(46), 509-511, doi: 10.1029/2006EO460001.
- Finnis, J., M.M. Holland, M.C. Serreze, and J.J. Cassano (2007), Response of Northern Hemisphere extratropical cyclone activity and associated precipitation to climate change, as represented by the Community Climate System Model, *Journal of Geophysical Research: Biogeosciences (2005–2012)*, 112, G04S42, doi: 10.1029/2006JG000286.
- Geer, A.J., P. Bauer, P. Lopez (2008), Lessons learnt from the operational 1D+4D-Var assimilation of rain- and cloud-affected SSM/I observations at ECMWF. *Quarterly Journal of the Royal Meteorological Society*, 134, 1513–1525.
- Groisman, P.Y., and E.Y. Rankova (2001), Precipitation trends over the Russian permafrost-free zone: removing the artifacts of pre-processing, *International Journal of Climatology*, 21(6), 657–678. doi: 10.1002/joc.627.
- Groisman, P.Y., and D.R. Easterling (1994), Variability and trends of total precipitation and snowfall over the United States and Canada, *Journal of Climate*, 7(1), 184–205.
- Hansen J., M. Sato., R. Ruedy, K. Lo, D.W. Lea, and M. Medina-Elizade (2006), *Proceedings of the National Academy of Sciences, USA*, 103(39), 14288–14293, doi: 10.1073/pnas.0606291103.
- Hinkel K.M., F.E. Nelson (2003), Spatial and temporal patterns of active layer depth at CALM sites in northern Alaska, 1995–2000, *Journal of Geophysical Research*, 108(D2), doi: 10.129/2001JD000927.

- Hinzman, L.D., D.L. Kane, C.S. Benson, and K.R. Everett (1991), Hydrologic and Thermal Properties of the Active Layer in the Alaskan Arctic, *Cold Regions Science and Technology*, 19(2), 95-110.
- Hirsch, R. M., J. R. Slack, and R. A. Smith (1982), Techniques of trend analysis for monthly water-quality data, *Water Resources Research*, 18, 107-121.
- Hu, et al, (2009), Gridpoint Statistical Interpolation (GSI), User's Guide V1.0. 67 pp. [For most recent version, refer to: <http://www.dtcenter.org/com-GSI/users/index.php>].
- IPCC, Climate Change 2007: Synthesis Report (2007), Section 1.1 Observations of climate change. [Available at: http://www.ipcc.ch/publications_and_data/ar4/syr/en/mains1.html].
- IPCC, Climate Change 2007: Working Group I: The Physical Science Basis: 11.8.1 Precipitation, (2007). [Available at: http://www.ipcc.ch/publications_and_data/ar4/wg1/en/ch11s11-8-1-5-precipitation.html].
- Juang, H.-M. (2005), Discrete generalized hybrid vertical coordinates by a mass, energy and angular momentum conserving vertical finite-differencing scheme, NCEP Office Note 445, 33 pp. [Available online at: <http://www.emc.ncep.noaa.gov/officenotes/FullTOC.html#2000>].
- Kattsov V.M., J.E. Walsh, W.L. Chapman, V. Govorkova, T.V. Pavlova, X. Zhang (2007), Simulation and projection of Arctic freshwater budget components by the IPCC AR4 global climate models, *Journal of Hydrometeorology*, 8, 571–589, doi: 10.1175/JHM575.1.
- Kendall, M. G. (1975), Rank Correlation Methods, 4th ed. Charles Griffin: London, UK, 272 pp.
- Kleist, D.T., D.F. Parrish, J.C. Derber, R. Treadon, R.M. Errico, and R. Yang (2009a), Improving Incremental Balance in the GSI 3DVAR Analysis System, *Monthly Weather Review*, 137, 1046-106
- Kleist, D.T., D.F. Parrish, J.C. Derber, R. Treadon W-S. Wu, and S. Lord (2009b), Introduction of the GSI into the NCEP Global Data Assimilation System, *Weather and Forecasting*, 24, 1691–1705, doi: 10.1175/2009WAF2222201.1.
- Koster, R.D., M.J. Suarez, A. Ducharne M. Stieglitz, P. Kumar (2000), A catchment-based approach to modeling land surface processes in a general circulation model: 1. Model structure, *Journal of Geophysical Research: Atmospheres*, 105(D20), 24809–2482, doi: 10.1029/2000JD900327.

- Lawrence, D. M. and A. G. Slater (2005), A projection of severe near-surface permafrost degradation during the 21st century. *Geophysical Research Letters*, 32(24), | doi: 10.1029/2005GL025080.
- Lawrimore, J.H., M.J. Menne, B.E. Gleason, C.N. Williams, D.B. Wuertz, R.S. Vose, and J. Rennie (2011), An overview of the Global Historical Climatology Network monthly mean temperature data set, version 3, *Journal of Geophysical Research*, 116, D19121, doi: 10.1029/2011JD016187.
- Lindsay, R., M. Wensnahan, A. Schweiger, and J. Zhang (2014), Evaluation of seven different atmospheric reanalysis products in the Arctic. *Journal of Climate*, 27(7), 2588–2606, doi: <http://dx.doi.org/10.1175/JCLI-D-13-00014.1>.
- Ling, F., and T. Zhang. 2004. A numerical model for surface energy balance and thermal regime of the active layer and permafrost containing unfrozen water. *Cold Regions Science and Technology*, 38(1), 1–15, doi: 10.1016/S0165-232X(03)00057-0.
- Liston, G. E. and M. Sturm (2002), Winter precipitation patterns in arctic Alaska determined from a blowing-snow model and snow-depth observations. *Journal of Hydrometeorology*, 3(6), 646–659.
- Lorenz, E. N. (1963), Deterministic nonperiodic flow. *Journal of the Atmospheric Sciences*, 20(2), 130–141.
- Lucchesi, R. (2012), File Specification for MERRA products, Global Modeling and Assimilation Office, GMAO Office Note No. 1, Version 2.3, 81 pp.
- NASA GISS. GISS Surface Temperature Analysis: Global Maps from GHCN v3 Data (web resource), <http://data.giss.nasa.gov/gistemp/maps/>.
- NOAA. Arctic Change, Land-Rivers (web resource), <http://www.arctic.noaa.gov/detect/land-river.shtml>.
[Arctic drainage basins Map (image URL):
http://www.arctic.noaa.gov/detect/detection-images/land-arctic-rivers_gro-375.jpg].
- NSIDC. Sea Ice (web resource), http://nsidc.org/cryosphere/sotc/sea_ice.html.
- Okamoto K. and J. Derber (2006). Assimilation of SSM/I Radiances in the NCEP Global Data Assimilation System, *Monthly Weather Review*, 134(9), doi: 10.1175/MWR3205.1.
- Phillips, N.A. (1957) A coordinate system having some special advantages for numerical forecasting, *Journal of Meteorology*, 14, 184–185.
- Rasmussen, R., B. Baker, J. Kochendorfer, T. Meyers, S. Landolt, A.P. Fischer, et al. (2012), How well are we measuring snow: the NOAA/FAA/NCAR winter precipitation test bed, *Bulletin of the American Meteorological Society*, 93(6), 811–829.

- Rienecker, M.M., M.J. Suarez, R. Gelaro, R. Todling, J. Bacmeister, E. Liu, Michael G. Bosilovich, S.D. Schubert, L. Takacs, G.-K. Kim, S. Bloom, J. Chen, D. Collins, A. Conaty, A. da Silva, et al. (2011), MERRA: NASA's Modern-Era Retrospective Analysis for Research and Applications. *Journal of Climate*, 24, 3624–3648, doi: 10.1175/JCLI-D11-00015.1.
- Rienecker, M.M., R. Todling, J. Bacmeister, L. Takacs, H-C. Liu, W. Gu, M. Sienkiewicz, R.D. Koster, R. Gelaro, I. Stajner, and J.E. Nielsen (2008), The GEOS-5 Data Assimilation System-Documentation of Versions 5.0. 1, 5.1. 0, and 5.2. 0., *NASA/TM-2008-104606*, Vol. 27, 118 pp.
- Saha, S., S Moorthi, H-L. Pan, X. Wu, J. Wang, S. Nadiga, P. Tripp, R. Kistler, J. Woollen, D. Behringer, Haixia Liu, D. Stokes, R. Grumbine, G. Gayno, J. Wang, Y-T. Hou, H-Y. Chuang, Hann-Ming H. Juang, J. Sela, M. Iredell, R. Treadon, D. Kleist, P. Delst, Dennis K., John D., Michael E. Jesse M., H. Wei, R. Yang, S. Lord, H. Dool, A. Kumar, W. Wang, C. Long, M. Chelliah, Y. Xue, B. Huang, J-K. Schemm, W. Ebisuzaki, R. Lin, P. Xie, M. Chen, S. Zhou, W. Higgins, C-Z. Zou, Q. Liu, Y. Chen, Y. Han, L. Cucurull, R. W. Reynolds, G. Rutledge, and M. Goldberg (2010), The NCEP Climate Forecast System Reanalysis. *Bulletin of the American Meteorological Society*, 91(8), 1015–1057. doi: 10.1175/2010BAMS3001.2.S1.
- Schuenemann, K., and J.J. Cassano (2009), Changes in synoptic weather patterns and Greenland precipitation in the 20th and 21st centuries. Part 1: Evaluation of late 20th century simulations from IPCC models, *Journal of Geophysical Research*, 114, D20113, doi: 10.1029/2009JD011705.
- Screen, J.A., and I. Simmonds (2010), The central role of diminishing sea ice in recent Arctic temperature amplification, *Nature*, 464, 1334–1337, doi: 10.1038/nature09051.
- Serreze, M.C., and Barry, R.G. (2011), Processes and impacts of Arctic amplification: A research synthesis. *Global and Planetary Change*, 77(1), 85–96, doi: 10.1016/j.gloplacha.2011.03.004.
- Serreze, M.C., A.P. Barrett, J.C. Stroeve, D.N. Kindig and M.M. Holland (2009), The emergence of surface-based Arctic amplification. *The Cryosphere Discussions*, 2, 601–622.
- Serreze, M.C., and A.P. Barrett, A.P. (2008). The Summer Cyclone Maximum over the Central Arctic Ocean. *Journal of Climate*, 21(5), 1048–1065, doi: 10.1175/2007JCLI1810.1.
- Serreze, M.C., A. P. Barrett, A.G. Slater, M. Steele, J. Zhang, K. E. Trenberth (2007), The large scale energy budget of the Arctic. *Geophysical Research Letters*., 112, D11122, doi: 10.1029/2006JD008230

- Serreze, M.C., A.P. Barrett, and F. Lo (2005), Northern high-latitude precipitation as depicted by atmospheric reanalyses and satellite retrievals, *Monthly Weather Review*, 133(12), 3407–3430, doi: <http://dx.doi.org/10.1175/2FMWR3047.1>.
- Serreze, M.C., and R.G. Barry (2005, Chapter 6), *The Arctic Climate System*, Cambridge, England: Cambridge University Press, 385 pp.
- Simmons, A.J., S.M. Uppala, D.P. Dee, S. Kobayashi (2007a), ‘ERA-Interim: New ECMWF reanalysis products from 1989 onwards,’ *ECMWF Newsletter* 110: 25–35.
- Simmons, A.J., S.M. Uppala, D.P. Dee (2007b), ‘Update on ERA-Interim,’ *ECMWF Newsletter* 111: 5.
- Simmons, A.J., and A. Hollingsworth (2002), Some aspects of the improvement in skill of numerical weather prediction, *Quarterly Journal of the Royal Meteorological Society*, 128(580), 647–677, doi: 10.1256/003590002321042135.
- Simmonds, I., and K. Keay (2009), Extraordinary September Arctic sea ice reductions and their relationships with storm behavior over 1979–2008, *Geophysical Research Letters*, 36(19),
- Stieglitz, M., S.J. Déry, V.E. Romanovsky, and T.E. Osterkamp (2003), The role of snow cover in the warming of arctic permafrost, *Geophysical Research Letters*, 30(13), 1721, doi: 10.1029/2003GL017337.
- Stieglitz, M., A. Ducharme, R. Koster, and M. Suarez (2001), The impact of detailed snow physics in the simulation of snow cover and subsurface thermodynamics at continental scales, *Journal of Hydrometeorology*, 2, 228–242.
- Stroeve, J.C., M.C. Serreze, A. Barrett, and D.N. Kindig (2011), Attribution of recent changes in autumn cyclone associated precipitation in the Arctic, *Tellus*, 63(4): 653–663, doi: 10.1111/j.1600-0870.2011.00515.x.
- Stroeve, J., M.C. Serreze, S. Drobot, S. Gearheard, M. Holland, J. Maslanik, W. Meier, T. Scambos (2008), Arctic sea ice extent plummets in 2007, *Eos, Transactions American Geophysical Union*, 89(2), 13–14, doi: 10.1029/2008EO020001.
- Stroeve, J., M.M. Holland, W. Meier, T. Scambos, and M. Serreze (2007), Arctic sea ice decline: Faster than forecast, *Geophysical Research Letters*, 34, L09501, doi: 10.1029/2007GL029703.
- Sugiura, K., T. Ohata, and D. Yang (2006), Catch characteristics of precipitation gauges in high-latitude regions with high winds, *Journal of Hydrometeorology*, 7(5), 984–994.

- Tavolato, C., and L. Isaksen (2010), 'Data usage and quality control for ERA-40, ERA-Interim, and the operational ECMWF data assimilation system,' ERA Report Series, No. 7, ECMWF: Reading, UK.
- Treadon, R.E., H.L. Pan, W.S. Wu., Y. Lin, W.S. Olson, and R.J. Kuligowski (2002), Global and regional moisture analyses at NCEP. In Proc. ECMWF/GEWEX workshop on humidity analysis, 33–47.
- Wang, X., and J.R. Key, 2005: Arctic surface, cloud, and radiation properties based on the AVHRR Polar Pathfinder dataset. Part I: Spatial and Temporal Characteristics. *Journal of Climate*, 18, 2558–2574, doi: <http://dx.doi.org/10.1175/JCLI3438.1>.
- Willmott, C.J. and Matsuura, K. (2005), Advantages of the mean absolute error (MAE) over the root mean square error (RMSE) in assessing average model performance. *Climate Research*, 30(1), 79–82.
- Woo, M.K., and T.C. Winter (1993), The role of permafrost and seasonal frost in the hydrology of northern wetlands in North America, *Journal of Hydrology*, 141, 5–31.
- Woodruff, S.D., R.J. Slutz, R.L. Jenne, and P.M. Steurer, 1987: A comprehensive ocean atmosphere data set. *Bulletin of American Meteorological Society*, 68, 1239-1250.
- Xie, P., M. Chen, A. Yatagai, T. Hayasaka, Y. Fukushima, and S. Yang (2007), A gauge based analysis of daily precipitation over East Asia, *Journal of Hydrometeorology*, 8, 607–626.
- Xie, P., and P.A. Arkin (1997), Global precipitation: A 17-year monthly analysis based on gauge observations, satellite estimates, and numerical model outputs, *Bulletin of American Meteorological Society*, 78, 2539–2558.
- Yang, D., D. Kane, Z. Zhang, D. Legates, and Goodison, B. (2005), Bias corrections of long term (1973–2004) daily precipitation data over the northern regions. *Geophysical Research Letters*, 32, L19501, doi: 10.1029/2005GL024057.
- Yang, D., and T. Ohata (2001), A bias corrected Siberian regional precipitation climatology, *Journal of Hydrometeorology*, 2, 122–139.
- Zhang, T., O.W. Frauenfeld, M.C. Serreze, A.J. Etringer, C. Oelke, J.L. McCreight, R.G. Barry, D. Gilichinsky, D. Yang, H. Ye, L. Feng, and S. Chudinova (2005), Spatial and temporal variability in active layer thickness over the Russian Arctic Drainage Basin. *Journal of Geophysical Research*, 110, doi: 10.1029/2004JD005642.
- Zhang, X., W.D. Hogg, and É. Mekis (2001), Spatial and temporal characteristics of heavy precipitation events over Canada. *Journal of Climate*, 14(9). 1923–1936.

- Zhang, T., R.G. Barry, K. Knowles, J.A. Heginbottom, and J. Brown, (1999), Statistics and characteristics of permafrost and ground-ice distribution in the Northern Hemisphere 1. *Polar Geography*, 23(2), 132–154.
- Zimov, S.A., E.A.G. Schuur, F.S. Chapin III (2006), Permafrost and the global carbon budget, *Science*, 312(5780), 1612–1613, doi: 10.1126/science.1128908.
- Zuidema, P., B. Baker, Y. Han, J. Intrieri, J. Key, P. Lawson, S. Matrosov, M. Shupe, R. Stone, and T. Uttal (2005), An Arctic springtime mixed-phase cloudy boundary layer observed during SHEBA., *Journal of the Atmospheric Sciences*, 62(1), 160–176, doi: <http://dx.doi.org/10.1175/JAS-3368.1>.

APPENDIX A. GHCN STATIONS AND THEIR LOCATIONS

Station ID	Location	Latitude	Longitude
CA002100115	ANNIE LAKE ROBINSON	60.47 °N	134.83 °W
CA002100120	ANVIL	62.37 °N	133.38 °W
CA002100160	BEAVER CREEK ARPT	62.417 °N	140.867 °W
CA002100161	BEAVER CREEK ARPT	62.383 °N	140.883 °W
CA002100163	BLANCHARD RIVER	60 °N	136.77 °W
CA002100167	BRAEBURN	61.47 °N	135.78 °W
CA002100174	BRYN MYRDDIN FARM	60.87 °N	135.38 °W
CA002100182	BURWASH (AUTO8)	61.367 °N	139.05 °W
CA002100200	CARCROSS	60.18 °N	134.7 °W
CA002100300	CARMACKS	62.117 °N	136.183 °W
CA002100402	DAWSON AIRPORT	64.05 °N	139.133 °W
CA002100430	DEZADEASH	60.37 °N	137.05 °W
CA002100460	DRURY CREEK	62.2 °N	134.383 °W
CA002100468	EAGLE PLAINS	66.37 °N	136.7 °W
CA002100500	ELSA	63.92 °N	135.48 °W
CA002100517	FARO	62.2 °N	133.367 °W
CA002100518	FARO (AUT)	62.23 °N	133.35 °W
CA002100630	HAINES JUNCTION YTG	60.767 °N	137.583 °W
CA002100631	HAINES JUNCTION YTG	60.75 °N	137.5 °W
CA002100636	HERSCHEL ISLAND	69.57 °N	138.91 °W
CA002100660	IVVAVIK NAT. PARK	69.16 °N	140.15 °W
CA002100670	JOHNSONS CROSSING	60.48 °N	133.3 °W
CA002100677	KENO HILL	63.93 °N	135.2 °W
CA002100679	KLONDIKE	64.45 °N	138.217 °W
CA002100680	KLUANE LAKE	61.02 °N	138.4 °W
CA002100685	KOMAKUK BEACH ARPT	69.583 °N	140.183 °W
CA002100693	MACMILLAN PASS	63.24 °N	130.04 °W
CA002100697	MARGARET LAKE	68.8 °N	140.85 °W
CA002100698	MARSH LAKE	60.43 °N	134.25 °W
CA002100700	MAYO AIRPORT	63.617 °N	135.867 °W
CA002100709	MAYO ROAD	60.87 °N	135.18 °W
CA002100719	MCQUESTEN	63.6 °N	137.52 °W
CA002100794	OGILVIE RIVER	65.35 °N	138.32 °W
CA002100800	OLD CROW AIRPORT	67.567 °N	139.833 °W
CA002100840	OTTER FALLS NCPC	61.03 °N	137.05 °W
CA002100880	PELLY RANCH	62.82 °N	137.37 °W
CA002100907	PORTER CREEK WAHL	60.77 °N	135.12 °W

APPENDIX A. Continued.

CA002100940	ROSS RIVER AIRPORT	61.967 °N	132.433 °W
CA002100941	ROSS RIVER YTG	61.98 °N	132.45 °W
CA002100950	SHINGLE POINT ARPT	68.95 °N	137.217 °W
CA002100FCG	HOUR LAKE	61.18 °N	129.13 °W
CA002100LRP	DAWSON	64.05 °N	139.13 °W
CA002101030	STEWART CROSSING	63.38 °N	136.68 °W
CA002101033	STEWART RIVER	63.32 °N	139.43 °W
CA002101081	SWIFT RIVER YUKON TERRI	60 °N	131.183 °W
CA002101095	TAKHINI RIVER RANCH	60.85 °N	135.57 °W
CA002101100	TESLIN ARPT (AUT)	60.167 °N	132.75 °W
CA002101102	TESLIN (AUT)	60.17 °N	132.73 °W
CA002101135	TUCHITUA	60.917 °N	129.25 °W
CA002101200	WATSON LAKE AIRPORT	60.117 °N	128.817 °W
CA002101300	WHITEHORSE AIRPORT	60.717 °N	135.067 °W
CA002101400	WHITEHORSE RIVERDALE	60.72 °N	135.02 °W
CA002200100	AKLAVIK	68.217 °N	135 °W
CA002200675	CAPE PARRY AIRPORT	70.167 °N	124.683 °W
CA002200824	COLVILLE LAKE	67.04 °N	126.08 °W
CA002201022	DELINE CS	65.22 °N	123.43 °W
CA0022010H0	DEADMEN VALLEY	61.26 °N	124.47 °W
CA0022010KA	DELINE A	65.17 °N	123.42 °W
CA002201400	FORT GOOD HOPE CS	66.233 °N	128.65 °W
CA002201450	FORT GOOD HOPE CS	66.23 °N	128.65 °W
CA002201575	FORT LIARD	60.233 °N	123.467 °W
CA002201579	FORT LIARD	60.23 °N	123.47 °W
CA002201601	FORT MCPHERSON	67.4 °N	134.85 °W
CA002201700	TULITA	64.92 °N	125.57 °W
CA002201799	FORT PROVIDENCE	61.32 °N	117.6 °W
CA002201800	FT PROVIDENCE	61.333 °N	117.667 °W
CA002201900	FORT RELIANCE	62.717 °N	109.167 °W
CA002201903	FORT RELIANCE (AUT)	62.71 °N	109.17 °W
CA002202000	FORT RESOLUTION	61.183 °N	113.683 °W
CA002202100	FORT SIMPSON	61.87 °N	121.35 °W
CA002202102	FORT SIMPSON CLIMATE	61.76 °N	121.24 °W
CA002202196	FORT SMITH AIRPORT	60.017 °N	111.967 °W
CA002202200	FORT SMITH AIRPORT	60.017 °N	111.967 °W
CA002202202	FORT SMITH CLIMATE	60.03 °N	111.93 °W
CA002202351	HANBURY RIVER	63.6 °N	105.13 °W
CA002202400	HAY RIVER AIRPORT	60.833 °N	115.783 °W
CA002202402	HAY RIVER CLIMATE	60.84 °N	115.78 °W

APPENDIX A. Continued.

CA002202405	HAY RIVER PARADISE GDNS	60.65 °N	116 °W
CA002202560	INNER WHALEBACKS	61.92 °N	113.73 °W
CA002202570	INUVIK AIRPORT	68.3 °N	133.483 °W
CA002202575	INUVIK AWOS A	68.3 °N	133.48 °W
CA002202578	INUVIK CLIMATE	68.32 °N	133.52 °W
CA002202582	INUVIK UA	68.32 °N	133.52 °W
CA002202663	KEATS POINT	69.67 °N	121.67 °W
CA002202678	LAC LA MARTRE	63.133 °N	117.25 °W
CA002202800	NORMAN WELLS ARPT	65.283 °N	126.8 °W
CA002202810	NORMAN WELLS CLIMATE	65.28 °N	126.75 °W
CA002203057	PAULATUK (AUTO)	69.35 °N	124.05 °W
CA002203058	PAULATUK	69.36 °N	124.08 °W
CA002203095	PELLY ISLAND	69.63 °N	135.44 °W
CA002203101	PINE POINT	60.87 °N	114.37 °W
CA002203341	QAVVIK LAKE	68.25 °N	122.1 °W
CA002203342	RABBIT KETTLE	61.96 °N	127.21 °W
CA002203359	RAE LAKES	64.11 °N	117.33 °W
CA002203361	GAMETI AIRPORT	64.12 °N	117.31 °W
CA002203700	SNARE RAPIDS	63.52 °N	116 °W
CA002203891	TSICHU RIVER	63.3 °N	129.82 °W
CA002203910	TUKTOYAKTUK	69.45 °N	133 °W
CA002203912	TUKTOYAKTUK	69.433 °N	133.033 °W
CA002203914	TUKTOYAKTUK	69.43 °N	133.02 °W
CA002203918	TUKTUT NOGAI	69.2 °N	122.36 °W
CA002203922	TUNGSTEN	61.95 °N	128.25 °W
CA002203943	VIRGINIA FALLS	61.63 °N	125.8 °W
CA002204000	WRIGLEY	63.2 °N	123.433 °W
CA002204100	YELLOWKNIFE AIRPORT	62.467 °N	114.45 °W
CA002204155	YELLOWKNIFE CS	62.47 °N	114.45 °W
CA002204200	YELLOWKNIFE HYDRO	62.67 °N	114.25 °W
CA002204300	YOHIN	61.24 °N	123.74 °W
CA00220B68C	LIVERPOOL BAY	69.6 °N	130.91 °W
CA00220B6Q3	LITTLE CHICAGO	67.2 °N	130.217 °W
CA00220BFH3	LITTLE DOCTOR LAKE	61.9 °N	123.25 °W
CA00220CQHR	TROUT LAKE	60.44 °N	121.24 °W
CA00220L001	LUTSELK'E A	62.42 °N	110.68 °W
CA00220L002	LUTSELK'E CS	62.42 °N	110.67 °W
CA00220N001	EKATI A	64.7 °N	110.61 °W
CA00220N003	LINDBURG LANDING	61.13 °N	122.85 °W
CA00220N004	LOWER CARP LAKE	63.6 °N	113.86 °W

APPENDIX A. Continued.

CA00220N005	TRAIL VALLEY	68.75 °N	133.5 °W
CA002300500	BAKER LAKE AIRPORT	64.3 °N	96.067 °W
CA002300501	BAKER LAKE CLIMATE	64.32 °N	96 °W
CA002300700	CHESTERFIELD	63.33 °N	90.72 °W
CA002300707	CHESTERFIELD INLET	63.333 °N	90.717 °W
CA002300750	CLINTON POINT	69.583 °N	120.75 °W
CA002300850	CONTWOYTO LAKE	65.48 °N	110.37 °W
CA002300900	COPPERMINE AIRPORT	67.833 °N	115.117 °W
CA002300902	KUGLUKTUK A	67.82 °N	115.13 °W
CA002300904	KUGLUKTUK CLIMATE	67.82 °N	115.14 °W
CA002300MKF	ARVIAT AIRPORT	61.1 °N	94.067 °W
CA002301000	CORAL HARBOUR ARPT	64.2 °N	83.367 °W
CA002301100	ENNADAI LAKE	61.133 °N	100.9 °W
CA002301102	ENNADAI LAKE (AUT)	61.13 °N	100.88 °W
CA002301153	ARVIAT CLIMATE	61.1 °N	94.07 °W
CA002301331	BROWN RIVER	66.03 °N	91.83 °W
CA002302335	GJOA HAVEN	68.633 °N	95.85 °W
CA002302340	GJOA HAVEN CLIMATE	68.64 °N	95.85 °W
CA002302370	HAT ISLAND	68.32 °N	100.09 °W
CA002302650	JENNY LIND ISL ARPT	68.65 °N	101.733 °W
CA002302680	LADY FRANKLIN POINT	68.5 °N	113.217 °W
CA002303090	PELLY BAY	68.433 °N	89.717 °W
CA002303092	KUGAARUK A	68.53 °N	89.8 °W
CA002303093	CAM FOUR	68.44 °N	89.73 °W
CA002303401	RANKIN INLET A	62.817 °N	92.117 °W
CA002303610	ROBERTSON LAKE (AUT)	65.1 °N	102.43 °W
CA002303685	SHEPHERD BAY ARPT	68.817 °N	93.433 °W
CA002303985	WHALE COVE	62.18 °N	92.6 °W
CA002303986	WHALE COVE AIRPORT	62.233 °N	92.6 °W
CA002304058	YATHKYED LAKE (AUT)	62.71 °N	98.29 °W
CA00230J01Q	CROKER RIVER	69.28 °N	119.22 °W
CA00230J048	DUBAWNT LAKE (AUT)	63.23 °N	101.76 °W
CA00230N002	LUPIN CS	65.76 °N	111.25 °W
CA002400300	ALERT	82.517 °N	62.283 °W
CA002400305	ALERT CLIMATE	82.5 °N	62.33 °W
CA002400306	ALERT UA	82.5 °N	62.33 °W
CA002400404	ARCTIC BAY CS	72.99 °N	85.01 °W
CA002400565	BREVOORT ISLAND	63.333 °N	64.15 °W
CA002400570	FOX FIVE	67.53 °N	63.78 °W
CA002400572	QIKIQTARJUAQ A	67.55 °N	64.03 °W

APPENDIX A. Continued.

CA002400573	QIKIQTARJUAQ CLIMATE	67.55 °N	64.03 °W
CA002400595	BYRON BAY AIRPORT	68.75 °N	109.067 °W
CA002400600	CAMBRIDGE BAY AIRPORT	69.1 °N	105.117 °W
CA002400602	CAMBRIDGE BAY GSN	69.11 °N	105.14 °W
CA002400635	CAPE DORSET AIRPORT	64.233 °N	76.533 °W
CA002400636	CAPE	64.23 °N	76.53 °W
CA002400654	CAPE	66.583 °N	61.617 °W
CA002400660	CAPE	68.47 °N	66.82 °W
CA002400800	CYLDE	70.483 °N	68.517 °W
CA002400802	CLYDE	70.48 °N	68.52 °W
CA002400F63	CAPE	64.96 °N	63.58 °W
CA002401030	DEWAR	68.65 °N	71.17 °W
CA002401200	EUREKA	79.983 °N	85.933 °W
CA002402340	GLADMAN	68.667 °N	97.8 °W
CA002402346	GRISE	76.417 °N	82.9 °W
CA002402350	HALL	68.783 °N	81.25 °W
CA002402353	HALL	68.78 °N	81.24 °W
CA002402540	IGLOOLIK	69.38 °N	81.8 °W
CA002402543	IGLOOLIK	69.367 °N	81.817 °W
CA002402590	IQALUIT	63.75 °N	68.55 °W
CA002402592	IQALUIT	63.75 °N	68.55 °W
CA002402594	IQALUIT	63.75 °N	68.55 °W
CA002402604	ISACHSEN	78.79 °N	103.55 °W
CA002402684	LONGSTAFF	68.883 °N	75.133 °W
CA002402686	MACKAR	68.3 °N	85.667 °W
CA002402730	NANISIVIK	72.983 °N	84.6 °W
CA002403049	PANGNIRTUNG	66.133 °N	65.7 °W
CA002403050	PANGNIRTUNG	66.15 °N	65.717 °W
CA002403053	PANGNIRTUNG	66.13 °N	65.7 °W
CA002403201	POND	72.7 °N	77.97 °W
CA002403204	POND	72.68 °N	77.98 °W
CA002403450	REA	75.37 °N	105.72 °W
CA002403490	REPULSE	66.517 °N	86.217 °W
CA002403500	RESOLUTE	74.717 °N	94.983 °W
CA002403505	RESOLUTE	74.72 °N	94.98 °W
CA002403602	RESOLUTION	61.583 °N	64.65 °W
CA002403625	ROWLEY	69.083 °N	79.033 °W
CA002403756	STEFANSSON	73.77 °N	105.29 °W
CA002403854	TALOYOAK	69.55 °N	93.58 °W
CA002403945	WAGER	65.88 °N	89.45 °W

APPENDIX A. Continued.

CA00240KFQJ	KIMMIRUT	62.85 °N	69.883 °W
CA002500440	AULAVIK	74.14 °N	119.99 °W
CA002502501	ULUKHATOK	70.75 °N	117.8 °W
CA002502505	HOLMAN	70.76 °N	117.81 °W
CA002502700	MOULD	76.233 °N	119.333 °W
CA002503648	SACHS	72 °N	125.27 °W
CA002503886	THOMSEN	73.23 °N	119.54 °W
CA00250M001	MOULD	76.24 °N	119.35 °W
FI000000304	HELSINKI	60.17 °N	24.95 °E
FI000002401	JYVASKYLA	62.4 °N	25.683 °E
FI000002963	JOKIOINEN	60.817 °N	23.5 °E
FI000007501	SODANKYLA	67.367 °N	26.65 °E
GL000004250	NUUK	64.167 °N	51.75 °W
GL000004320	DANMARKSHAVN	76.767 °N	18.667 °W
GL000004360	TASIIAQ	65.6 °N	37.633 °W
IC000004013	STYKKISHOLMUR	65.083 °N	22.733 °W
IC000004030	REYKJAVIK	64.132 °N	21.9 °W
IC000004048	VESTMANNAEYJAR	63.4 °N	20.283 °W
IC000004063	AKUREYRI	65.683 °N	18.083 °W
IC000004092	TEIGARHORN	64.68 °N	15.14 °W
IC000004097	DALATANGI	65.266 °N	13.583 °W
ICW00016201	KEFLAVIK	63.9667 °N	22.6 °W
JN000099950	JAN-MAYEN	70.93 °N	7.33 °W
NO000001026	TROMSO	69.65 °N	18.933 °E
NO000001212	ONA	62.867 °N	6.533 °E
NO000001238	FOKSTUA	62.117 °N	9.283 °E
NO000005350	NORD-ODAL	60.38 °N	11.55 °E
NO0000050350	SAMNANGER	60.46 °N	5.9 °E
NO0000050540	BERGEN/FLORIDA	60.383 °N	5.333 °E
NO0000050550	BERGEN-FREDRIKSBERG	60.4 °N	5.317 °E
NO000068330	SELBU-STUBBE	63.2 °N	11.117 °E
NO000086850	BARKESTAD	68.82 °N	14.8 °E
NO000093300	SUOLOVUOPMI	69.583 °N	23.533 °E
NO000097250	KARASJOK	69.467 °N	25.517 °E
NO000098550	VARDO	70.367 °N	31.1 °E
NO000099710	BJORNOYA	74.517 °N	19.017 °E
RS000020046	POLARGMO	80.617 °N	58.05 °E
RS000020049	RUDOLF	81.8 °N	57.97 °E
RS000020069	OSTROV	79.5 °N	76.983 °E
RS000020087	DOMASCHNIY	79.5 °N	91.13 °E

APPENDIX A. Continued.

RS000020274	OSTROV	77.5 °N	82.2 °E
RS000020292	GMO	77.717 °N	104.3 °E
RS000020353	MYS	76.85 °N	68.55 °E
RS000020357	RUSSKAJ-GAVAN'	76.2 °N	63.6 °E
RS000020594	UST'-TAYMYRA	76.2 °N	99.07 °E
RS000020667	IM.	73.333 °N	70.05 °E
RS000020674	OSTROV	73.5 °N	80.4 °E
RS000020744	MALYE	72.367 °N	52.7 °E
RS000020891	HATANGA	71.983 °N	102.467 °E
RS000020982	VOLOCHANKA	70.967 °N	94.5 °E
RS000021358	ZHOVA	76.15 °N	152.833 °E
RS000021432	OSTROV	76 °N	137.867 °E
RS000021504	OSTROV	74.667 °N	112.933 °E
RS000021636	CAPE	73.333 °N	139.917 °E
RS000021647	SHALAUROVA	73.18 °N	143.23 °E
RS000021802	SASKYLAH	71.967 °N	114.083 °E
RS000021824	TIKSI	71.583 °N	128.917 °E
RS000021908	DZALINDA	70.133 °N	113.967 °E
RS000021921	KJUSJUR	70.683 °N	127.4 °E
RS000021931	JUBILEJNAJA	70.767 °N	136.217 °E
RS000021946	CHOKURDAH	70.617 °N	147.883 °E
RS000021965	OSTROV	70.633 °N	162.483 °E
RS000021982	VRANGELYA	70.97 °N	178.53 °E
RS000022028	TERIBERKA	69.2 °N	35.117 °E
RS000022106	PADUN	68.6 °N	31.85 °E
RS000022112	KOLA-IN-MURMAN	68.883 °N	33.017 °E
RS000022113	MURMANSK	68.967 °N	33.05 °E
RS000022119	PULOSERO	68.4 °N	33.3 °E
RS000022127	LOVOZERO	68 °N	35.033 °E
RS000022145	SVYAToy	68.15 °N	39.82 °E
RS000022165	KANIN	68.65 °N	43.3 °E
RS000022212	MONCEGORSK	67.967 °N	32.883 °E
RS000022217	KANDALAKSA	67.15 °N	32.35 °E
RS000022235	KRASNOSCELE	67.35 °N	37.05 °E
RS000022269	MYS	67.15 °N	43.9 °E
RS000022271	SOJNA	67.883 °N	44.133 °E
RS000022282	MYS	67.8 °N	46.667 °E
RS000022292	INDIGA	67.683 °N	48.683 °E
RS000022312	KOVDA	66.7 °N	32.883 °E
RS000022318	LOUHI	66.067 °N	33 °E

APPENDIX A. Continued.

RS000022324	UMBA	66.683 °N	34.35 °E
RS000022349	PJALICA	66.183 °N	39.533 °E
RS000022365	ABRAMOVSKIJ	66.383 °N	43.25 °E
RS000022383	NIZHNYAYA	66.767 °N	47.783 °E
RS000022408	KALEVALA	65.217 °N	31.167 °E
RS000022422	GRIDINO	65.9 °N	34.767 °E
RS000022438	ZIZGIN	65.2 °N	36.817 °E
RS000022446	ZIMNEGORSKIJ	65.467 °N	39.733 °E
RS000022452	INCY	65.967 °N	40.717 °E
RS000022471	MEZEN	65.867 °N	44.217 °E
RS000022499	BARKOVSKAJA	65.233 °N	49.583 °E
RS000022511	JUSKOZERO	64.75 °N	32.116 °E
RS000022518	RUGOZERO	64.083 °N	32.783 °E
RS000022522	KEM	64.95 °N	34.65 °E
RS000022525	RAZNAVOLOK	64.566 °N	34.917 °E
RS000022529	KOLEZMA	64.233 °N	35.883 °E
RS000022541	UNSKIJ	64.833 °N	38.4 °E
RS000022550	ARHANGELSK	64.55 °N	40.583 °E
RS000022551	MUDJUG	64.849 °N	40.283 °E
RS000022559	HOLMOGORY	64.217 °N	41.667 °E
RS000022563	PINEGA	64.7 °N	43.383 °E
RS000022573	LESUKONSKOE	64.9 °N	45.767 °E
RS000022583	KOJNAS	64.75 °N	47.65 °E
RS000022602	REBOLY	63.833 °N	30.817 °E
RS000022619	PADANY	63.267 °N	33.417 °E
RS000022621	SEGEZA	63.767 °N	34.283 °E
RS000022641	ONEGA	63.9 °N	38.117 °E
RS000022648	TURCASOVO	63.117 °N	39.233 °E
RS000022656	EMECK	63.483 °N	41.8 °E
RS000022676	SURA	63.583 °N	45.633 °E
RS000022686	VENDINGA	63.45 °N	47.917 °E
RS000022695	KOSLAN	63.45 °N	48.9 °E
RS000022707	VYARTSILYA	62.183 °N	30.7 °E
RS000022721	MEDVEZEGORSK	62.917 °N	34.433 °E
RS000022723	DANILOVO	62.967 °N	35.7 °E
RS000022727	KONDOPOGA	62.167 °N	34.3 °E
RS000022738	KUGONAVOLOK	62.233 °N	36.883 °E
RS000022762	DVINSKIJ	62.867 °N	42.717 °E
RS000022768	SENKURSK	62.1 °N	42.9 °E
RS000022778	VERHNJAJA	62.233 °N	45.017 °E

APPENDIX A. Continued.

RS000022798	JARENSK	62.167 °N	49.117 °E
RS000022802	SORTAVALA	61.717 °N	30.717 °E
RS000022816	PRIAZA	61.683 °N	33.617 °E
RS000022820	PETROZAVODSK	61.817 °N	34.267 °E
RS000022831	PUDOZ	61.8 °N	36.517 °E
RS000022833	KOLODOZERO	61.783 °N	37.75 °E
RS000022837	VYTEGRA	61.017 °N	36.45 °E
RS000022845	KARGOPOL	61.5 °N	38.933 °E
RS000022854	NJANDOMA	61.667 °N	40.183 °E
RS000022867	VELSK	61.083 °N	42.067 °E
RS000022887	KOTLAS	61.233 °N	46.717 °E
RS000022892	VYBORG	60.717 °N	28.733 °E
RS000022907	OZERKI	60.2 °N	29 °E
RS000022912	OLONEC	60.983 °N	32.983 °E
RS000022913	LODEJNOE	60.717 °N	33.55 °E
RS000022915	SVIRICA	60.467 °N	32.9 °E
RS000022917	NOVAJA	60.117 °N	32.317 °E
RS000022925	VINNICY	60.633 °N	34.783 °E
RS000022939	BELOZERSK	60.033 °N	37.783 °E
RS000022954	VOZEGA	60.467 °N	40.2 °E
RS000022981	VELIKIJ	60.767 °N	46.3 °E
RS000022996	OBJACEVO	60.367 °N	49.65 °E
RS000023022	YUGORSKIY	69.817 °N	60.75 °E
RS000023032	MARESALE	69.717 °N	66.8 °E
RS000023074	DUDINKA	69.4 °N	86.167 °E
RS000023146	CAPE	68.467 °N	73.6 °E
RS000023205	NARJAN-MAR	67.633 °N	53.033 °E
RS000023207	KOTKINO	67.017 °N	51.2 °E
RS000023219	HOSEDA-HARD	67.083 °N	59.383 °E
RS000023226	VORKUTA	67.483 °N	64.016 °E
RS000023242	NOVY	67.683 °N	72.867 °E
RS000023256	TAZOVSKOE	67.467 °N	78.733 °E
RS000023274	IGARKA	67.433 °N	86.617 °E
RS000023305	OKUNEV	66.25 °N	52.583 °E
RS000023324	PETRUN	66.433 °N	60.767 °E
RS000023330	SALEHARD	66.533 °N	66.667 °E
RS000023331	RA-IZ	66.9 °N	65.7 °E
RS000023383	AGATA	66.883 °N	93.467 °E
RS000023405	UST-CILMA	65.433 °N	52.267 °E
RS000023412	UST-USA	65.967 °N	56.917 °E

APPENDIX A. Continued.

RS000023418	PECHORA	65.117 °N	57.1 °E
RS000023426	MUZI	65.382 °N	64.717 °E
RS000023472	SUKHAYA	65.167 °N	87.917 °E
RS000023518	UST-SUGOR	64.266 °N	57.617 °E
RS000023527	SARAN-PAUL	64.283 °N	60.883 °E
RS000023552	TARKO-SALE	64.917 °N	77.817 °E
RS000023606	UHTA	63.55 °N	53.817 °E
RS000023625	SOSVA	63.65 °N	62.1 °E
RS000023631	BEREZOVO	63.933 °N	65.05 °E
RS000023678	VERHNEIMBATSK	63.15 °N	87.95 °E
RS000023701	VESLJANA	62.9 °N	50.9 °E
RS000023711	TROICKO-PECHERSKOE	62.7 °N	56.2 °E
RS000023724	NJAKSIMVOL	62.433 °N	60.867 °E
RS000023734	OKTJABRSKOE	62.45 °N	66.05 °E
RS000023803	UST-KULOM	61.683 °N	53.683 °E
RS000023804	SYKTYVKAR	61.683 °N	50.783 °E
RS000023813	UST-UNJA	61.8 °N	57.917 °E
RS000023849	SURGUT	61.25 °N	73.5 °E
RS000023867	LAR'YAK	61.27 °N	80.05 °E
RS000023884	BOR	61.6 °N	90.2 °E
RS000023891	BAJKIT	61.667 °N	96.367 °E
RS000023909	GAJNY	60.283 °N	54.35 °E
RS000023914	CHERDYN	60.4 °N	56.517 °E
RS000023921	IVDEL,AS	60.41 °N	60.26 °E
RS000023929	SAIM	60.317 °N	64.217 °E
RS000023933	HANTY-MANSIJSK	61.017 °N	69.033 °E
RS000023955	ALEKSANDROVSKOE	60.433 °N	77.867 °E
RS000023966	VANZIL-KYNAK	60.35 °N	84.083 °E
RS000023973	VOROGOVO	61 °N	89.6 °E
RS000023975	SYM	60.35 °N	88.367 °E
RS000023982	VELMO	61.02 °N	93.42 °E
RS000023987	JARCEVO	60.25 °N	90.233 °E
RS000024105	ESSEJ	68.467 °N	102.367 °E
RS000024125	OLENEK	68.5 °N	112.433 °E
RS000024136	SUHANA	68.617 °N	118.333 °E
RS000024143	DZARDZAN	68.733 °N	124 °E
RS000024197	DRUZINA	68.233 °N	145.3 °E
RS000024266	VERHOJANSK	67.55 °N	133.383 °E
RS000024329	SELAGONCY	66.25 °N	114.283 °E
RS000024343	ZHIGANSK	66.767 °N	123.4 °E

APPENDIX A. Continued.

RS000024382	UST-MOMA	66.45 °N	143.233 °E
RS000024477	IEMA	65.3 °N	135.67 °E
RS000024507	TURA	64.17 °N	100.07 °E
RS000024561	SYURYUN-KYUYEL	65 °N	130.683 °E
RS000024585	UST-NERA	64.566 °N	143.2 °E
RS000024598	DARPIR	64.167 °N	148.033 °E
RS000024639	NJURBA	63.283 °N	118.333 °E
RS000024641	VILJUJSK	63.767 °N	121.617 °E
RS000024652	SANGARY	63.967 °N	127.467 °E
RS000024656	BATAMAJ	63.517 °N	129.483 °E
RS000024671	TOMPO	63.95 °N	135.867 °E
RS000024678	ZAPADNAYA	63.13 °N	138.28 °E
RS000024688	OJMJAKON	63.25 °N	143.15 °E
RS000024724	CHERNISHEVSKII	63 °N	112.3 °E
RS000024725	TUOY-KHAYA	62.53 °N	111.23 °E
RS000024738	SUNTAR	62.15 °N	117.65 °E
RS000024763	KREST-KHALDZHAY	62.82 °N	134.43 °E
RS000024768	CURAPCA	62.033 °N	132.6 °E
RS000024817	ERBOGACEN	61.267 °N	108.017 °E
RS000024856	POKROVSKAJA	61.483 °N	129.15 °E
RS000024891	KULU	61.883 °N	147.35 °E
RS000024908	VANAVARA	60.333 °N	102.267 °E
RS000024918	PREOBRAZENKA	60.067 °N	107.967 °E
RS000024923	LENSK	60.717 °N	114.883 °E
RS000024944	OLEKMINSK	60.4 °N	120.417 °E
RS000024951	ISIT	60.817 °N	125.317 °E
RS000024959	JAKUTSK	62.017 °N	129.717 °E
RS000024962	AMGA	60.9 °N	131.983 °E
RS000024966	UST-MAJA	60.383 °N	134.45 °E
RS000024982	UEGA	60.717 °N	142.783 °E
RS000024988	ARKA	60.083 °N	142.333 °E
RS000025034	BUHTA	69.617 °N	162.3 °E
RS000025123	CHERSKIJ	68.75 °N	161.283 °E
RS000025173	MYS	68.9 °N	179.367 °W
RS000025206	CREDNEKOLYMSK	67.45 °N	153.717 °E
RS000025248	ILIRNEY	67.33 °N	168.23 °E
RS000025325	UST-OLOJ	66.55 °N	159.417 °E
RS000025372	AMGUJEMA	67.033 °N	178.917 °W
RS000025378	EGVEKINOT	66.35 °N	179.117 °W
RS000025392	ENURMINO	66.933 °N	171.833 °W

APPENDIX A. Continued.

RS000025399	MYS	66.15 °N	169.833 °W
RS000025400	ZYRJANKA	65.733 °N	150.9 °E
RS000025428	OMOLON	65.233 °N	160.533 °E
RS000025503	KORKODON	64.75 °N	153.967 °E
RS000025526	KEGALI	64.25 °N	161.07 °E
RS000025538	VERKHNE-PENZHINO	64.22 °N	164.23 °E
RS000025551	MARKOVO	64.683 °N	170.417 °E
RS000025563	ANADYR	64.783 °N	177.567 °E
RS000025594	BUHTA	64.266 °N	173.3 °W
RS000025621	KEDON	64 °N	158.917 °E
RS000025656	BEREZOVO	63.417 °N	172.717 °E
RS000025677	BERINGOVSKAJA	63.017 °N	179.283 °E
RS000025703	SEJMCHAN	62.917 °N	152.417 °E
RS000025705	SREDNIKAN	62.45 °N	152.317 °E
RS000025715	OMSUKCHAN	62.5 °N	155.783 °E
RS000025744	KAMENSKOE	62.5 °N	166.2 °E
RS000025777	BUHTA	62.417 °N	179.133 °E
RS000025802	STRELKA	61.87 °N	152.22 °E
RS000025821	NAJAHAN	61.95 °N	158.967 °E
RS000025822	GIZIGA	61.95 °N	160.367 °E
RS000025902	ATKA	60.75 °N	151.77 °E
RS000025954	KORF	60.35 °N	166 °E
RS000025956	APUKA	60.4 °N	169.7 °E
SV000001008	SVALBARD	78.25 °N	15.467 °E
SV000020107	BARENCEBURG	78.067 °N	14.25 °E
SW000002080	KARESUANDO	68.45 °N	22.45 °E
SW000002120	KVIKKJOKK-ARRENJARK	66.883 °N	17.75 °E
SW000002127	STENSELE	65.067 °N	17.167 °E
SW000002196	HAPARANDA	65.833 °N	24.15 °E
SW000002288	HOLMOGADD	63.6 °N	20.75 °E
SW000002361	HARNOSAND	62.633 °N	17.95 °E
SW000002410	MALUNG	60.683 °N	13.717 °E
SW000010537	FALUN	60.617 °N	15.667 °E
UK000003005	LERWICK	60.133 °N	1.183 °W
US1AKAB0001	ANCHORAGE	61.2047 °N	149.7563 °W
US1AKAB0003	ANCHORAGE	61.1926 °N	149.7542 °W
US1AKAB0004	ANCHORAGE	61.1094 °N	149.7701 °W
US1AKAB0006	ANCHORAGE	61.1934 °N	149.9682 °W
US1AKAB0007	ANCHORAGE	61.1 °N	149.82 °W
US1AKAB0008	KNIK	61.4176 °N	149.4477 °W

APPENDIX A. Continued.

US1AKAB0009	ANCHORAGE	61.1852 °N	149.7205 °W
US1AKAB0012	ANCHORAGE	60.9512 °N	149.1278 °W
US1AKAB0014	ANCHORAGE	61.1606 °N	149.8067 °W
US1AKAB0021	EAGLE	61.3122 °N	149.4958 °W
US1AKAB0022	EAGLE	61.2869 °N	149.3945 °W
US1AKAB0023	EAGLE	61.2378 °N	149.4543 °W
US1AKAB0027	ANCHORAGE	61.1039 °N	149.7296 °W
US1AKAB0028	ANCHORAGE	61.0614 °N	149.7524 °W
US1AKAB0030	ANCHORAGE	61.2059 °N	149.8112 °W
US1AKAB0034	EAGLE	61.3659 °N	149.5501 °W
US1AKAB0036	ANCHORAGE	61.1925 °N	149.76 °W
US1AKAB0038	EAGLE	61.2272 °N	149.4401 °W
US1AKAB0043	EAGLE	61.235 °N	149.2715 °W
US1AKBC0003	ANIAK	61.58 °N	159.551 °W
US1AKBC0004	SLEETMUTE	61.7025 °N	157.1699 °W
US1AKFN0004	FAIRBANKS	64.9347 °N	148.0244 °W
US1AKKP0001	SOLDOTNA	60.4868 °N	151.0823 °W
US1AKKP0002	SOLDOTNA	60.4879 °N	150.726 °W
US1AKMS0005	WILLOW	61.6995 °N	149.9897 °W
US1AKMS0010	WASILLA	61.5419 °N	149.4133 °W
US1AKVC0005	VALDEZ	61.0958 °N	146.1967 °W
US1AKWH0003	CHEVAK	61.5277 °N	165.5787 °W
US1AKWH0005	NEWTOK	60.9445 °N	164.6441 °W
USC00500172	ALASKA	61.1889 °N	149.8056 °W
USC00500230	ALLAKAKET	66.5653 °N	152.6425 °W
USC00500243	ALYESKA	60.9583 °N	149.1108 °W
USC00500247	AMBER	62.1925 °N	150.495 °W
USC00500249	AMBLER	67.0833 °N	157.85 °W
USC00500260	AMBLER	67.0833 °N	157.8667 °W
USC00500272	ANCHORAGE	61.1747 °N	149.905 °W
USC00500275	ANCHORAGE	61.1561 °N	149.9847 °W
USC00500279	ANCHORAGE	61.1167 °N	149.7333 °W
USC00500281	ANCHORAGE	61.1025 °N	149.7169 °W
USC00500284	ANCHORAGE	61.0883 °N	149.7561 °W
USC00500286	ANCHORAGE	61.1939 °N	149.8858 °W
USC00500287	ANCHORAGE	61.2044 °N	149.9106 °W
USC00500299	ANDERSON	64.3458 °N	149.1947 °W
USC00500302	ANDERSON	61.6244 °N	149.3397 °W
USC00500396	ARCTIC	68.1167 °N	145.5333 °W
USC00500490	AURORA	64.8553 °N	147.7217 °W

APPENDIX A. Continued.

USC00500653	BEAVER	66.3597 °N	147.4014 °W
USC00500685	BELUGA	61.1833 °N	151.0333 °W
USC00500707	BENS	61.5678 °N	149.1386 °W
USC00500788	BIG	60.8142 °N	152.297 °W
USC00501175	BUTTE	61.5836 °N	149.0056 °W
USC00501180	BUTTE	61.52 °N	149.0561 °W
USC00501220	CAMPBELL	61.1639 °N	149.7778 °W
USC00501228	CAMP	61.495 °N	149.7572 °W
USC00501230	CANDLE	65.9333 °N	161.9167 °W
USC00501240	CANNERY	61.0183 °N	147.5147 °W
USC00501243	CANTWELL	63.3953 °N	148.895 °W
USC00501244	CANTWELL	63.3717 °N	148.8433 °W
USC00501312	CAPE	68.8667 °N	166.1167 °W
USC00501318	CAPE	61.7667 °N	166.05 °W
USC00501451	CASWELL	61.9736 °N	150.0594 °W
USC00501466	CENTRAL	65.5667 °N	144.7653 °W
USC00501492	CHANDALAR	67.5111 °N	148.4925 °W
USC00501497	CHANDALAR	68.0781 °N	149.5647 °W
USC00501557	CHENA	64.8203 °N	147.9805 °W
USC00501574	CHENA	65.0528 °N	146.0561 °W
USC00501684	CHICKEN	64.0917 °N	141.9211 °W
USC00501821	CHISTOCHINA	62.6125 °N	144.6156 °W
USC00501824	CHITINA	61.5231 °N	144.4089 °W
USC00501900	CHULITNA	62.4 °N	150.25 °W
USC00501926	CHULITNA	62.8256 °N	149.9061 °W
USC00501977	CIRCLE	65.8333 °N	144.0667 °W
USC00501987	CIRCLE	65.4861 °N	144.6364 °W
USC00502005	CLEAR	64.3547 °N	149.0436 °W
USC00502015	CLEAR	64.2453 °N	149.1828 °W
USC00502019	CLEARWATER	64.05 °N	145.5167 °W
USC00502101	O'BRIEN	64.3172 °N	141.4183 °W
USC00502104	COLDFOOT	67.2539 °N	150.1875 °W
USC00502107	COLLEGE	64.8603 °N	147.8483 °W
USC00502110	COLLEGE	64.8922 °N	147.8453 °W
USC00502112	COLLEGE	64.925 °N	147.8803 °W
USC00502114	COLLEGE	64.8264 °N	147.9589 °W
USC00502126	COLVILLE	70.4322 °N	150.4094 °W
USC00502144	COOPER	60.3925 °N	149.6661 °W
USC00502149	COOPER	60.4875 °N	149.968 °W
USC00502156	COPPER	61.9667 °N	145.3167 °W

APPENDIX A. Continued.

USC00502173	CORDOVA	60.5561 °N	145.7531 °W
USC00502179	CORDOVA	60.5358 °N	145.778 °W
USC00502241	CRESTLINE	64.9239 °N	147.665 °W
USC00502339	DELTA	64.1172 °N	145.7511 °W
USC00502341	DELTA	63.9333 °N	145.3419 °W
USC00502350	DELTA	64.0839 °N	145.6136 °W
USC00502352	DELTA	63.9639 °N	145.1044 °W
USC00502568	DRY	63.6772 °N	144.6011 °W
USC00502642	EAGLE	61.2344 °N	149.2708 °W
USC00502645	EAGLE	61.3192 °N	149.5436 °W
USC00502648	EAGLE	61.2225 °N	149.4386 °W
USC00502656	EAGLE	61.2969 °N	149.44 °W
USC00502665	EDGEMIRE	62.5333 °N	150.2833 °W
USC00502707	EIELSON	64.6667 °N	147.1 °W
USC00502711	EIELSON	63.4258 °N	150.3117 °W
USC00502730	EKLUTNA	61.4667 °N	149.1667 °W
USC00502737	EKLUTNA	61.4494 °N	149.3231 °W
USC00502825	EMMONAK	62.7833 °N	164.4833 °W
USC00502868	ESTER	64.8758 °N	148.0439 °W
USC00502870	ESTER	64.8464 °N	148.0256 °W
USC00502871	ESTER	64.9111 °N	147.9242 °W
USC00502872	ESTER	64.7919 °N	148.0367 °W
USC00502873	ESTER	64.9133 °N	147.9139 °W
USC00502876	ESTER	64.7694 °N	148.0464 °W
USC00502964	FAIRBANKS	65.1178 °N	147.6856 °W
USC00502965	FAIRBANKS	64.8172 °N	147.8739 °W
USC00502970	FAIRBANKS	64.8342 °N	147.7911 °W
USC00503009	FAREWELL	62.5422 °N	153.6206 °W
USC00503082	FIVE	65.9333 °N	149.8333 °W
USC00503083	FLAG	64.4078 °N	146.9486 °W
USC00503160	FT	65.0033 °N	147.3408 °W
USC00503163	FT	61.2275 °N	149.6503 °W
USC00503181	FOX	64.9592 °N	147.6261 °W
USC00503183	FOX	64.9328 °N	147.5583 °W
USC00503196	FUNNY	60.4822 °N	150.8056 °W
USC00503205	GAKONA	62.3 °N	145.3 °W
USC00503208	GAKONA	62.3914 °N	145.1325 °W
USC00503210	GALBRAITH	68.4833 °N	149.4833 °W
USC00503212	GALENA	64.7408 °N	156.8756 °W
USC00503275	GILMORE	64.9669 °N	147.5136 °W

APPENDIX A. Continued.

USC00503299	GLEN	61.1 °N	149.6936 °W
USC00503304	GLENNALLEN	62.1086 °N	145.5328 °W
USC00503367	GOLDSTREAM	64.9261 °N	147.8767 °W
USC00503573	HAYES	61.9872 °N	152.0758 °W
USC00503581	HEALY	63.8453 °N	148.9436 °W
USC00503585	HEALY	63.8717 °N	149.0169 °W
USC00503720	HOPE	60.8983 °N	149.6286 °W
USC00503731	HOUSTON	61.6311 °N	149.8019 °W
USC00503871	IGLOO	63.1639 °N	149.7778 °W
USC00503908	ILLINOIS	64.05 °N	157.8333 °W
USC00503910	INDIAN	65.9833 °N	153.6833 °W
USC00504165	KALTAG	64.3333 °N	158.7167 °W
USC00504425	KASILOF	60.3667 °N	151.3833 °W
USC00504550	KENAI	60.6692 °N	151.3228 °W
USC00504567	KENNY	61.6794 °N	144.7639 °W
USC00504621	KEYSTONE	64.9156 °N	148.2711 °W
USC00504683	KILLIK	68.45 °N	154.3 °W
USC00504971	KOBE	64.1942 °N	149.4314 °W
USC00505051	KOTZEBUE	67.25 °N	162.8 °W
USC00505091	KOYUK	64.9333 °N	161.15 °W
USC00505136	KUPARUK	70.3167 °N	149.5833 °W
USC00505397	LAKE	62.4528 °N	146.6789 °W
USC00505454	LATOUCHE	60.05 °N	147.9 °W
USC00505464	LAZY	61.6294 °N	149.0297 °W
USC00505511	LITTLE	64.8872 °N	147.3203 °W
USC00505512	LITTLE	64.8944 °N	147.3411 °W
USC00505516	LITTLE	64.8833 °N	147.25 °W
USC00505534	LIVENGOOD	65.5225 °N	148.5497 °W
USC00505544	LONELY	70.9167 °N	153.25 °W
USC00505604	MAIN	60.5181 °N	148.093 °W
USC00505607	MANKOMEN	62.9861 °N	144.4792 °W
USC00505644	MANLEY	65 °N	150.65 °W
USC00505733	MATANUSKA	61.5664 °N	149.2542 °W
USC00505754	MC	61.4333 °N	142.9 °W
USC00505757	MCCARTHY	61.4181 °N	142.9961 °W
USC00505778	MCKINLEY	63.7175 °N	148.9692 °W
USC00505780	MEADOW	61.5778 °N	149.565 °W
USC00505845	MEKORYUK	60.3833 °N	166.2 °W
USC00505857	MENTASTA	62.9331 °N	145.5742 °W
USC00505873	MILE	65.1906 °N	147.2542 °W

APPENDIX A. Continued.

USC00505875	MILE	65.5167 °N	145.3333 °W
USC00505880	MILE	65.2222 °N	147.1667 °W
USC00505882	MINERAL	62.945 °N	143.3783 °W
USC00505883	MIRROR	61.4253 °N	149.4075 °W
USC00505888	MONTANA	62.1044 °N	150.0589 °W
USC00505889	MONTANA	65.36 °N	146.0864 °W
USC00505891	MOOSE	64.7136 °N	147.1581 °W
USC00505894	MOOSE	60.5028 °N	149.4264 °W
USC00505895	MOOSE	60.5333 °N	149.5167 °W
USC00506147	NABESNA	62.3978 °N	142.9967 °W
USC00506157	NANCY	61.6831 °N	149.975 °W
USC00506270	NELCHINA	61.9833 °N	146.8667 °W
USC00506419	NIKOLAI	63.0181 °N	154.3639 °W
USC00506463	NOATAK	67.5756 °N	162.9697 °W
USC00506581	NORTH	64.7581 °N	147.3253 °W
USC00506656	NULATO	64.7186 °N	158.1022 °W
USC00506777	OLD	61.8 °N	144.9833 °W
USC00506870	PALMER	61.4222 °N	149.0994 °W
USC00507097	PAXSON	63.0322 °N	145.4983 °W
USC00507108	PEARL	64.8922 °N	147.7961 °W
USC00507352	PLANT	61.5333 °N	149.0833 °W
USC00507431	POINT	68.35 °N	166.8 °W
USC00507444	POINT	61.4169 °N	150.0819 °W
USC00507494	PORTAGE	60.8167 °N	148.9833 °W
USC00507502	PORTAGE	60.7833 °N	148.8333 °W
USC00507513	PORT	62.6211 °N	141.0078 °W
USC00507570	PORT	60.2033 °N	154.3164 °W
USC00507669	PORT	65.25 °N	166.8667 °W
USC00507738	PORT	60.0503 °N	148.0672 °W
USC00507778	PROSPECT	66.8236 °N	150.6689 °W
USC00507780	PRUDHOE	70.25 °N	148.3333 °W
USC00507783	PUNTILLA	62.0911 °N	152.735 °W
USC00507989	RIKAS	64.15 °N	145.85 °W
USC00508025	ROCK	61.1167 °N	149.75 °W
USC00508044	RUBY	64.7425 °N	155.4842 °W
USC00508047	RUBY	64.8694 °N	155.1178 °W
USC00508054	RUSSIAN	61.7833 °N	161.3167 °W
USC00508105	ST	62.0528 °N	163.1711 °W
USC00508107	ST	62.0667 °N	163.3 °W
USC00508130	SAG	68.7608 °N	148.8731 °W

APPENDIX A. Continued.

USC00508140	SALCHA	64.4942 °N	146.9767 °W
USC00508156	SALCHA	64.5247 °N	146.3703 °W
USC00508239	SAVOONGA	63.6936 °N	170.4808 °W
USC00508375	SEWARD	60.1883 °N	149.6275 °W
USC00508377	SEWARD	60.3539 °N	149.3483 °W
USC00508379	SHAGELUK	62.7 °N	159.5667 °W
USC00508409	SHEEP	61.8125 °N	147.4992 °W
USC00508466	SILVER	64.8981 °N	147.5942 °W
USC00508470	SILVER	61.5175 °N	144.1914 °W
USC00508547	SLANA	62.7089 °N	143.9808 °W
USC00508594	SNOWSHOE	62.0303 °N	146.6931 °W
USC00508615	SOLDOTNA	60.4194 °N	151.1336 °W
USC00508618	SOLOMON	64.5833 °N	164.4 °W
USC00508625	SOURDOUGH	62.5333 °N	145.5167 °W
USC00508666	SPARREVOHN	61.1 °N	155.55 °W
USC00508813	SUMMIT	63.1483 °N	145.5408 °W
USC00508884	SUSITNA	61.9128 °N	150.0989 °W
USC00508915	SUTTON	61.7139 °N	148.9092 °W
USC00508945	TAHNETA	61.8167 °N	147.55 °W
USC00509038	TATALINA	65.3844 °N	148.2486 °W
USC00509098	TELIDA	63.3961 °N	153.2706 °W
USC00509102	TELLER	65.2608 °N	166.3595 °W
USC00509313	TOK	63.3519 °N	143.0422 °W
USC00509314	TOK	63.3156 °N	143.0058 °W
USC00509315	TOK	63.3283 °N	142.9972 °W
USC00509316	TOK	63.3269 °N	142.9956 °W
USC00509385	TONSINA	61.6503 °N	145.1714 °W
USC00509398	TRAPPER	62.2622 °N	150.4228 °W
USC00509402	TRAPPER	62.3339 °N	150.5378 °W
USC00509421	TRI	60.55 °N	150.5333 °W
USC00509489	TWO	64.8656 °N	146.9542 °W
USC00509641	UNIVERSITY	64.8564 °N	147.8617 °W
USC00509685	VALDEZ	61.1314 °N	146.2433 °W
USC00509690	VALDEZ	61.1119 °N	145.7892 °W
USC00509693	VENETIE	67.0178 °N	146.4325 °W
USC00509747	WALLY	60.7986 °N	148.0872 °W
USC00509759	WASILLA	61.5333 °N	149.4333 °W
USC00509765	WASILLA	61.6167 °N	149.4 °W
USC00509767	WASILLA	61.6508 °N	149.4192 °W
USC00509790	WHITES	61.7067 °N	149.9978 °W

APPENDIX A. Continued.

USC00509793	WHITESTONE	64.1539 °N	145.8894 °W
USC00509798	WHITE	64.6833 °N	163.4 °W
USC00509829	WHITTIER	60.7764 °N	148.6858 °W
USC00509860	WILLOW	61.7064 °N	150.1139 °W
USC00509861	WILLOW	61.7481 °N	150.0542 °W
USC00509864	WILLOW	61.7667 °N	150.05 °W
USC00509869	WISEMAN	67.4192 °N	150.1069 °W
USC00509891	WOODSMOKE	64.7803 °N	147.275 °W
USC00509911	WORTMAN'S	61.1167 °N	145.8167 °W
USW00025331	PALMER	61.5961 °N	149.0917 °W
USW00026401	ELMENDORF	61.25 °N	149.8 °W
USW00026409	ANCHORAGE	61.2167 °N	149.8333 °W
USW00026410	CORDOVA	60.4914 °N	145.4511 °W
USW00026411	FAIRBANKS	64.8039 °N	147.8761 °W
USW00026412	NORTHWAY	62.9614 °N	141.9292 °W
USW00026413	FT	66.5706 °N	145.2342 °W
USW00026415	BIG	63.995 °N	145.7183 °W
USW00026422	EAGLE	64.7856 °N	141.2036 °W
USW00026425	GULKANA	62.1603 °N	145.4569 °W
USW00026435	NENANA	64.5461 °N	149.0961 °W
USW00026438	SEWARD	60.1039 °N	149.4439 °W
USW00026440	TANACROSS	63.3783 °N	143.3483 °W
USW00026442	VALDEZ	61.1303 °N	146.3517 °W
USW00026445	YAKATAGA	60.0833 °N	142.5 °W
USW00026451	ANCHORAGE	61.1689 °N	150.0278 °W
USW00026491	ANCHORAGE	61.1781 °N	149.9664 °W
USW00026492	PORTAGE	60.785 °N	148.8389 °W
USW00026494	FAIRBANKS	64.9736 °N	147.51 °W
USW00026502	KALTAG	64.3267 °N	158.7417 °W
USW00026508	UMIAT	69.3694 °N	152.14 °W
USW00026510	MCGRATH	62.9575 °N	155.6103 °W
USW00026512	MINCHUMINA	63.9033 °N	152.2817 °W
USW00026514	SKWENTNA	61.9772 °N	151.2169 °W
USW00026516	ANIAK	61.5833 °N	159.5333 °W
USW00026519	FAREWELL	62.5167 °N	153.8833 °W
USW00026523	KENAI	60.5797 °N	151.2392 °W
USW00026528	TALKEETNA	62.32 °N	150.095 °W
USW00026529	TANANA	65.1744 °N	152.1069 °W
USW00026533	BETTLES	66.9161 °N	151.5089 °W
USW00026536	TATALINA	62.9 °N	155.9667 °W

APPENDIX A. Continued.

USW00026562	PORT	60.195 °N	154.3197 °W
USW00026563	CRN	60.724 °N	150.448 °W
USW00026615	BETHEL	60.785 °N	161.8292 °W
USW00026616	KOTZEBUE	66.8667 °N	162.6333 °W
USW00026617	NOME	64.5111 °N	165.44 °W
USW00026618	WALES	65.6239 °N	168.0992 °W
USW00026627	UNALAKLEET	63.8833 °N	160.8 °W
USW00026634	TIN	65.5667 °N	167.9167 °W
USW00026642	KIVALINA	67.7317 °N	164.5483 °W
USW00026643	DEERING	66.0689 °N	162.7639 °W
USW00026655	CRN	68.028 °N	162.921 °W
USW00026703	GAMBELL	63.7833 °N	171.75 °W
USW00027401	BARTER	70.1333 °N	143.6333 °W
USW00027406	DEADHORSE	70.1917 °N	148.4772 °W
USW00027502	BARROW	71.2833 °N	156.7814 °W
USW00027503	WAINWRIGHT	70.6378 °N	160.0145 °W
USW00027515	NUIQSUT	70.2117 °N	151.0017 °W
USW00027516	BARROW	71.3214 °N	156.6111 °W